ABSTRACT

Title of Dissertation:	INVESTIGATION OF THERMO-OPTIC EFFECTS IN SILICON MICRORING RESONATORS FOR SENSING AND INTERROGATION
	Hyun-Tae Kim, Doctor of Philosophy, 2017
Dissertation directed by:	Professor Miao Yu Department of Mechanical Engineering

Integrated photonics technology has great potential for enhancing the performance and reducing the volume and cost of optical sensing systems. Among many integrated photonic structures, silicon microring resonators have received much attention for both sensing and interrogation. Particularly, the high quality-factor of the microring resonators and the large thermo-optic coefficient and high thermal conductivity of silicon make them attractive for temperature sensing and thermally-tunable-filter-based interrogation. In this dissertation work, the thermo-optic effects in silicon microring resonators is studied and used in the silicon-ring-resonator-based temperature sensing and interrogation.

The first objective of this dissertation work is to develop a highly sensitive photonic temperature sensor, which can be potentially used for achieving portable, compact temperature sensing systems employing a low-resolution on-chip

spectrometer. However, the sensitivity of conventional silicon-ring-resonator-based temperature sensors is relatively low (less than ~80 pm/°C). These sensors often require the use of a bulky and expensive fine-resolution interrogator for high resolution temperature monitoring, since the sensor resolution is determined by the sensitivity. In this work, a novel photonic temperature sensor based on cascaded-ring-resonators with the Vernier effect is developed to simultaneously enhance the sensitivity and sensing range. With a proof-of-concept device, sensitivity enhancement of 6.3 times and sensing range enhancement of 5.3 times are demonstrated.

On-chip optical interrogators employing a silicon-ring-resonator-based thermally tunable filter (SRRTF) offer a promising solution for realizing portable, compact optical sensing systems. However, the slow interrogation speed of conventional SRRTF-based interrogators (less than a few Hz) has hindered their application for dynamic sensing. The second objective of this dissertation work is to develop a high-speed SRRTF-based interrogator, which can be used to interrogate optical sensors monitoring dynamic parameters. In this work, an SRRTF-based system utilizing the nonlinear transient thermal response of the SRRTF is developed for the speed enhancement. High speed interrogation (100 kHz of interrogation speed) of a fiber Bragg grating (FBG) sensor is successfully demonstrated with this system.

The third objective of the dissertation work is to further enhance the tuning speed and range of the previously developed SRRTF and to use it for simultaneous interrogation of multiplexed FBG sensors. Performance of SRRTF-based interrogators is primarily determined by thermal and optical characteristics of the SRRTF. However,

conventional SRRTF structures with a metallic heater on the top oxide cladding have limitations on interrogation speed and range. In this dissertation work, a novel SRRTF employing an interior-ridge-ring resonator and thermal through-cladding-vias is developed, which can realize enhanced tuning speed and range. With this SRRTF, interrogation of multiplexed FBG sensors at 125 kHz speed is demonstrated.

INVESTIGATION OF THERMO-OPTIC EFFECTS IN SILICON MICRORING RESONATORS FOR SENSING AND INTERROGATION

by

Hyun-Tae Kim

Dissertation submitted to the Faculty of the Graduate School of the
University of Maryland, College Park, in partial fulfillment
of the requirements for the degree of
Doctor of Philosophy
2017

Advisory Committee:
Professor Miao Yu, Chair
Professor Abhijit Dasgupta
Professor Bao Yang
Professor Bongtae Han
Professor Mario Dagenais, Dean's Representative

Dedication

To Yuan Yi

Acknowledgements

This dissertation could not have been written without the immense support and mentorship of my advisor, Professor Miao Yu. I am sincerely grateful to her for giving me the opportunity to research nanophotonic sensing systems and for the constant intellectual stimulation and encouragement she provided throughout my PhD study.

Besides my advisor, I would like to thank the rest of my dissertation committee: Prof. Abhijit Dasgupta, Prof. Bao Yang, Prof. Bongtae Han, and Prof. Mario Dagenais, for their time and invaluable advice.

I am also grateful to my fellow labmates in the Sensors and Actuators Laboratory: Hyungdae Bae, Haijun Liu, Yongyao Chen, Zhijian Zhang, Ying Chen, Randy Ganye, and Tim Wen, for the stimulating discussions and collaboration. It was a pleasure to work with them.

I would like to thank the Maryland Nanocenter staffs: Tom Loughran, Jonathan Hummel, Mark Lecates, and John Abrahams, for sharing their fabrication experiences.

Finally, the biggest thanks go to my family. My parents and parents-in-law always supported my decision and encouraged me. Most important of all, my wife, Yuan Yi, was there from the beginning of my PhD study and encouraged me when things got difficult. She was always confident that someday my work would come to fruition. To her I dedicate this dissertation.

Table of Contents

List of Figures

Chapter 1: Introduction and background

1.1 Problem of interest

Integrated photonics technology has great potential for enhancing the performance and reducing the volume and cost of optical sensing systems, including sensors and interrogators. For example, integrated photonic structures utilizing nanowire waveguides or photonic crystals have rendered ultracompact sensors with high sensitivity [1-4]. Furthermore, the integration of multiple photonic sensors into a micro-scale platform has enabled multi-parameter sensing with a compact device footprint [5, 6]. On the other hands, interrogators, which occupy most of the sensing system volume, can be integrated into a miniaturized photonic integrated circuit (PIC) chip. In particular, silicon PICs can be monolithically integrated with complementary metal-oxide-semiconductor (CMOS) circuitry [7], which helps reduce the volume and cost of optical sensing systems significantly. Among many integrated photonic structures, silicon microring resonators have received much attention for both sensors and interrogators. Particularly, the high quality-factor of the microring resonator and the large thermo-optic coefficient and high thermal conductivity of silicon make them attractive for temperature sensors and thermally-tunable-filter-based interrogators. This dissertation work focuses on the silicon-ring-resonator-based temperature sensors and interrogators.

1.1.1 Silicon photonic temperature sensors

Optical temperature sensors have received much attention as attractive alternatives to standard electrical resistance thermometers. Although the resistance thermometers have been widely used with advantages of easy implementation and fine resolution (i.e., ~0.01 °C), the susceptibility to environmental disturbance such as electromagnetic interference, mechanical shock, and humidity causes the resistance to drift over time [8-10]. Hence, they require periodic, time consuming calibration, which potentially increases the sensor ownership cost. Meanwhile, optical temperature sensors are robust to such environmental disturbances. Further, they have advantages of having better performance in harsh environments (i.e., high temperature and corrosive medium) and multiplexing capability [11-13].

For optical temperature sensing, fiber Bragg grating (FBG) sensors and extrinsic Fabry-Perot (FP) cavity sensors have been widely used. However, temperature sensitivity of the FBG sensors is low (e.g., ~10 pm/°C [14, 15]) due to the low thermo-optic coefficient of silica glass (i.e., 1.0×10^{-5} /°C [16]). Therefore, bulky and expensive fine-resolution sensor interrogators are required for precise temperature monitoring. Note that the sensing resolution is determined by the sensor sensitivity and the resolution of the sensor interrogator. For example, a 10 pm/°C sensitivity of FBG sensor with a 1 pm resolution of sensor interrogator provides only 0.1 °C sensing resolution. Compared to the FBG sensors, the extrinsic FP cavity sensors have demonstrated much higher temperature sensitivity [17]. However, as shown in Figure 1.1, fabrication of the extrinsic FP cavity sensor is complex and is not compatible with batch processing, which are obstacles to low-cost and high-yield fabrication.

Furthermore, these fiber optic sensors are not suitable for on-chip temperature monitoring, which is often required for biological and chemical analyses in lab-on-a-chip microsystems [18].

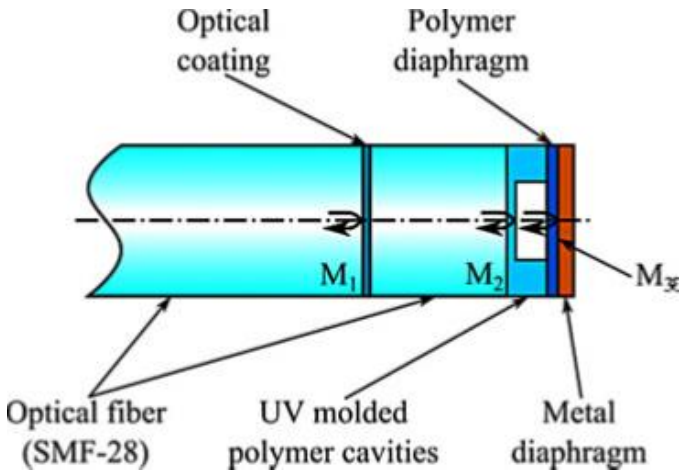

Figure 1.1 Schematic of the fiber optic temperature sensor based on an extrinsic FP cavity [17].

Silicon photonic temperature sensors can be an attractive solution to address these drawbacks of the optical temperature sensors. In other words, the large thermo-optic coefficient of silicon (i.e., 1.86×10^{-4} /°C [16, 19]) and the CMOS compatible fabrication of silicon photonic structures help build a compact, on-chip temperature sensor with enhanced temperature sensitivity.

1.1.2 Silicon photonic interrogators

Low coherence interferometry (LCI) and FBG have been widely used in a variety of sensing applications for monitoring of mechanical [17, 20], chemical [21, 22], and biomedical parameters [23, 24]. Compared to coherent interferometry, they have advantages of absolute and unambiguous measurement over a wide sensing range and robustness to the intensity fluctuation and wavelength instability [25]. Despite

these advantages they have not been used in some applications that require a compact, real-time sensing system such as wireless sensor networks for environmental/structural health monitoring [26, 27], micro air/underwater vehicles [28, 29], and implantable/portable medical devices [30, 31]. For these applications, both the sensor and interrogator should be compact and respond fast enough for real-time sensing. Various interferometric sensors and FBGs are readily available with a compact footprint, fast response speed, and low cost. However, conventional interrogators (i.e., spectrometers) are not only expensive but also slow and/or bulky.

For high-speed interrogation of the LCI and FBG sensors, time-wavelength spectroscopy was developed [32]. It converts spectral response of the sensor into a time-domain waveform through dispersive elements or tunable wavelength filters. Although the dispersive-Fourier-transformation-based approach demonstrated ultrafast sensor interrogation in the megahertz regime [33-37], miniaturization of the entire interrogation system remains challenging. From the aspect of the system miniaturization, the tunable-wavelength-filter-based approach is promising. For example, a miniaturized sensor interrogator with a 1 cm × 2 cm footprint was demonstrated by using a micro-electro-mechanical systems (MEMS) FP tunable wavelength filter, as shown in Figures 1.2 (a) and 1.2 (b) [38]. However, interrogators using a MEMS FP filter have the following drawbacks. First, mechanical moving parts of the MEMS FP filter such as a movable mirror or reflection membrane have limited spectral scan speed in the range of ~10s kHz [39, 40]. Further, these moving parts make the filter fabrication process complicated and are a potential cause of the interrogator failure. Finally, the optical interconnection between the MEMS FP filter and other

photonic components such as a superluminescent diode (SLED) and photodetector relies on conventional optical fibers, which requires a precise optical fiber alignment and assembly process.

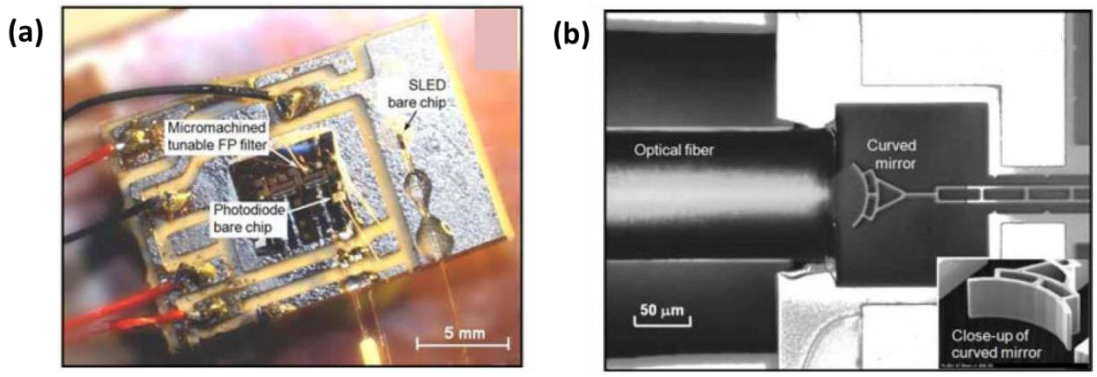

Figure 1.2 (a) A miniaturized sensor interrogator employing a tunable MEMS FP filter, SLED, and photodiode. (b) SEM image of the movable, reflection mirror in the tunable MEMS FP filter [38].

Recent progress in integrated photonics technology has shed light on realizing a compact, robust, high-speed interrogator. For example, integrated photonic filters capable of wavelength tuning with no moving parts have been demonstrated [41, 42], which can be attractive alternatives to the tunable MEMS FP filters. On the other hands, integrated planar diffraction gratings such as echelle gratings [43] and arrayed waveguide gratings [44] help miniaturize the spectrometers. Furthermore, these integrated photonic structures have an advantage of being optically interconnected with a SLED and photodetector through integrated waveguides [45-47].

1.2 Literature review

1.2.1 Silicon photonic temperature sensors

Silicon-on-insulator (SOI) microring resonators, waveguide Bragg gratings (WBGs), and Michelson interferometers (MIs) have been widely used for temperature

monitoring. An SOI-ring-resonator-based temperature sensor was first demonstrated by G. Kim et al [48]. A 4 μm-radius silicon ring resonator was used as a temperature sensor, as shown in Figure 1.3 (a). Temperature was measured by monitoring the resonance wavelength shift of the ring resonator [Figure 1.3 (b)]. The temperature-dependent resonance wavelength shift resulted from the thermo-optic effect in the ring resonator. In other words, the effective refractive-index of the ring waveguide increased with temperature, which redshifted the resonance wavelength. 83 pm/°C of temperature sensitivity was demonstrated with transverse-electric (TE) polarized light, which was the maximum achievable sensitivity under the single mode operation of the ring waveguide. The sensing range was 280 °C with a 23.4 nm of free spectral range [Figure 1.3 (c)]. The sensing resolution was determined by the sensitivity and the resolution of the optical interrogation system. With a 1 pm resolution tunable laser source, 0.01 °C of sensing resolution was achieved.

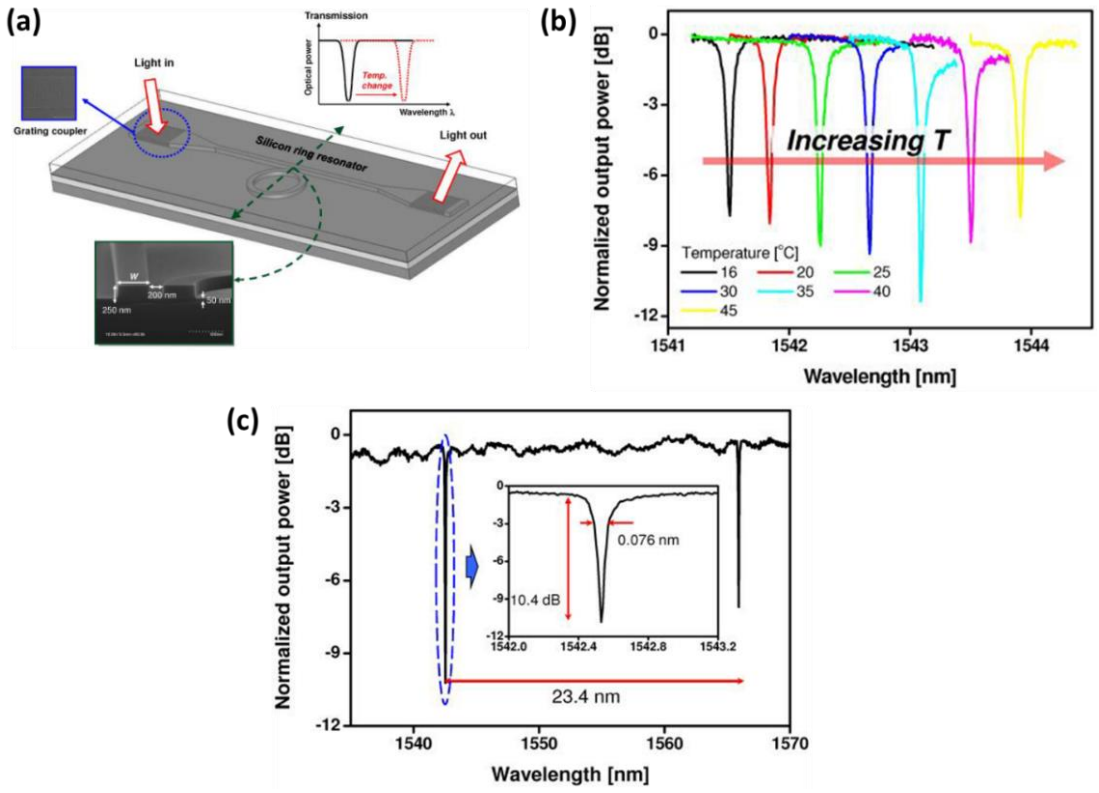

Figure 1.3 (a) 3D illustration and SEM images of the SOI ring resonator temperature sensor, (b) transmission spectra showing the temperature-dependent resonance wavelength shift, and (c) spectral response of the fabricated SOI ring resonator [48].

Using a similar SOI ring resonator structure, H. Xu et al demonstrated temperature sensing with much improved resolution [9]. To identify the resonance wavelength shift, they monitored the transmission intensity change. The input laser wavelength was selected to be centered at the side of the resonance (i.e., at the ~3 dB point), so that a small temperature change resulted in a large change in the transmission intensity. The intensity change was then used to estimate the resonance wavelength shift from the known resonance line shape. The sensing resolution was determined by the system noise including both the laser wavelength and the laser power noises. At 296.15 K, an 80 μK of the minimum resolution (i.e., noise floor) was achieved at 1 Hz sampling rate, where Allan variation was minimized [Figures 1.4 (a) and 1.4 (b)]. The

measured sensing resolution showed 13 times improvement compared to the wavelength scanning scheme by G. Kim et al. However, the noise floor rose to ±5 K at long time scale (i.e., >1 min). Therefore, the proposed scheme was not suitable for the temperature measurement requiring long observation times. Further, since the resonance wavelength shift should remain within the resonance linewidth, the sensing range was much narrower than that with the wavelength scanning scheme.

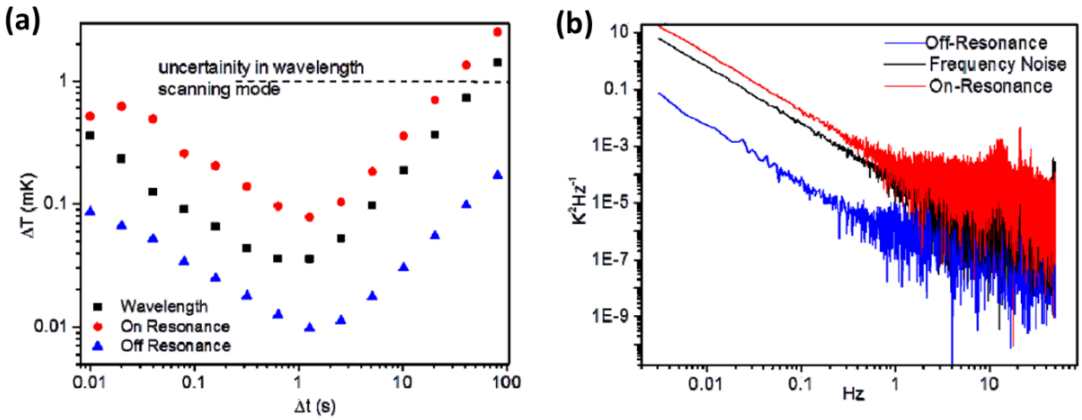

Figure 1.4 (a) Noise power spectral density as a function of sampling time scale and (b) the corresponding Allan variance plot [9].

While the free-spectral-range of the SOI ring resonator temperature sensors imposes a limitation on the maximum achievable sensing range, WBG-based temperature sensors have a sole resonance mode (i.e., Bragg resonance) and thus render a much wider sensing range. N. Klimov et al reported an SOI WBG temperature sensor [10], where the Bragg gratings were formed in a rectangular waveguide by modulating the waveguide width to a square-wave form and thus modulating the effective refractive-index of the waveguide [Figure 1.5 (a)]. The temperature-dependent Bragg wavelength shift was demonstrated from 5 ˚C to 160 ˚C with 82 pm/˚C of sensitivity, as shown in Figure 1.5 (b). Although temperature was monitored over a 155 ˚C range,

it was claimed that the sole resonance mode of the WBG enables to continuously monitor temperature from cryogenic up to silicon melting temperature. The measured sensor resolution was 1.25 ˚C, which was much coarse than that of the SOI ring resonator temperature sensors (i.e., 0.01 ˚C). The coarse resolution mainly resulted from the error in estimating the center wavelength of the blunt and wide-linewidth Bragg resonance (i.e., the resonance linewidth was 5.1 nm).

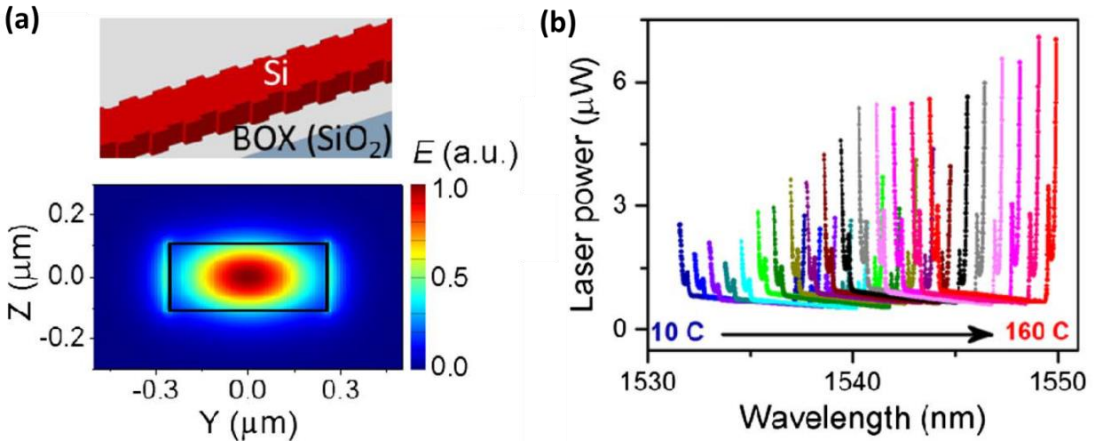

Figure 1.5 (a) Schematic of Bragg grating in the SOI waveguide and (b) transmission spectra of the WBG sensor measured at different temperatures [10].

C. Chang et al developed a silicon WBG temperature sensor that rendered sharp and narrow-linewidth Fano resonance [49]. The sensor consisted of a phase plate and Bragg gratings, as shown in Figure 1.6 (a). The effective refractive-index modulation for the Bragg gratings was achieved by a periodic air hole array aside the silicon waveguide. The interference of reflected beams from the phase plate and Bragg gratings rendered asymmetric resonance with ~1 nm resonance linewidth [Figures 1.6 (b) and 1.6 (c)]. The sensitivity was 77 pm/˚C at room temperature, but the sensor resolution was not reported.

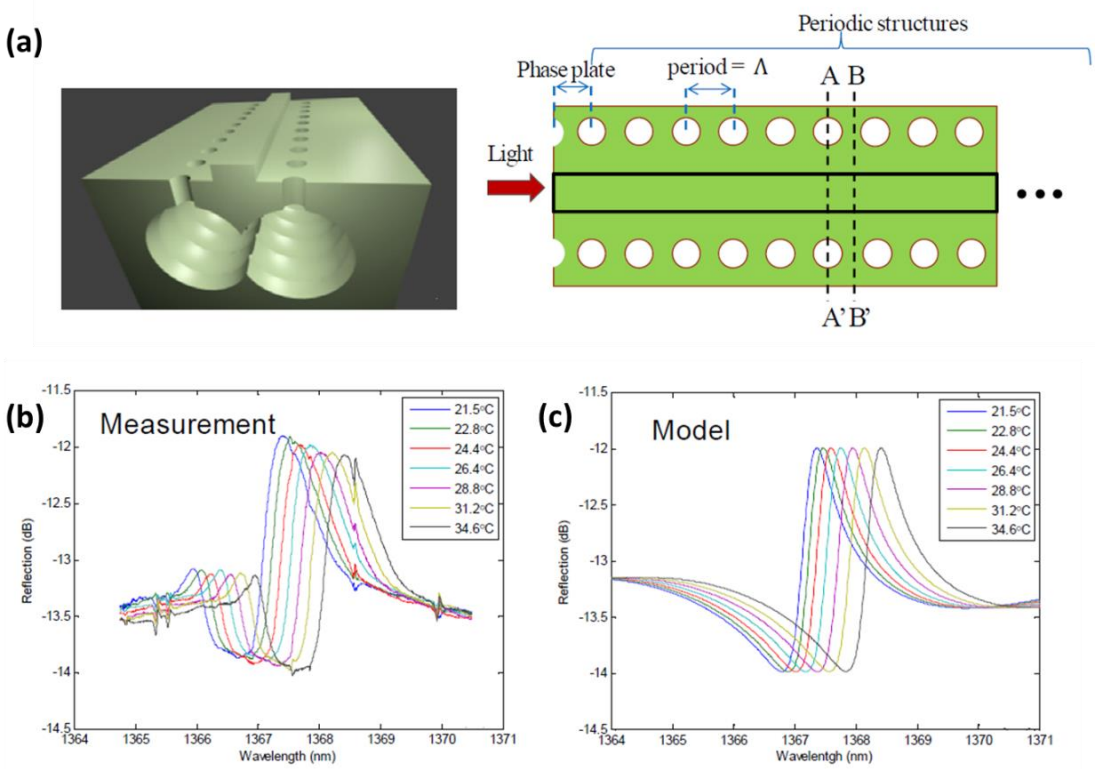

Figure 1.6 (a) Schematic of the silicon WBG reflector for rendering Fano resonance. Reflection spectra for temperature ranging from 21.5 °C to 34.6 °C obtained from (b) experiment and (c) calculation [49].

J. Tao et al demonstrated temperature monitoring with an SOI MI structure [50]. As shown in Figure 1.7 (a), the MI temperature sensor employed a directional coupler for a light splitter/combiner, two waveguides with different lengths for MI arms, and two loop-waveguides for reflection mirrors. The temperature-dependent phase difference between the two arms shifted the destructive interference wavelength with 113.7 pm/˚C sensitivity [Figure 1.7 (b)]. The free spectral range between the adjacent destructive interference wavelengths was 27.9 nm, which rendered a 246 ˚C of sensing range.

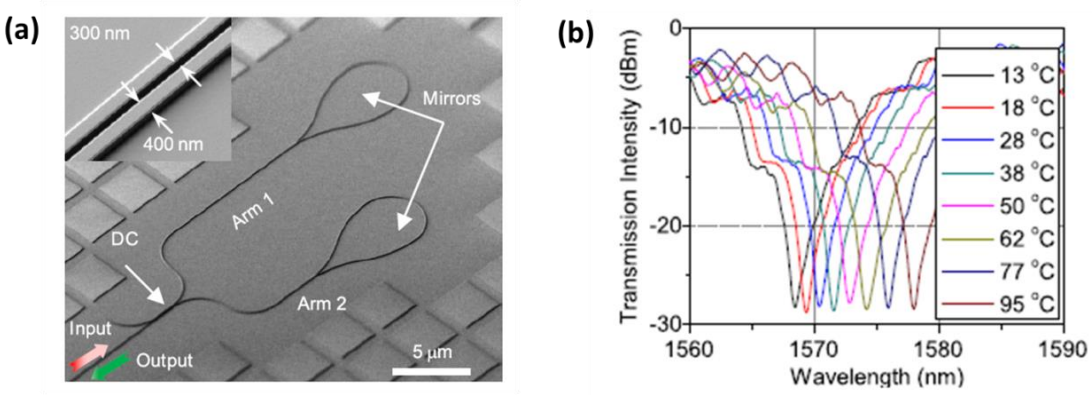

Figure 1.7 (a) SEM image of the fabricated SOI MI temperature sensor and (b) transmission spectra at different temperatures [50].

S. Tsao et al also reported an SOI MI temperature sensor [51], but it consisted of different photonic components from that by J. Tao et al. As shown in Figure 1.8, a 2 × 2 multimode interference coupler and waveguide Bragg reflective gratings were used for a beam splitter/combiner and reflection mirrors, respectively. 293 pm/˚C of sensitivity was obtained from analytical calculation, but experimental results were not provided. However, the calculated sensitivity is believed to be overestimated, since the thermo-optic coefficient of silicon which was used for the sensitivity calculation was ~4 times higher than typical values.

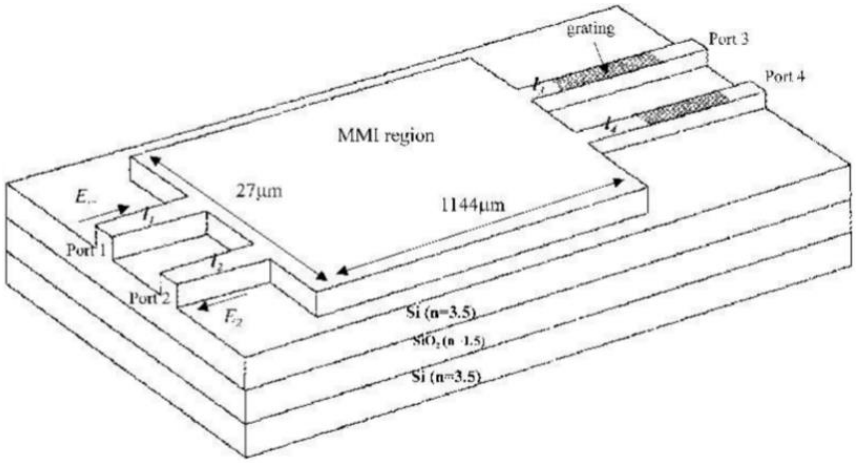

Figure 1.8 3D illustration of an SOI MI temperature sensor [51].

1.2.2 Silicon photonic interrogators

Silicon photonic interrogators can be categorized into two groups according to their spectrum sampling method: serial sampling and parallel sampling. Silicon photonic interrogators based on the serial sampling method consist of a broadband source, tunable wavelength filter, and photodetector. Figure 1.9 shows the interrogation principle. The broadband source (i.e., P_{source}) combined with the tunable wavelength filter (i.e., T_{filter}) produces a narrowband tunable optical source (i.e., $P_{filtered}$) for scanning across the spectral bandwidth of the optical sensor (i.e. T_{sensor}). The reflection (or transmission) power intensity from the optical sensor (i.e., P_{sensor}) is measured by the photodetector. The spectral response of the optical sensor is then reconstructed by calibrating the measured intensity waveform to a fixed wavelength reference.

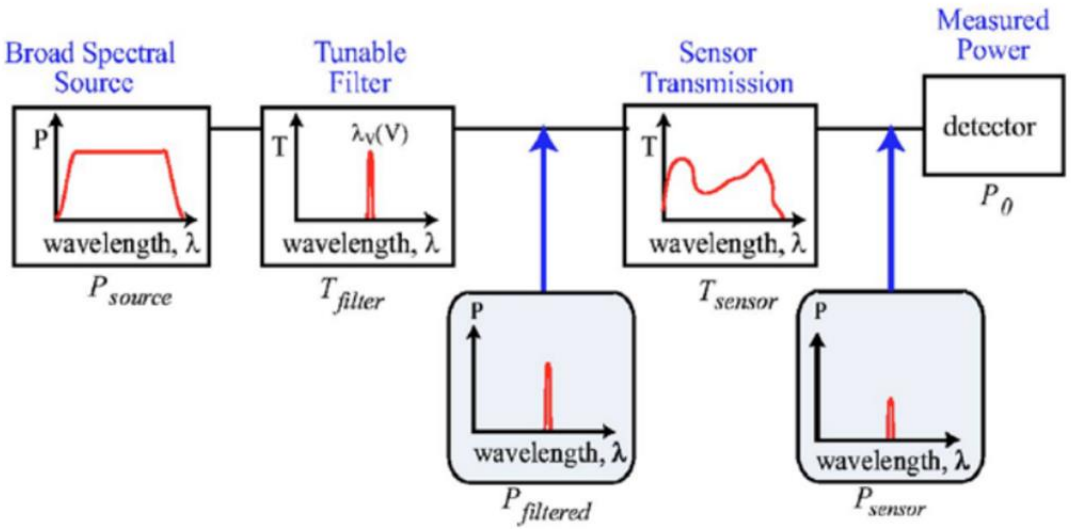

Figure 1.9 Schematic of sensor interrogation using a tunable wavelength filter [52].

For the tunable wavelength filter, silicon-ring-resonator-based thermally tunable filters (SRRTFs) have been widely used due to the following advantages. First, ring resonators provide excellent wavelength selectivity due to their high quality-factor

[53]. Second, the free spectral range and finesse of ring resonators can be easily tailored by changing the in-plane geometric parameters such as a ring radius and ring-to-bus waveguide coupling gap [54]. Third, the high refractive-index contrast of the SOI structure enhances the waveguide mode confinement and reduces the waveguide bending loss. Therefore, it helps build an ultracompact tunable filter [55, 56]. Finally, the large thermo-optic coefficient and high thermal conductivity of silicon helps enable high-speed (~1 MHz) and wide-range wavelength tuning [41, 42, 57]. Note that although electro-optic tuning with the free-carrier effect has been widely used for high-speed silicon ring modulators in the GHz regime, the large free-carrier absorption loss has limited the wavelength tuning range to less than 0.2 nm [58]. Other electro-optic tuning schemes such as the Franz-Keldysh effect, the Kerr effect, and the Pockels effects are very weak in silicon at 1550 nm wavelength [59]. Recently, silicon-organic-hybrid platforms, which consist of silicon slot waveguides and electro-optic polymer cladding with high Pockels coefficient, have demonstrated the high-speed optical modulation in the GHz regime and the capability of wide-range wavelength tuning [60]. However, it has a drawback that the electro-optic polymer is not CMOS compatible.

A. Shen et al demonstrated the interrogation of an FBG sensor with an SRRTF [61]. The SRRTF consisted of a silicon ring resonator and a metallic micro-heater on the top oxide cladding layer, as shown in Figure 1.10 (a). For the sensor interrogation the resonance wavelength of the ring resonator was thermally tuned over the spectral range including the Bragg wavelength of the FBG. The output intensity of the interrogator was maximized when the resonance wavelength coincided with the Bragg wavelength [Figure 1.10 (b)]. The spectral information of the FBG sensor was then

demodulated by mapping the heating power and the corresponding resonance wavelength.

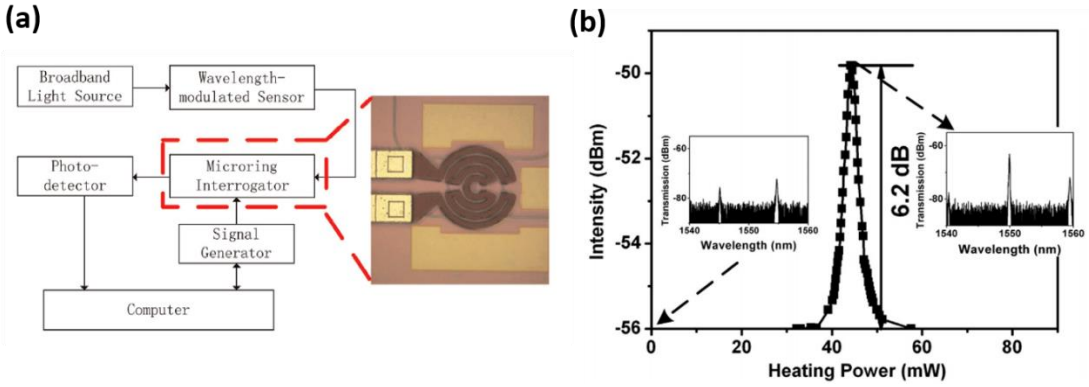

Figure 1.10 (a) Schematic of the sensor interrogation system using a SRRTF. (b) Measured output intensities as a function of heating power; the insets are transmission spectra of the ring resonator filter at given heating power [61].

X. Wang et al interrogated an FBG sensor under strain change using an SRRTF with a feedback control system [62]. The SRRTF was tuned so that the resonance wavelength tracked the Bragg wavelength, and the output intensity of the interrogator was used for the error signal of the feedback control system, as shown in Figure 1.11 (a). By monitoring the input voltage waveform for the micro-heater of the SRRTF, they measured a 1 Hz strain change applied to the FBG sensor [Figure 1.11 (b)].

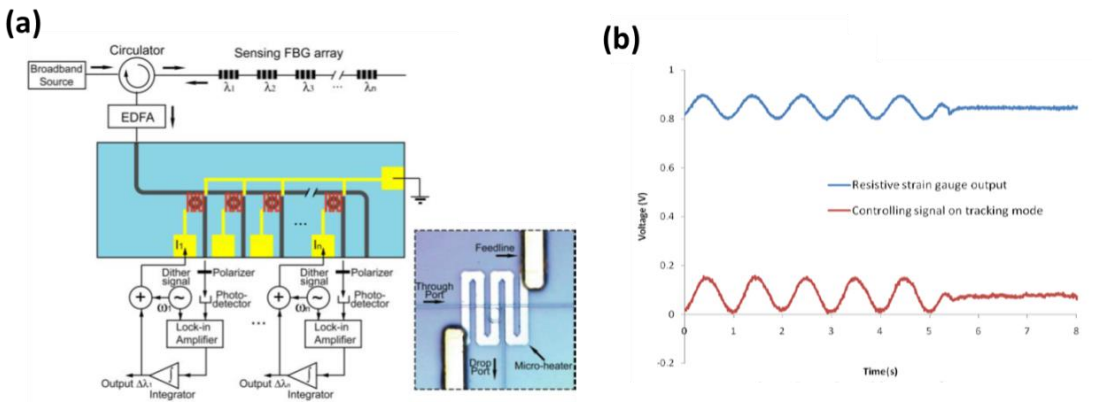

Figure 1.11 (a) Schematic of the tracking mode FBG sensor interrogation system and the microscope image of the fabricated SRRTF. (b) Dynamic tracking waveform for 1 Hz strain perturbation on the FBG sensor [62].

G. Vargas et al reported a time-to-wavelength mapping scheme for an SRRTF-based interrogator, which is capable of interrogating an FBG sensor under strain change [63, 64]. They utilized a periodic, triangular-wave input voltage to operate the SRRTF, as shown in Figure 1.12 (a). The output intensity of the interrogator was maximized when the resonance wavelength coincides with the Bragg wavelength. Therefore, the output intensity waveform rendered two peaks at each tuning cycle: one during the redshift and the other during the blueshift of the resonance wavelength. The time interval between the two peaks changed as the Bragg wavelength shifts, as shown in Figures 1.12 (b) and 1.12 (c). The Bragg wavelength information was then demodulated by monitoring the change of the time interval. With a 3 nm of wavelength tuning range and 0.5 Hz repetition rate, they demonstrated the measurement of static strain applied to the FBG sensor with a 50 pm accuracy.

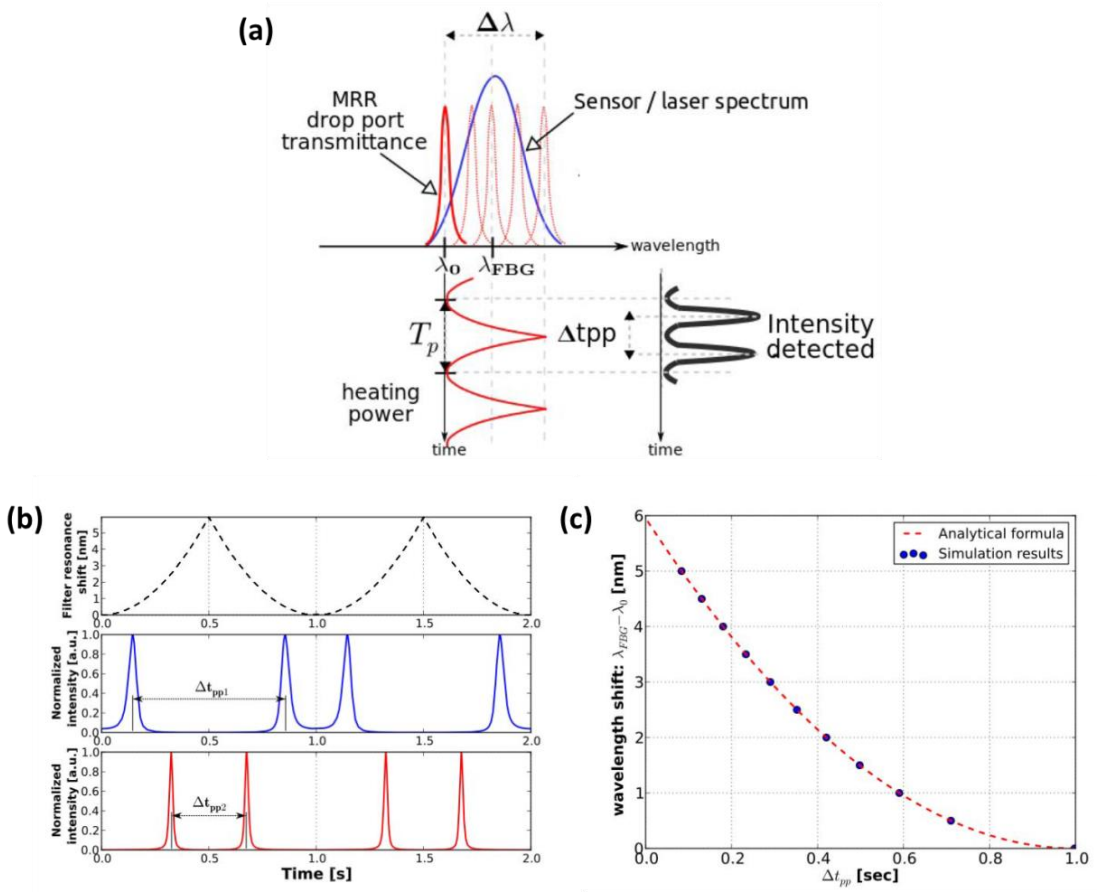

Figure 1.12 (a) Schematic of the time-to-wavelength demodulation using a SRRTF. (b) Simulation results of (top) the resonance wavelength tuning as a function of time and the corresponding output intensity at the FBG Bragg wavelength shift of (middle) 0.5 nm and (bottom) 2.5 nm. (c) Simulation results of FBG Bragg wavelength shift as a function of the time interval [64].

Silicon photonic sensor interrogators based on the parallel sampling method utilize an on-chip spectrometer. P. Cheben et al demonstrated a 50-channel, arrayed-waveguide-gratings spectrometer [44]. Light coming from an input waveguide channel was spatially distributed with different wavelengths by the arrayed waveguide grating, and the distributed light beams were coupled into multiple output waveguide channels. To achieve high channel density and thus fine spectral resolution, they used a narrow, high-aspect-ratio 0.6 μm × 1.5 μm waveguide aperture [Figure 1.13 (a)]. The

spectrometer provided 0.2 nm channel spacing with a 0.15 nm linewidth at 1550 nm wavelength, and the operating bandwidth was 10 nm [Figure 1.13 (b)].

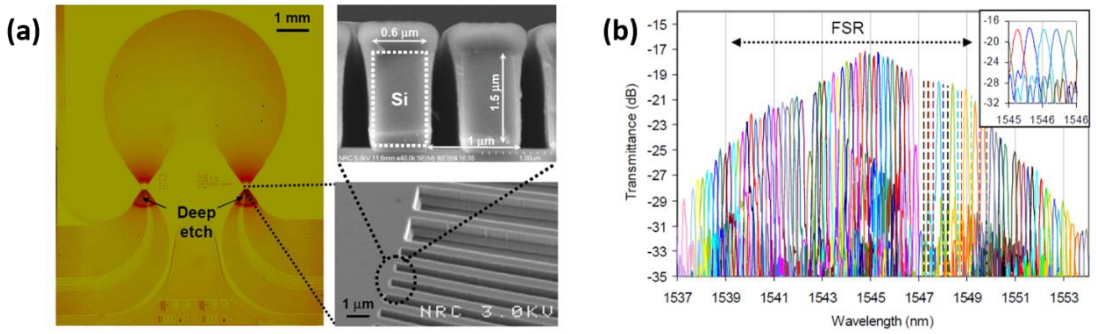

Figure 1.13 (a) A microscope image of the 50-channel, arrayed-waveguide-grating spectrometer and SEM images of narrow deep-etched rectangular waveguide apertures at the Rowland circle. (b)Measured spectra for the arrayed-waveguide-grating spectrometer [44].

B. Kyotoku et al demonstrated an echelle grating spectrometer combined with a ring resonator filter, as shown in Figure 1.14 (a) [65]. The echelle grating was used to spatially distribute incoming light with different wavelengths [66-68]. The ring resonator filter was employed to reduce the channel linewidth and thus enhance the resolution of the spectrometer. The incoming light filtered by the ring resonator was inserted into the spectrometer. Here, the free-spectral-range of the ring resonator was designed to match to the channel spacing of the spectrometer. Therefore, the channel linewidth was reduced to be the same as the resonance linewidth of the ring resonator. The spectrometer had 10 channels with a 10 nm operating bandwidth at 1490 nm wavelength, and the measured channel spacing and linewidth were 1 nm and 0.1 nm, respectively. To take full advantage of the reduced channel linewidth, the ring resonator was thermally tuned, so that the resonance wavelength shifted up to 1 nm and at every 0.1 nm resonance shift the spectrometer acquired the spectral information [Figure 1.14 (b)]. Therefore, the spectrometer rendered virtually100 channels with 0.1 nm channel

spacing [Figure 1.14 (c)]. Note that the spectral information was serially sampled during the thermal tuning.

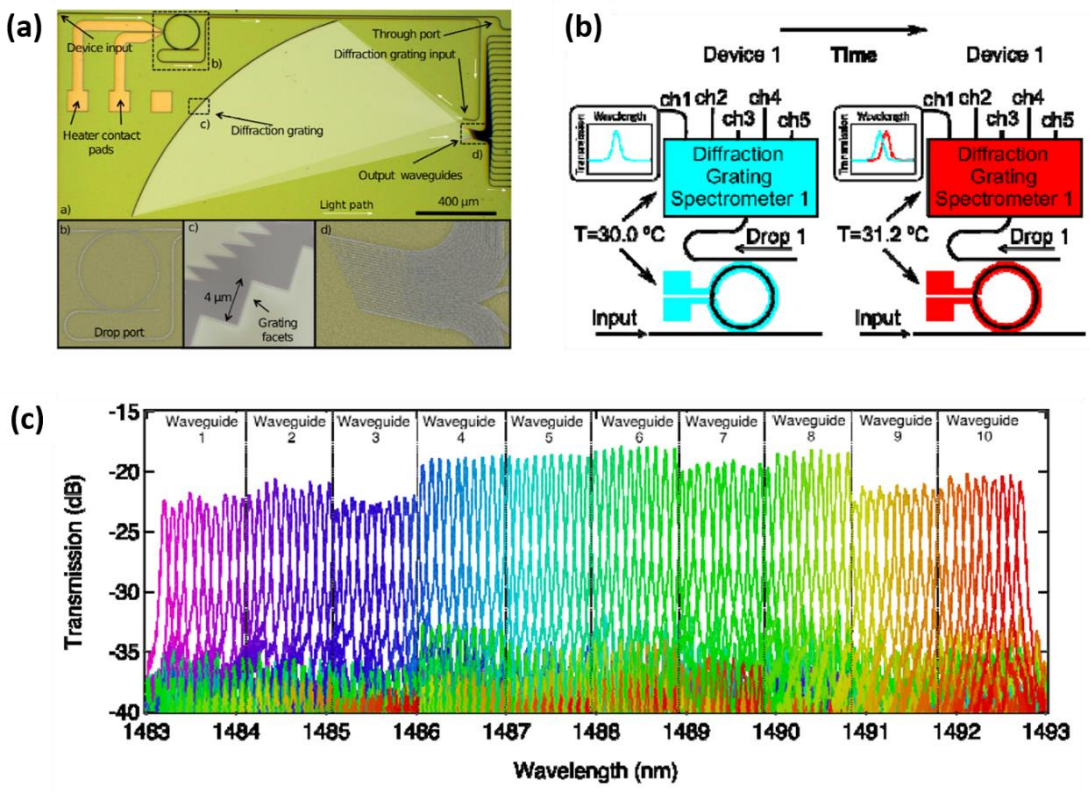

Figure 1.14 (a) Microscope images of the echelle grating spectrometer with a tunable ring resonator filter. (b)Schematic showing the time serialization based on the thermo-optic tuning of the ring resonator and (c) transmission spectra for the echelle grating spectrometer using the time serialization scheme [65].

Z. Xia et al reported an on-chip spectrometer using an array of microring resonators [69]. A large number of microring resonators were coupled into a bus waveguide and served as channel dropping filters, as shown in Figure 1.15 (a). The radius of the ring resonators was tailored so that each ring resonator rendered a unique spectral channel. Therefore, the array of ring resonators spatially separated incoming light from the bus waveguide with different wavelengths [Figure 1.15 (b)]. The spectrometer employed 81 microring resonators and rendered 0.6 nm channel spacing

and 0.05 nm channel linewidth [Figures 1.15(c) and 1.15(d)]. The operating bandwidth was 50 nm at 1550 nm wavelength.

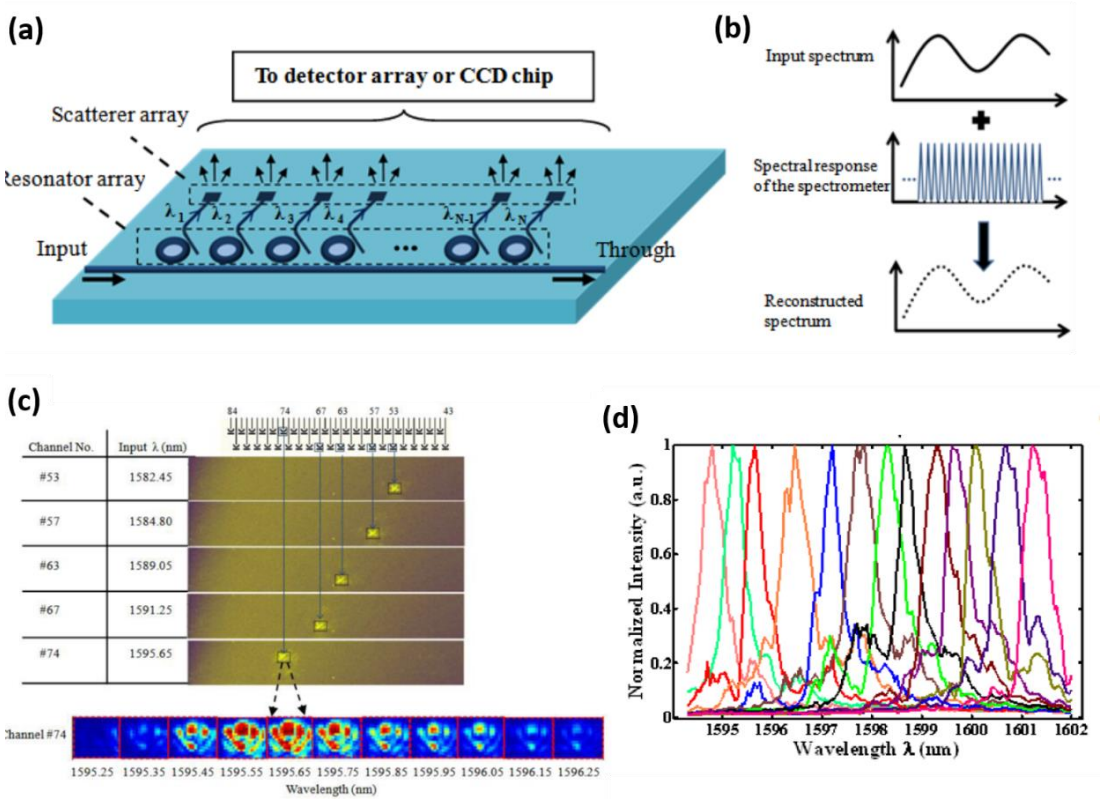

Figure 1.15 (a) Configuration and (b) working principle of the ring-resonator-based spectrometer. (c) Infrared camera images of the channel responses at different input wavelength and post-processed light pattern scattered by channel #74 at different input wavelengths around its resonance. (d) Calibration spectra of the 13 channels covering the wavelength range from 1594.30 nm to 1602.00 nm [69].

1.3 Motivation for the dissertation

1.3.1 Silicon photonic temperature sensors

While silicon photonic temperature sensors using an SOI ring resonator, WBG, and MI have rendered enhanced temperature sensitivities compared with the glass-optical-fiber-based sensors, there exists the fundamental limit in the maximum achievable sensitivity. The sensitivity of these silicon photonic temperature sensors is

primarily determined by the thermo-optic effect in the SOI waveguide (i.e., dn_{eff}/dT) as follows [13, 48, 50]:

$$\frac{d\lambda}{dT} = \frac{\lambda}{n_g}\left(\frac{\partial n_{eff}}{\partial T} + n_{eff}\alpha_{Si}\right), \tag{1.1}$$

where the λ is the resonance wavelength for ring resonators, the Bragg wavelength for WBGs, or the destructive interference wavelength for MIs. The n_{eff} and n_g are the effective refractive-index and group index of the waveguide, respectively, and the α_{Si} is the thermal expansion coefficient of silicon. For the SOI structure, the dn_{eff}/dT increases with the waveguide mode confinement and thus increases with the waveguide core size [70, 71]. In general, the maximum core size is determined by the single mode condition of the waveguide. For a 220 nm-thick SOI structure, the maximum waveguide width for the single mode condition is ~450 nm and the corresponding temperature sensitivity is ~85 pm/˚C [48]. If these silicon photonic temperature sensors are interrogated by using low-resolution portable spectrometers (e.g., 0.1 nm resolution), the sensing resolution is only ~1.2 ˚C. Therefore, they still require bulky and expensive high-resolution sensor interrogators for precise temperature monitoring. To overcome this limitation the temperature sensitivity needs to be further enhanced.

The cascaded-ring-resonator (CRR)-based Vernier effect has been an attractive solution for enhancing the sensitivity of silicon-ring-resonator-based sensors, as shown in Figure 1.16 [72-74]. Although some efforts have been made for CRR-based bio/chemical sensors [75, 76], the conventional CRR-based approach has two main limitations. First, applying the conventional CRR-based sensing approach (i.e., isolating the reference ring from the sensory input) to temperature sensing requires a

more complicated multi-mask fabrication process, which is believed to be the main reason why the CRR-based temperature sensing has not yet been demonstrated. Second, it cannot enhance both the sensitivity and sensing range. Only the enhancement of sensitivity has been demonstrated with previous CRR-based sensors.

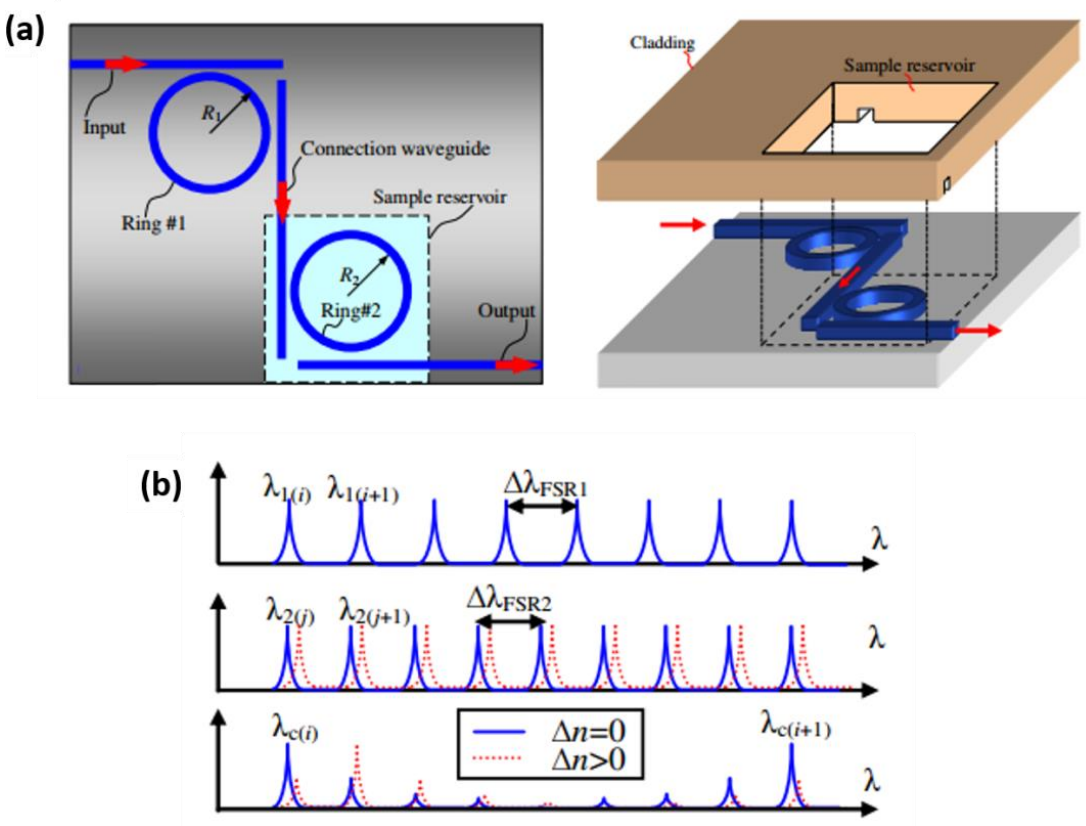

Figure 1.16 (a) The schematic configuration of the cascaded ring resonator-based optical sensor and (b) spectral responses for the cascaded ring resonators [72].

In this dissertation, a novel CRR-based sensing approach is proposed to overcome the limitations of the conventional CRR-based sensing approach. The proposed approach employs two ring resonators with different temperature sensitivities and different free-spectral-ranges, so that the CRR-based sensor can enhance both the temperature sensitivity and sensing range with a much simpler fabrication process. Therefore, it will enables silicon photonic sensors to precisely monitor temperature

with a low-resolution portable spectrometer, which helps reduce the volume and cost of optical temperature monitoring system.

1.3.2 Silicon photonic interrogators

Although on-chip spectrometers enable high-speed interrogation of an optical sensor, there exists a tradeoff between the interrogation resolution and device footprint [44, 65]. To achieve fine-resolution interrogation with a wide interrogation range, on-chip spectrometers have to accommodate a large number of waveguides in the arrayed waveguide gratings (or grooves in the diffraction grating) with a corresponding large number of photodetectors, which will significantly increase the device footprint. Further, on-chip spectrometers cannot interrogate multiple heterogeneous LCI sensors simultaneously, which prevents their application to a multifunctional optical sensing system.

Meanwhile, SRRTF-based sensor interrogators have an advantage of achieving fine-resolution interrogation with an ultracompact device footprint since the resolution is determined by the resonance linewidth of the SRRTF. Further, such a serial sampling method is capable of interrogating multiple heterogeneous LCI sensors simultaneously by adding the same number of photodetectors with the LCI sensors, as shown in Figure 1.17 [26]. However, SRRTF-based sensor interrogators have not yet demonstrated high-speed and wide-spectral-range interrogation, which is required for real-time monitoring of multiple optical sensors. The speed and range of SRRTF-based interrogators have been less than ~1 Hz and ~10 nm, respectively.

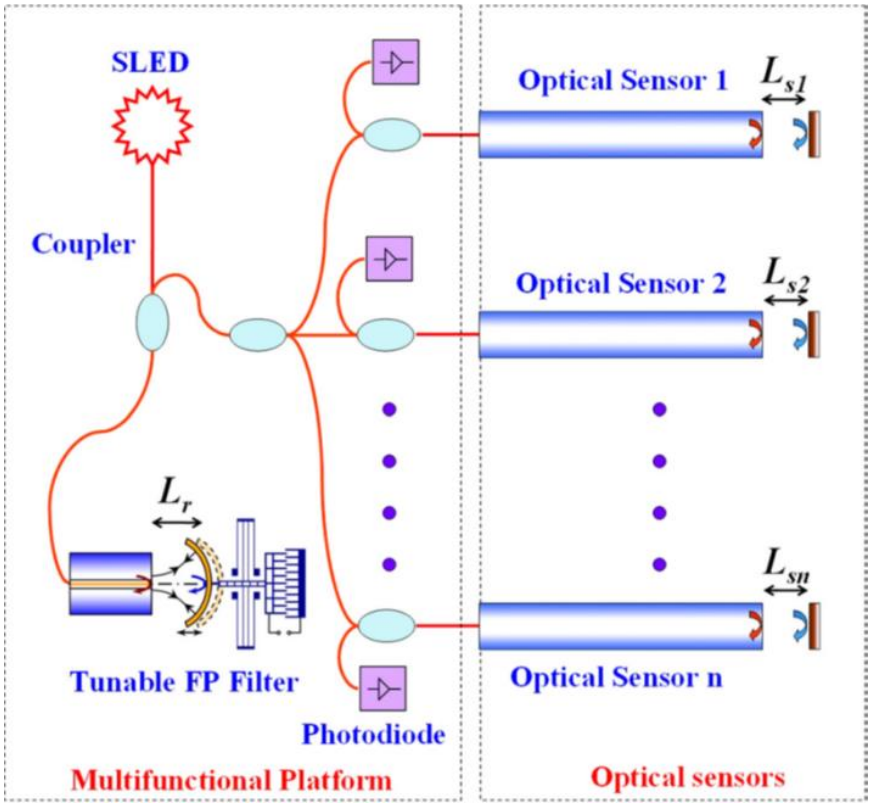

Figure 1.17 (a) Schematic of the multifunctional optical sensor platform employing a tunable wavelength filter [26].

The slow interrogation speed mainly resulted from the conventional interrogation scheme (i.e., time-to-wavelength mapping scheme). For the wavelength demodulation the SRRTF was driven by triangular-wave input voltage, and the time-domain output signal from the photodetector was mapped into wavelength domain, as shown in Figure 1.12. The time-to-wavelength transfer function for the mapping process was obtained from the time-dependent resonance wavelength shift of the SRRTF, where the resonance wavelength (λ_{res}) was calculated based on the steady-state temperature of the ring resonator at a given input voltage [64]:

$$\lambda_{res}(t)=\begin{cases}\lambda_0+\dfrac{\eta}{R}\left(\dfrac{2V_p}{T}\right)^2 t^2, & 0\le t<\dfrac{T}{2}\\ \lambda_0-\dfrac{\eta}{R}\left(\dfrac{2V_p}{T}\right)^2 (t-T)^2, & \dfrac{T}{2}\le t<T,\end{cases} \tag{1.2}$$

where the λ_0 is the initial resonance wavelength, the η is the tuning power efficiency, the R is the resistance of the micro-heater, the V_p is the peak amplitude of the triangular-wave input voltage, the T is the period of the triangular-wave input voltage, and the t is time. Such an interrogation scheme is valid only if the SRRTF operates at a low frequency (i.e., slow interrogation speed), so that the thermal response time of the SRRTF can be ignored compared with the T. If the operating frequency increases, the thermal response time becomes significant and cannot be ignored, which causes a wavelength demodulation error. On the other hands, the SRRTF was operated with a narrow tuning range to prevent a high-temperature failure of the metallic micro-heater. For conventional SRRTFs the micro-heater was located on the top oxide cladding layer of the silicon ring resonator. To avoid the absorption loss due to the lossy metal, the top oxide cladding layer was designed to be thicker than 1 μm. However, the thick oxide cladding layer and the low thermal conductivity of the oxide (1.38 W/mK) resulted in large thermal resistance between the micro-heater and the ring waveguide, which made the heater temperature much higher than the waveguide temperature.

In this dissertation, a high-speed interrogation scheme, which utilizes the nonlinear transient response of the SRRTF to square-wave input voltage, is investigated to enhance the speed of the SRRTF-based interrogators. Furthermore, an SRRTF employing an interior-ridge-ring resonator and a thermal through-cladding-vias (TCVs)

is proposed and developed for enhancing the tuning speed and range. The high-speed interrogation scheme with the proposed SRRTF will help develop a high-speed on-chip interrogator for simultaneous interrogation of multiple optical sensors (e.g., multiplexed FBG sensors).

1.4 Overview of the dissertation

This dissertation work is aimed at achieving enhanced understanding of thermo-optic effects in silicon microring resonators and applying such understanding to the development of (1) a cascaded-ring-resonator-based temperature sensor, (2) an SRRTF-based high-speed interrogator, and (3) a SRRTF with enhanced speed and range for simultaneous interrogation of multiplexed FBG sensors. To achieve these objectives, this dissertation work includes following three research thrusts.

Research thrust 1: Cascaded-ring-resonator-based photonic temperature sensor

A temperature sensing model with the cascaded-ring-resonator-based Vernier effect is established for enhancing the sensitivity as well as the sensing range. For a single ring resonator, simulation studies are conducted to examine the effects of the ring geometry on the temperature sensitivity and sensing range. With the established sensing model and the obtained understanding of the geometry effects a cascaded-ring-resonator-based temperature sensor is designed. Finally, the temperature sensor is fabricated and experimental studies are carried out to demonstrate the simultaneous enhancement of the sensitivity and sensing range.

Research thrust 2: High-speed optical interrogator with an SRRTF

The nonlinear transient response of the SRRTF to a square-wave input voltage is investigated using analytical and numerical methods. With the obtained understanding of the nonlinear transient response a high-speed interrogation scheme (i.e., scanning the entire spectral range during the thermal response time of the SRRTF) is established. For proof-of-concept, the SRRTF is fabricated and the SRRTF-based interrogator is developed. Experimental studies are carried out to characterize the nonlinear transient response of the fabricated SRRTF, and an FBG sensor under static and dynamic temperature changes is interrogated with the developed interrogator.

Research thrust 3: SRRTF with enhanced speed and range for simultaneous interrogation of multiplexed FBG sensors

A SRRTF with an interior-ridge-ring resonator and a thermal TCV is investigated to enhance the optical and thermal characteristics, including the quality factor (Q-factor), full spectral range (FSR), thermal response time, and ratio of the waveguide temperature change to the heater temperature change. Parametric studies are performed to examine the effect of the interior-ridge ring and thermal TCVs on the optical and thermal characteristics of the SRRTF. Based on the obtained understanding an SRRTF employing the interior-ridge ring and thermal TCVs is designed and fabricated. Experimental studies are carried out to characterize the fabricated SRRTF. Finally, a high-speed interrogator is developed with the fabricated SRRTF, and multiplexed FBG sensors are interrogated simultaneously with the developed interrogator.

Chapter 2: Cascaded-ring-resonator-based temperature sensor with simultaneously enhanced sensitivity and sensing range

2.1 Introduction

Recently, silicon photonics based temperature sensors have received much attention. These sensors are robust against electromagnetic interference and drift due to environmental disturbances such as mechanical shock and humidity [8-10], which make them superior to conventional electrical temperature sensors in many applications. Silicon-on-insulator (SOI) based micro ring resonators [9, 48], waveguide Bragg gratings [10], and Michelson interferometers [50, 51] have been demonstrated for temperature sensing. Compared with optical fiber based temperature sensors, these sensors can achieve much higher sensitivity due to the high thermo-optic coefficient of silicon [16, 19, 77]. Furthermore, the integration of silicon photonic sensors with the complementary metal-oxide-semiconductor (CMOS) process enables cost-effective on-chip temperature sensing [78], which is not readily achievable with optical fiber Bragg gratings [79, 80] or fiber tip based temperature sensors [17, 81].

Among many silicon photonics based structures, SOI micro ring resonators offer some unique features that render them an attractive choice for high performance temperature sensing. The high quality (Q) factor spectral response of silicon ring resonators manifests a strong temperature-dependence [56], which enables high resolution temperature sensing. Furthermore, the high refractive-index contrast of the

SOI waveguide provides excellent optical confinement and reduces the waveguide bending loss [82], thus facilitates the development of ultra-compact photonic sensors [55, 83, 84].

Most ring resonator based temperature sensors operate by monitoring the resonance wavelength shift with a tunable laser or spectrometer [9, 48, 85]. This shift results from the optical path length change of the ring waveguide, which is primarily due to the thermally-induced effective refractive index change. The temperature sensitivity of SOI ring resonators is typically limited to be ~80 pm/˚C [9, 48]. Note that the temperature detection limit (i.e., resolution) is determined by the sensitivity of the sensor and the resolution of the spectral measurement system. Due to the limited sensitivity of a single ring resonator, in order to achieve high resolution temperature detection, an expensive, narrow linewidth tunable laser or fine resolution optical spectrum analyzer (OSA) is often required. On the other hand, the sensing range is determined by the free spectral range (FSR) of the ring resonator, which corresponds to the temperature change that can induce the resonance wavelength shift to a full FSR. The sensing range can be increased by increasing the FSR, which is usually achieved by reducing the ring size. For example, a 120 ˚C of sensing range was obtained by a 9.2 μm-radius ring resonator [9], and a 280 ˚C of sensing range by a 4 μm-radius ring resonator [48].

There have been many efforts devoted towards enhancing the performance of ring resonator based sensors by employing various ring resonator architectures. These include cascaded ring resonators (CRR) [72, 86] for realizing the Vernier effect [87], vertically stacked ring resonators for obtaining resonance splitting [88], and Bragg

grating ring resonators for achieving resonance splitting and Fano resonance [89]. While the resonance splitting and Fano resonance have been used to improve the sensor resolution, the CRR-based Vernier effect has been widely used to enhance the sensitivity of the ring resonator based sensors. It has also been used to tailor the spectral characteristics of ring resonators such as suppressing undesired resonance modes and increasing finesse and FSR [90-92]. In a conventional CRR sensor configuration, two ring resonators (a reference resonator and a sensor resonator) are designed to have slightly different FSRs (FSR_1 and FSR_2, respectively). The resonance wavelength of the sensor resonator shifts with respect to a sensory input, while the reference resonator is designed to be isolated from the sensory input, and thus its resonance wavelength remains unchanged. The major resonance wavelength of the CRR is located at the common resonance wavelength of the two ring resonators. Neglecting the dispersion, the FSR of the CRR is [73]

$$FSR_{CRR} = \frac{FSR_1 FSR_2}{FSR_1 - FSR_2}. \tag{2.1}$$

Note that when the resonance wavelength of the sensor resonator shifts one FSR, the resonance wavelength shift of CRR is amplified to one FSR_{CRR}. Therefore, the sensitivity of the CRR is amplified by a factor of FSR_{CRR}/FSR_2. It should be noted that although the conventional CRR based sensors can help enhance the sensitivity by increasing the overall FSR_{CRR}, the sensing range will not be enhanced as it is determined by the FSR of the sensor resonator. On the other hand, to isolate the reference resonator from the sensory input, a multi-mask fabrication process is required: one mask for patterning the waveguides of the CRR and another mask for selectively removing the top cladding of the sensor resonator [73, 74, 76, 93].

The conventional CRR based sensors have been demonstrated for biological or chemical sensing [73, 74, 76, 93]. However, enhancing temperature sensitivity with CRRs has not yet been demonstrated. The main challenge is the isolation of the reference resonator from a temperature change. Alternatively, the temperature sensitivity of the reference ring resonator can be suppressed by depositing a cladding layer with negative thermo-optic coefficient such as polymer or TiO_2 [70, 94]. However, polymers are not CMOS compatible, and the selective deposition of a negative thermo-optic cladding layer on the reference resonator requires a more complicated multi-mask fabrication process.

In this chapter, a novel CRR device that can help simultaneously enhance both sensitivity and sensing range is proposed. For proof-of-concept, an SOI photonic temperature sensor utilizing this non-conventional CRR approach is developed for both temperature sensitivity and sensing range enhancement. Instead of using one of the ring resonators as a reference and thermally isolating the reference, two ring resonators with different temperature sensitivities and different FSRs were used as sensor resonators. Because the proposed approach does not require isolation of one of the ring resonators from a temperature input, the sensor fabrication can be achieved with a single-mask CMOS-compatible process. More importantly, since the enhanced FSR_{CRR} is obtained from the Vernier effect of two sensor resonators, the device can be tailored to enhance both the temperature sensitivity and sensing range, or to ultimately enhance one of the performance parameters (i.e., sensitivity or sensing range).

2.2 Principle of operation

Figure 2.1 shows the schematic of the proposed CRR temperature sensor operation. Ring 1 is designed to have a smaller temperature sensitivity (i.e., $S_1 < S_2$) and a larger FSR compared to Ring 2 (i.e., $FSR_1 > FSR_2$). This is achieved by using different ring waveguide widths and ring radii [Figures 2.1 (a) and 2.1 (b)]. Furthermore, temperature sensing is achieved by monitoring the position of the envelope peak of the output transmission spectrum [Figure 2.1 (c)] (sensitivity of S_{CRR}). This will help compensate the sensor resolution degradation induced by monitoring the discrete shift of the major resonance peak [72]. To better determine the envelope of the output transmission spectrum, the difference (ΔFSR) in FSRs of the two ring resonators should be smaller than the full-width half-maximum (FWHM) of the resonance peak [73].

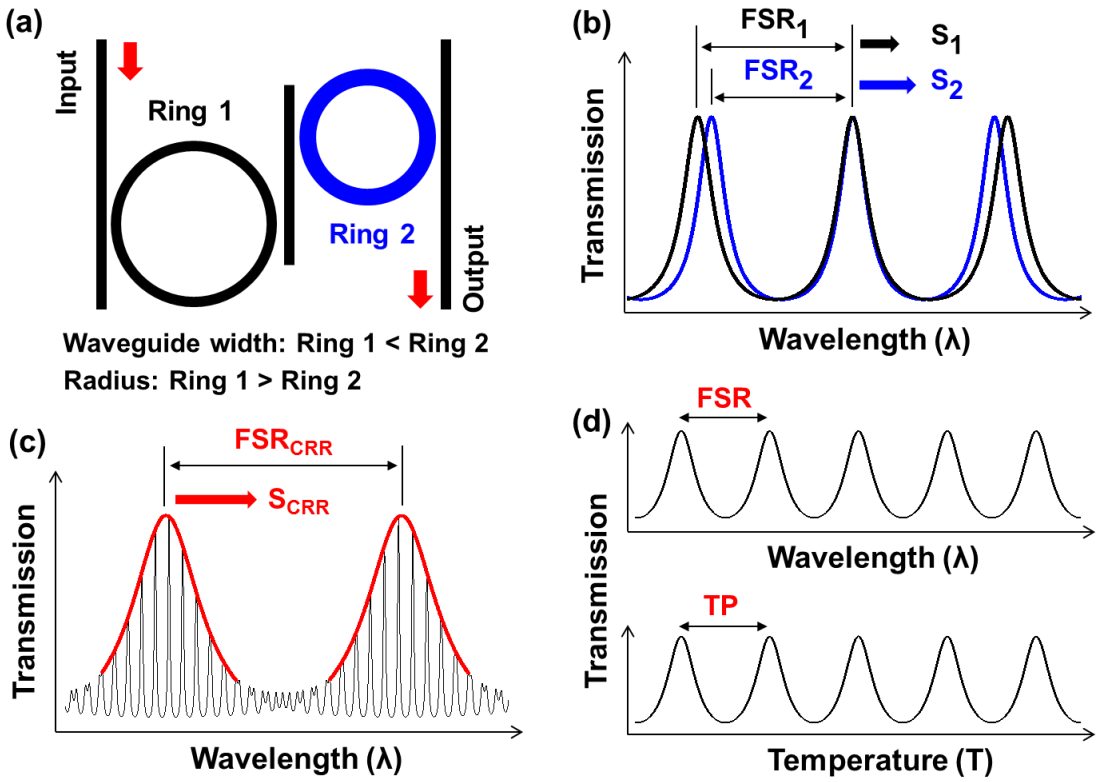

Figure 2.1 (a) Schematic of the CRR temperature sensor operation. (a) Cascaded configuration of Rings 1 and 2. Transmission spectra (b) at the drop ports of the two ring resonators, and (c) at the output of the CRR. (d) Power output at the drop port of a single ring resonator as a function of wavelength and temperature.

As schematically shown in Figure 2.1 (d), the power output at the drop port of each individual ring resonator is a periodic function of both wavelength (λ) and temperature (T). When the temperature changes by a temperature period (TP), the resonance wavelength of a single ring resonator will shift by one FSR. Thus, the temperature sensitivity of each individual ring resonator can be written as

$$S_i = FSR_i / TP_i, \quad i = 1, 2. \tag{2.2}$$

Note that the temperature period determines the temperature sensing range. For a CRR sensor, the temperature period TP_{CRR} is obtained as $\frac{TP_1 TP_2}{TP_1 - TP_2}$. When TP_1 and TP_2 are

close, the temperature sensing range of the CRR sensor will be much larger than that of each individual ring resonator. Furthermore, the sensitivity (S_{CRR}) of the CRR sensor can be expressed as

$$S_{CRR} = FSR_{CRR} / TP_{CRR} = \frac{FSR_1 FSR_2}{FSR_1 - FSR_2}\left(\frac{S_2}{FSR_2} - \frac{S_1}{FSR_1}\right). \quad (2.3)$$

When the two ring resonators have different sensitivity, the SCRR will be enhanced. Based on Equations (2.2) and (2.3), we can define the overall figure of merit (FOM) of the CRR sensor as the amplification of FSR compared with that of a single ring resonator:

$$FOM = \frac{S_{CRR}}{S_i}\frac{TP_{CRR}}{TP_i} = \frac{FSR_{CRR}}{FSR_i}, \qquad i = 1, 2. \quad (2.4)$$

Equation (2.4) indicates that the FOM represents the product of the sensitivity enhancement and the sensing range enhancement. Therefore, by using the proposed CRR sensor design, the sensitivity and sensing range can be enhanced simultaneously.

In general, the FOM can be enhanced by increasing the FSR_{CRR}, rendering the capability of enhancing both the sensitivity and the sensing range. However, depending on the applications, it is possible to use the FOM for ultimately enhancing only one performance parameter. In other words, the performance of the CRR sensor can be tailored to either solely enhance the sensitivity or sensing range, or both. According to Equation (2.3), for given FSR_1 and FSR_2, the key to tailor the sensor performance is $S_2/FSR_2 - S_1/FSR_1$ (i.e., the sensitivity difference (ΔS) between the two single ring resonators). The larger the ΔS, the higher the sensitivity enhancement. However, increasing the ΔS will compromise the sensing range enhancement. On the other hand, the enhancement of sensing range can be achieved by decreasing the ΔS at the expense

of reducing the sensitivity enhancement. At a given S_2, the maximum S_{CRR} will be achieved when the S_1 is zero, which represents the case of a conventional CRR sensor; while the maximum sensing range will be achieved when the S_1 is the same as the S_2 (there will be no sensitivity enhancement in this case). Therefore, compared with a conventional CRR sensor, our CRR sensor allows more flexibility to tailor the sensitivity and sensing range.

2.3 Sensor design

For an SOI device, the temperature sensitivity and FSR of each individual ring resonator can be controlled by changing the waveguide width and ring radius. The temperature sensitivity is related to the thermo-optic effect and thermal expansion of the ring waveguide [48]:

$$S = \frac{d\lambda_{res}}{dT} = \frac{\lambda_{res}}{n_g}\left(\frac{\partial n_{eff}}{\partial T} + n_{eff}\alpha_{Si}\right), \tag{2.5}$$

where n_{eff} is the effective index of the waveguide and α_{Si} is the coefficient of thermal expansion of silicon. The group index of the waveguide n_g is [56]

$$n_g = n_{eff} - \lambda\left(\frac{\partial n_{eff}}{\partial \lambda}\right). \tag{2.6}$$

Note that α_{Si} (2.5×10^{-6} /°C [19]) is ~100 times smaller than the thermo-optic coefficients of silicon and silicon dioxide (1.86×10^{-4}/°C and 1.0×10^{-5}/°C, respectively [48]). Therefore, the temperature sensitivity is dominated by the thermo-optic effect (i.e., $\partial n_{eff}/\partial T$), which is closely related to the mode confinement of the waveguide [70, 71]. The mode confinement can be controlled by changing the waveguide geometric parameters. For an SOI device with a fixed waveguide thickness, the mode confinement

increases with the waveguide width. Figure 2.2 shows the finite-difference time-domain (FDTD) simulations performed for a single ring resonator with a 210 nm-thick waveguide at 1550 nm at the room temperature, where the refractive indices of silicon and silicon dioxide were 3.48 and 1.45, respectively. Both $\partial n_{eff}/\partial T$ and ng increase with the waveguide width for the fundamental quasi-TM mode [Figure 2.2 (a)]. However, for the fundamental quasi-TE mode, as the waveguide width increases, $\partial n_{eff}/\partial T$ and ng first increase, then $\partial n_{eff}/\partial T$ saturates and n_g decreases slightly. As a result, for both modes, the temperature sensitivity is shown to increase with the waveguide width but with slightly different trends [Figure 2.2 (b)]. The FSR is determined by the ring radius and waveguide width. For a chosen waveguide width, n_g is fixed, and thus the FSR can be controlled by changing the ring radius [56]

$$FSR = \frac{\lambda_{res}^2}{n_g 2\pi R}, \tag{2.7}$$

where R is the ring radius. Figure 2.2 (c) shows the FSR as a function of a ring radius at a resonance wavelength of 1550 ± 0.05 nm. The temperature period TP (i.e., the sensing range) of a ring resonator is related to its FSR and temperature sensitivity, and therefore, for a chosen waveguide width it is determined by the ring radius [Figure 2.2 (d)].

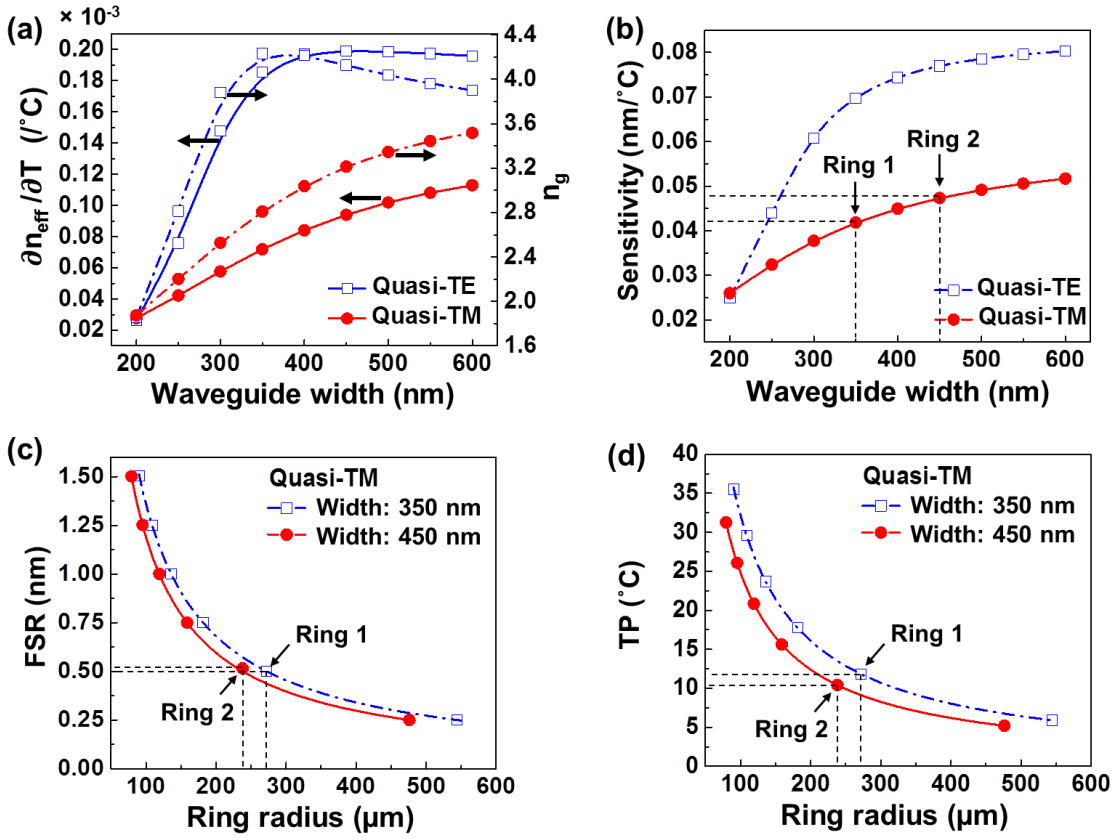

Figure 2.2 (a) $\partial n_{eff}/\partial T$, n_g, and (b) temperature sensitivity of a ring resonator as a function of waveguide width. (c) FSR and (d) TP as a function of ring radius with 350 nm and 450 nm wide waveguides at the quasi-TM mode. FDTD simulation and analytical calculation were performed at 1550 nm. The waveguide thickness is 210 nm.

Based on the above simulation results, a CRR temperature sensor with desired sensitivity/sensing range enhancement can be developed. A proof-of-concept temperature sensor was designed to operate at the fundamental quasi-TM mode for less susceptibility to waveguide sidewall roughness induced power attenuation. Considering the single mode operation and optical confinement of the waveguide, the waveguide widths of Rings 1 and 2 were chosen to be 350 nm and 450 nm, respectively. Then, based on the simulations [Figure 2.2 (b)], the S_1 and S_2 were obtained to be 42.3 pm/°C and 48.0 pm/°C, respectively. The FSR_{CRR} was chosen to be ~17 nm, so that it

can be smaller than the spectral width of the broadband light source to be used in the experiment. Furthermore, the FSR_1 and FSR_2 were set to be 0.515 nm and 0.500 nm, respectively, rendering the sensing ranges of 12.17 °C and 10.42 °C [Figure 2.2 (d)]. It was taken into the consideration that ΔFSR should be less than the FWHM of a single resonator. For an SOI ring resonator with a typical Q factor of ~10,000, the FHWMs were estimated to be ~0.155 nm at 1550 nm. Based on the FSRs, the corresponding radii of Rings 1 and 2 were determined to be 271.94 μm and 232.23 μm, respectively [Figure 2.2 (c)]. The bus-to-ring waveguide coupling gaps were designed to obtain critical coupling by using FDTD simulations (Gaps of 310 nm and 250 nm were obtained for Rings 1 and 2, respectively). From Equation (2.3), the sensitivity and sensing range of the designed CRR temperature sensor were estimated to be 238.0 pm/°C and 72.13 °C, respectively. A sensitivity enhancement of 5.0 times and sensing range enhancement of 6.9 times compared to Ring 2 (i.e., FOM of 34.5) were expected.

Note that in the above design values, the dispersion was not taken into account. To investigate the effect of dispersion on the sensitivity and sensing range, we obtained n_{eff} with dispersion for Rings 1 and 2 using FDTD simulations [Figure 2.3 (a)]. Here, only the waveguide dispersion was considered, since it dominates the material dispersion in a high refractive-index contrast SOI waveguide [95]. Using the obtained n_{eff} and setting the reference at the room temperature (i.e., $\Delta T = 0$), the envelope peak of interest was located at 1550 nm and the FSR_{CRR} was determined to be 16.87 nm [Figure 2.3 (b)]. The temperature-dependent envelope peak shift of the CRR temperature sensor was calculated [Figure 2.3 (c)]. The sensitivity and sensing range were obtained to be 229.6 pm/°C and 73.48 °C, respectively, which compare well with

those values obtained by neglecting the dispersion. Furthermore, to investigate the effect of the bus-to-ring coupling conditions on the sensor, the transmission spectra at different coupling conditions were obtained [Figure 2.3 (b)]. The results show a trade-off between the envelop peak sharpness and the transmission power. The critically-coupled CRR sensor renders a sharper envelope peak than the over-coupled CRR sensor and a higher transmission power than the under-coupled CRR sensor. The sharp envelope peak can help reduce the envelope fitting error, and thus improve the sensor resolution. For example, the fitting errors were ~3.2 pm for the over-coupled condition and ~1.2 pm for the critically-coupled and under-coupled conditions. However, the envelope peak locations and FSR_{CRR} of both the over-coupled and under-coupled CRR sensors are the same as the critically-coupled CRR sensor. Therefore, the coupling condition of the CRR sensor does not affect the sensitivity and sensing range.

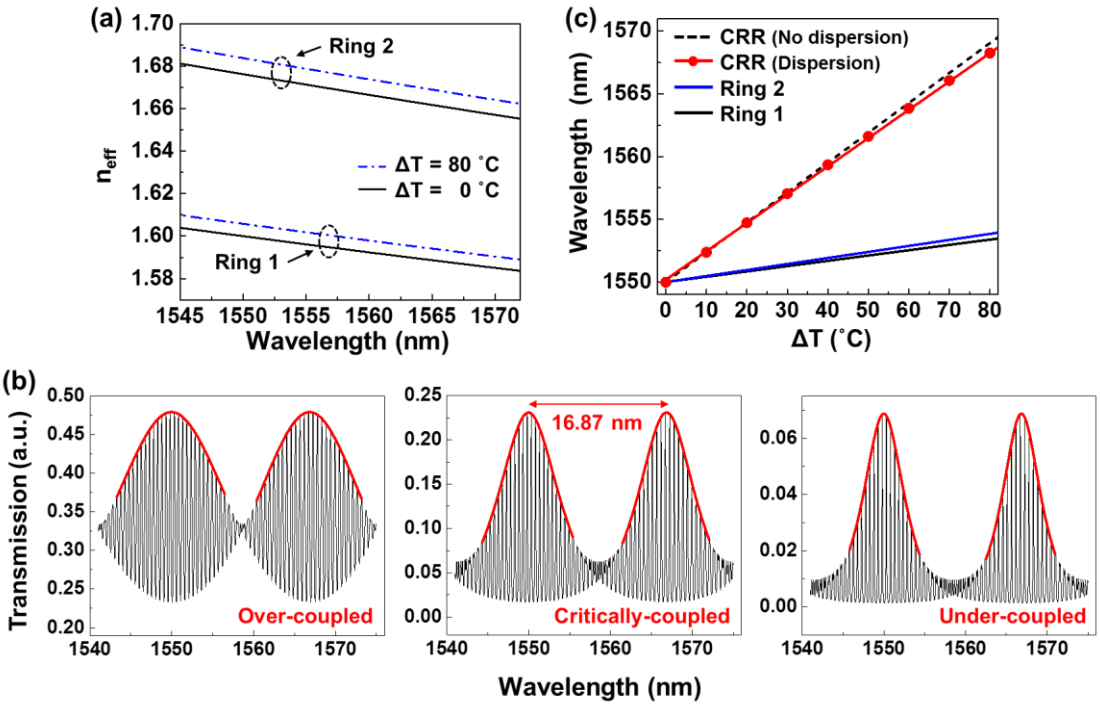

Figure 2.3 (a) FDTD simulation results of n_{eff} for Rings 1 and 2 as a function of wavelength. The waveguide thickness is 210 nm. (b) Transmission spectra of the over-coupled, critically-coupled, and under-coupled CRR sensors at the room temperature (ΔT = 0 °C). (c) Calculated temperature-induced peak shifts of the designed CRR temperature sensor and Rings 1 and 2.

2.4 Sensor fabrication and experimental setup

The CRR temperature sensor was fabricated by using an SOI wafer with a 210 nm-thick silicon layer and a 3 µm-thick buried oxide layer. The SOI wafer was spin-coated with poly(methyl methacrylate) (PMMA) followed by e-beam lithography for patterning the ring and bus waveguides. A 20 nm-thick chromium (Cr) layer was then deposited on top of the patterned PMMA layer followed by the Cr lift-off process. The ring and bus waveguides were formed by the inductively coupled plasma reactive ion etching process. After releasing the Cr etch mask, a 1 µm-thick oxide cladding layer was deposited by the plasma-enhanced chemical vapor deposition. Figure 2.4 shows the fabricated sensor. The sensor was tested in the quasi-TM mode. A broadband light

source (M1702, AT&T) and a 60 pm resolution OSA (86142B, Agilent) were used to obtain the transmission spectrum of the sensor. The temperature control was achieved with a micro-hotplate and a k-type thermocouple (CO1, Omega).

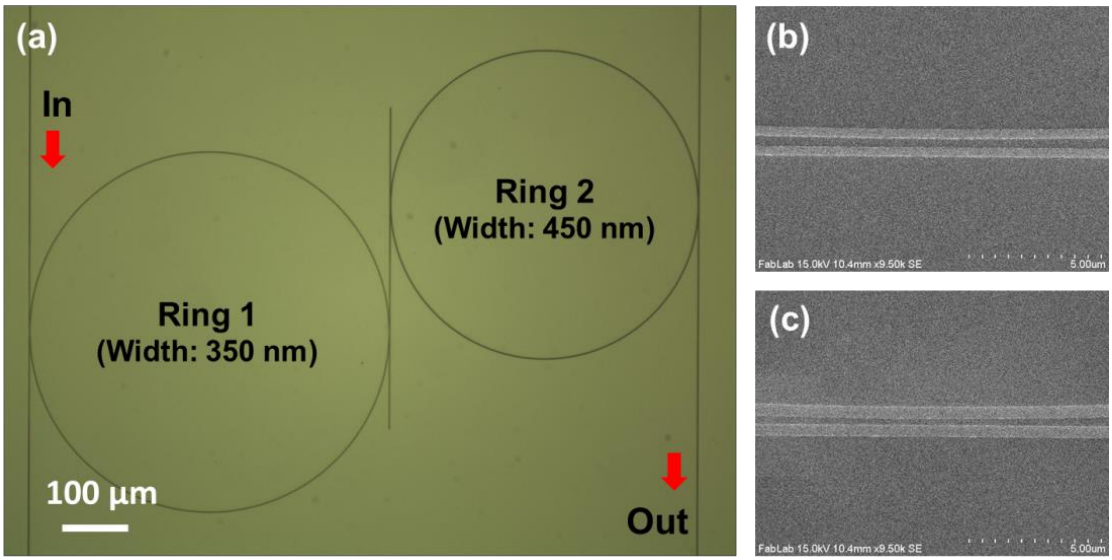

Figure 2.4 (a) Optical microscope image of the fabricated CRR temperature sensor. SEM images of the ring and bus waveguides in the coupling region for (b) Ring 1 and (c) Ring 2.

2.5 Results and discussion

The measured transmission spectra of the two ring resonators at the pass port are shown in Figure 2.5 (a). The Q factors of Rings 1 and 2 were 9,000 and 10,000, respectively. The FSR_1 and FSR_2 were ~0.515 nm and ~0.500 nm, respectively. The difference in FSRs (ΔFSR = ~0.015 nm) was 10 times smaller than the measured FWHM (~0.145 nm). The resonance wavelength shifts of each individual ring resonator as a function of temperature were measured, which exhibited a good linearity [Figure 2.5 (b)]. The temperature sensitivities of Rings 1 and 2 were determined to be 38.9 pm/°C and 46.6 pm/°C, respectively, which were slightly lower than the designed values (42.3 pm/°C and 48.0 pm/°C, respectively). The discrepancies are believed to

result from the differences in the device geometric parameters and material properties (i.e., refractive indices and thermo-optic coefficients of silicon and silicon dioxide) between the experiment and simulations.

Furthermore, the performance of the CRR temperature sensor was characterized. The envelope peak position was determined by the Lorentzian fit of the output transmission spectrum. At the room temperature (23.74 °C), the envelope peak was located at ~1546 nm and the FSR_{CRR} was 16.63 nm [Figure 2.5 (c)]. The shift of the envelope peak with respect to temperature was clearly observed [Figures 2.5 (c) and 2.5 (d)] and a good linearity was obtained [Figure 2.5 (b)]. The sensitivity and sensing range were 293.9 pm/°C and 56.85 °C, which exhibit an enhancement of 6.3 times and 5.3 times compared with those of Ring 2. The corresponding FOM was 33.4. The resolution of the CRR temperature sensor was determined from the sensitivity and envelope peak fitting error (i.e., sensor resolution = envelope peak fitting error / sensitivity) [73]. Based on the measured transmission spectrum, the envelope peak fitting error was determined to be 53 pm, and hence, the resolution of the CRR temperature sensor was obtained as 0.18 °C. The resolution can be improved by further enhancing the sensitivity and/or reducing the fitting error. The error can be reduced by using a two-step fitting (i.e., constituent peaks fitting and envelope fitting) and a higher resolution spectrum measurement system. For example, an 18 pm fitting error was demonstrated in [73] by using the two-step fitting and a tunable laser with a 1 pm resolution.

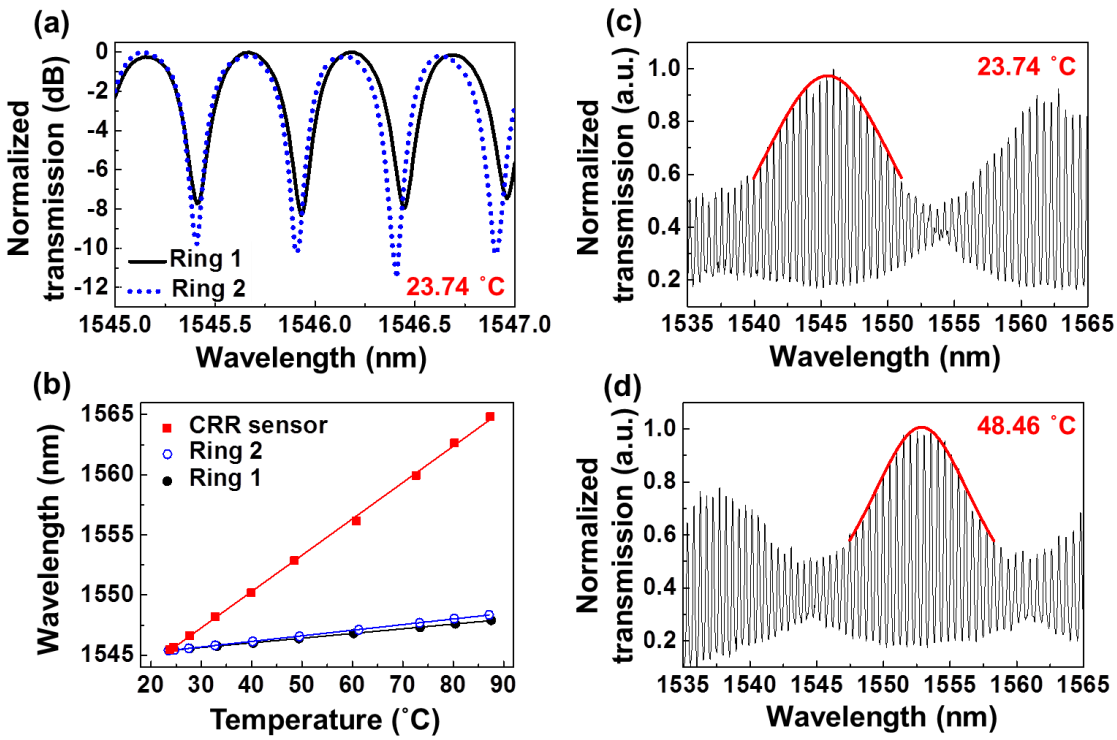

Figure 2.5 (a) Normalized transmission spectra at the pass port of Rings 1 and 2 at 23.74 °C. (b) Resonance wavelength shift of Rings 1 and 2 and the envelope peak shift of the CRR temperature sensor as a function of temperature. (c) and (d) Normalized transmission spectra of the CRR temperature sensor and the corresponding envelopes by the Lorentzian fit at 23.74 °C and 48.46 °C.

Although the proof-of-concept sensor only demonstrated a sensing range of 56.85 °C, it should be noted that for the obtained FOM of 33.4, the sensing range of the sensor can be ultimately enhanced to be ~358 °C when the S_1 is designed to be equal to the S_2, and there will be no sensitivity enhancement (i.e., the sensitivity will be 46.6 pm/°C, same as that of each single ring resonator). On the other hand, for the same FOM, a larger sensing range can be obtained without compromising the sensitivity by reducing the ring radii. For example, if the radii of Rings 1 and 2 are reduced to 10 % of the current values (i.e., 27.2 μm and 23.2 μm), the FSRs and thus the sensing ranges of Rings 1 and 2 will increase by ten times. Since both the sensing

range enhancement and sensitivity enhancement will remain unchanged, a sensing range of 568.5 °C with a sensitivity of 293.9 pm/°C will be achievable with the CRR sensor. In this case, a light source with a larger spectral width is required for the full-range sensing since the FSR_{CRR} will also increase by ten times. Furthermore, with the designed waveguide widths, if the quasi-TE mode operation is used, the achievable ΔS will be ~27 % larger than that of the quasi-TM mode operation, which can help further enhance the sensitivity. However, for the quasi-TE mode operation, precise fabrication of the waveguides is required to decrease the sidewall roughness so that the power attenuation can be reduced. The sensor performance adjustment can be achieved by tailoring the in-plane geometric parameters of Rings 1 and 2 (i.e., waveguide widths and ring radii). The out-of-plane geometry and core/cladding layer materials are the same for Rings 1 and 2, which enables to fabricate the sensor with a single-mask CMOS-compatible process.

2.6 Summary

In summary, a CRR-based, silicon photonic temperature sensor with the capability of enhancing both sensitivity and sensing range was developed. The CRR temperature sensor was fabricated by using a single-mask CMOS-compatible process. In experiment, the sensor was demonstrated to have an enhancement of 6.3 times in the sensitivity and 5.3 times in the sensing range compared to the single ring resonator sensor. Furthermore, it was theoretically shown that either the sensitivity or the sensing range can be ultimately enhanced by tailoring the ΔS, and both the sensitivity and the sensing range can be enhanced by increasing the FOM. As pointed by previous studies [72, 73], owing to the sensitivity enhancement of the proposed temperature sensor, one

can potentially use an on-chip, low resolution micro optical spectrometry such as an arrayed waveguide grating [44] for sensor interrogation without significant compromise in resolution. This can help reduce the size and cost of the photonic temperature monitoring system. On the other hand, it is possible to tailor the sensor to obtain an extended temperature sensing range, so that it can be utilized to monitor large temperature changes.

Chapter 3: High-speed optical sensor interrogator with a silicon-ring-resonator-based thermally tunable filter

3.1 Introduction

Compact, real-time optical sensing systems are highly desirable in applications such as wireless sensor networks [26] and portable medical devices [96]. To achieve such a system, high speed, on-chip optical sensor interrogators are needed to replace the conventional bulky and slow interrogators.

Current on-chip optical interrogators are mainly based on two approaches: i) spectrometers based on diffraction gratings and photodetector arrays and ii) tunable filter based devices. The former often makes use of a planar diffraction grating such as arrayed waveguide gratings [44] and echelle gratings [65], to acquire spectrum in parallel, which are then detected by using a large array of high-speed photodetectors (PDs). While this approach can achieve fast interrogation, it often requires a large device footprint. The latter approach makes use of a tunable wavelength filter and a single PD to tune the resonance wavelength in serial, and then detect the time-domain signal converted from the spectral information. The resolution of these interrogators is determined by the linewidth of the tunable wavelength filter [52]. By using a narrow-linewidth filter, fine-resolution interrogation can be realized with a small device footprint, and multiple optical sensors can be simultaneously interrogated [26]. Most tunable-filter-based interrogators are based on micro-electro-mechanical-system

(MEMS) Fabry-Perot (FP) interferometers, employing a movable mirror [38] or deflectable membrane [52].

Recently, silicon-ring-resonator-based thermally tunable filters (SRRTFs) have received much attention [61-63, 97-99] due to several features. First, compared with MEMS FP tunable filters, SRRTFs render a simple fabrication process as well as better long-term reliability, since thermo-optic tuning does not require any moving part. Second, the large thermo-optic coefficient and high thermal conductivity of silicon enable SRRTFs to achieve efficient, wide-range wavelength tuning. Third, high quality-factor (Q-factor) ring resonators provide excellent wavelength selectivity, which enables fine-resolution interrogation. Fourth, the high refractive-index contrast of the silicon-on-insulator (SOI) structure can help achieve an ultra-compact device. Lastly, the CMOS compatible fabrication process of these filters opens up the opportunity for monolithic integration of all the necessary photonic components, including SRRTFs, light emitting diodes, PDs, couplers, and waveguides for optical interconnection, which could ultimately lead to miniaturization and cost reduction of optical sensor interrogators.

However, most of reported SRRTF interrogators suffer from slow interrogation speed (less than a few Hz) [61-63, 97], which makes them not suitable for monitoring of dynamic parameters. Recently, an enhanced speed of 0.8 kHz with an SRRTF-based swept wavelength laser was demonstrated by Li et al. [100]. In this chapter, a 100 kHz of high-speed interrogation system based on an SRRTF is reported. The high-speed interrogation system can be used for real-time monitoring of dynamic parameters.

For proof-of-concept, a fiber Bragg grating (FBG) sensor under dynamic temperature change (200 Hz) is interrogated with such a system.

3.2 Principle of operation

Figure 3.1 (a) shows the schematic of the proposed interrogation system. It consists of a broadband light source, a polarization controller, an SRRTF, and a PD. The SRRTF scans over the reflection spectrum of the sensor [Figures 3.1 (b) and 3.1 (c)]. Assuming the wavelength scanning of the SRRTF is much faster than the sensor response, the time-domain output of the PD [Figure 3.1 (d)] is

$$P(t) = \int S(\lambda)F(\lambda - \Delta\lambda_{res}(t))d\lambda, \tag{3.1}$$

where S(λ) [Figure 3.1 (b)] and F(λ) [Figure 3.1 (c)] are the spectra of the sensor and the SRRTF, respectively, and $\Delta\lambda_{res}(t)$ is the time-dependent resonance wavelength (λ_{res}) shift of the SRRTF. Here, we utilize the nonlinear transient response of the SRRTF [Figures 3.1 (f) and 3.1 (g)] to a square-wave input [Figure 3.1 (e)] to enhance the interrogation speed. We set the operating frequency, f, of the SRRTF, so that 1/2f is close to the thermal response time, τ. Then, the scan of the λ_{res} over the entire spectral range, Δλ, is performed twice during 2τ, which renders the interrogation speed of 1/2τ (i.e., 2f). The Δλ is determined by the amplitude of the input voltage. The sensor spectrum can then be demodulated from the P(t) and $t - \lambda_{res}$ relation of the SRRTF. The demodulated sensor spectrum is close to S(λ) if the full width at half-maximum (FWHM) of the resonance is sufficiently narrow compared to that of the sensor.

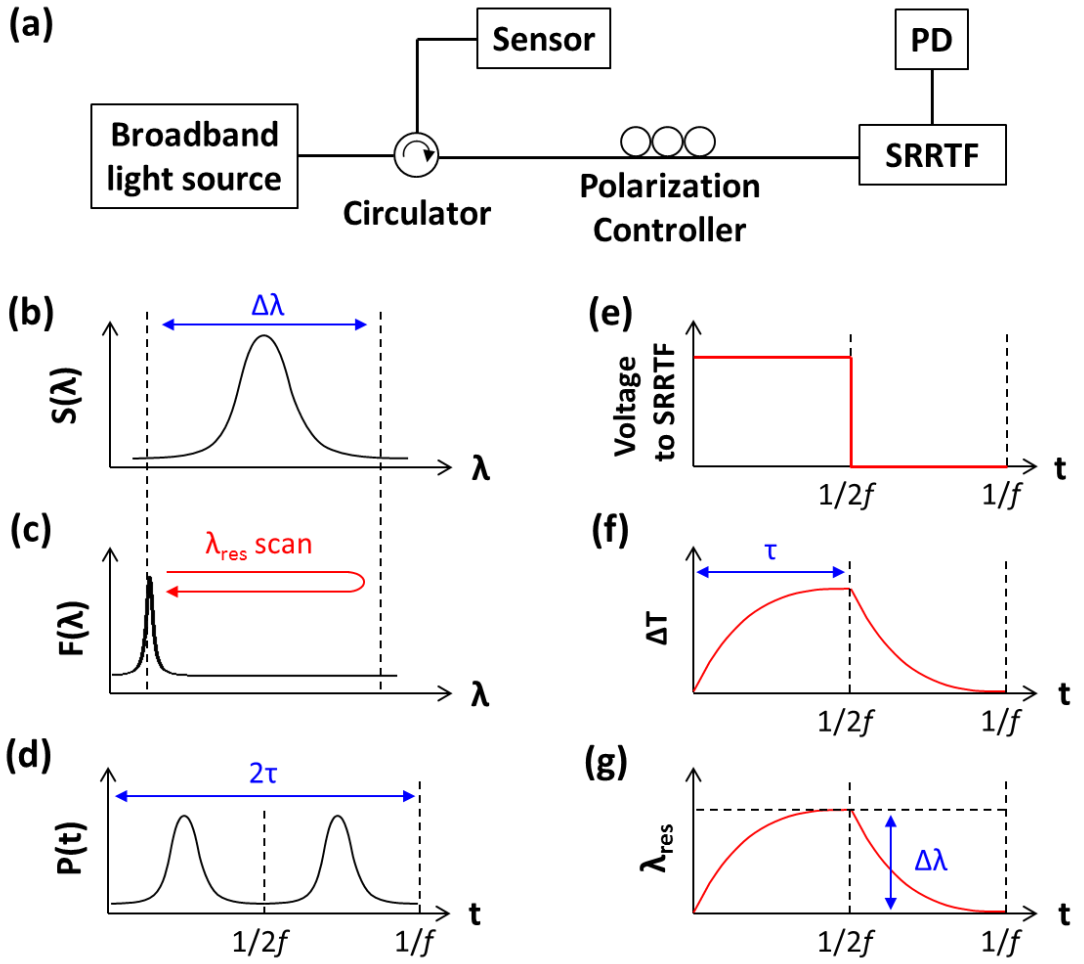

Figure 3.1 (a) Schematic of the high-speed optical sensor interrogation system based on the SRRTF. (b) and (c): spectra of the sensor and SRRTF, respectively. (d) Time-domain output of the PD. (e) Operation voltage waveform of the SRRTF. (f) Temperature change and (g) resonance wavelength of the SRRTF under the input voltage.

The t – λ_{res} relation is determined by the thermal sensitivity (i.e., $d\lambda_{res}/dT$) of the SRRTF and time-dependent temperature change from a reference temperature [i.e., $\Delta T(t)$] as

$$\lambda_{res}(t) = \lambda_{res,0} + \frac{d\lambda_{res}}{dT}\Delta T(t), \tag{3.2}$$

where $\lambda_{res,0}$ is the resonance wavelength at the reference temperature. The thermal sensitivity is determined by the waveguide properties as

$$\frac{d\lambda_{res}}{dT} = \frac{\lambda_{res}}{n_g}\left(\frac{\partial n_{eff}}{\partial T} + n_{eff}\alpha_{Si}\right), \tag{3.3}$$

where n_{eff} and n_g are the effective and group indices of the waveguide, respectively, and α_{Si} is the thermal expansion coefficient of silicon.

The time-dependent temperature change is determined by the SRRTF structure. For a rectangular SOI ring waveguide with a narrow-width micro-heater over the top oxide cladding [Figure 3.2 (a)], the temperature profile around the micro-heater obtained from finite-element-method (FEM) simulations has contours close to a semicircle [Figure 3.2 (b)]. Therefore, the time-dependent temperature change of the SOI waveguide (i.e., SRRTF) can be approximated by the series solution of the heat conduction equation in cylindrical coordinates, and the normalized temperature change to a step thermal input is expressed as [101, 102]

$$\Delta T_{Norm}(t) = 1 - \sum_{n=1}^{\infty} A_n J_0(\delta_n r_{WG}) \exp(-\delta_n^2 \alpha t), \tag{3.4}$$

where A_n are coefficients, r_{WG} is the gap between the micro-heater and waveguide, δ_n are the eigenvalues of the heat equation, and α is the oxide thermal diffusivity. Figure 3.2 (c) shows the normalized temperature obtained from FEM, which is curve-fitted to the series solutions. The root-mean-square error (RMSE) of the curve fitting decreases with the number of the exponential terms and converges to 0.0014. In the 10% – 90% rise-time period, the errors of the 3-term exponential function are less than 0.0082. Therefore, if the thermal sensitivity of the SRRTF is constant, the $t - \lambda_{res}$ relation can be described by using the 3-term exponential function.

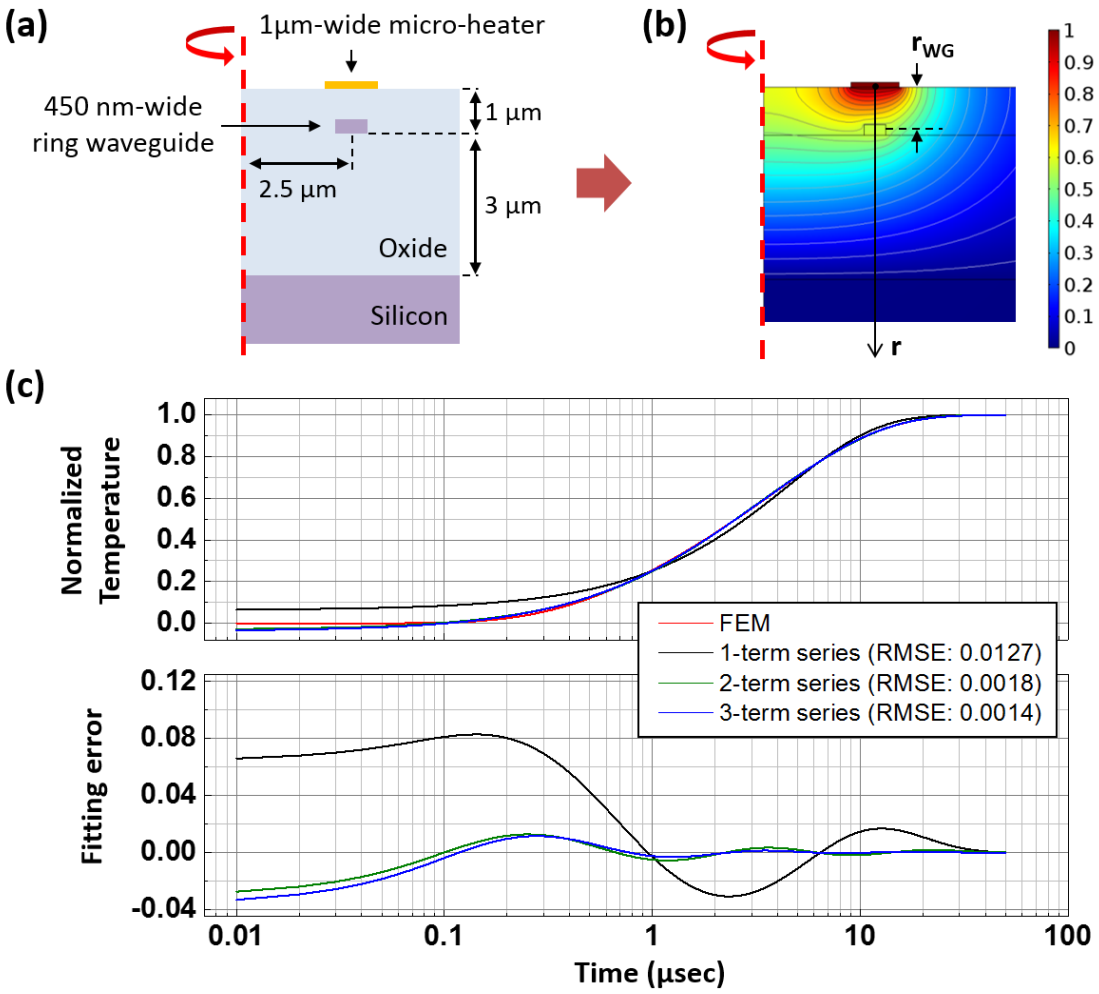

Figure 3.2 (a) Schematic of the SRRTF cross-section structure (ring waveguide: 450 nm × 220 nm, micro-heater: 1 µm × 100 nm). (b) Normalized, steady-state temperature profile obtained from the FEM simulation. (c) Normalized, time-dependent temperature change of the SRRTF waveguide under a step thermal input and errors of the series solutions from the FEM simulation.

3.3 Fabrication of the SRRTF

For proof-of-concept, an SRRTF was fabricated and used in the proposed interrogation system. A silicon ring resonator was fabricated using an SOI wafer with a 3 µm buried oxide layer. The ring radius was 2.5 µm and the width and thickness of the waveguide were 450 nm and 220 nm, respectively [Figure 3.3 (a)]. For the top cladding layer, a 1 µm oxide film was deposited. A chromium (Cr) micro-heater for

thermo-optic tuning was then fabricated on top of the ring resonator. The width and thickness of the micro-heater were 1 µm and 100 nm, respectively [Figure 3.3 (b)].

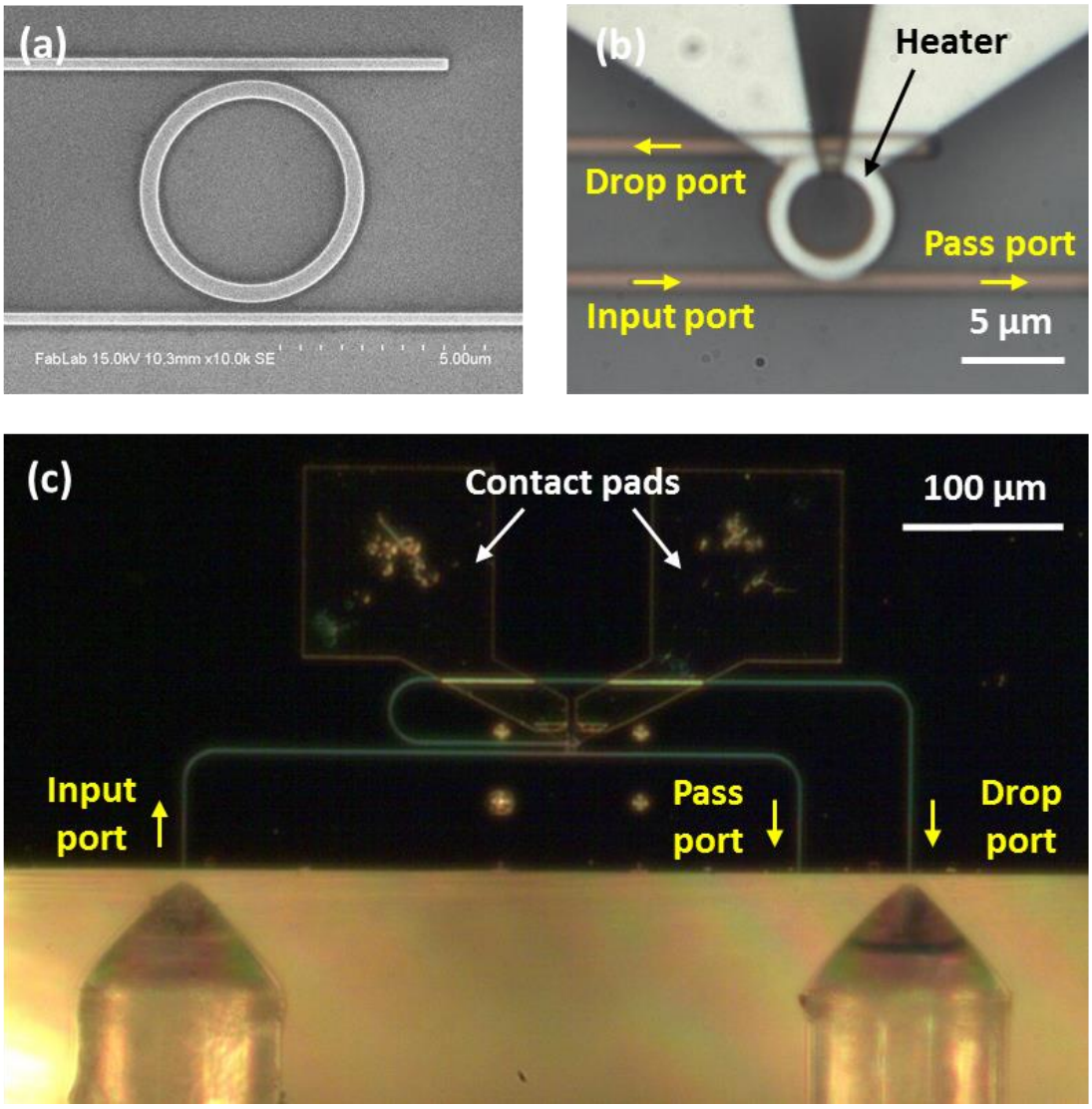

Figure 3.3 (a) SEM image of the silicon ring resonator and (b) optical microscopy image of the Cr micro-heater on top of the silicon ring resonator. (c) Optical microscopy image showing the SRRTF chip with tapered-lensed fibers.

3.4 Results and discussions

3.4.1 Characterization of the SRRTF

The fabricated SRRTF was first characterized by using a tunable laser and a PD. The input light was controlled to be TE-polarized since a quasi-TE mode operation renders higher thermal sensitivity. Coupling the TE-polarized light into and from the SRRTF chip was achieved using a tapered-lensed fiber and an inverse taper coupler, as shown in Figure 3.3 (c). The tapered-lensed fiber had 2.5 μm of spot diameter and 14 μm working distance. The inverse taper coupler had 120 nm of taper tip width and 40 μm of length, whose coupling loss was reported to 6.0 ± 0.4 dB at 1550 nm [103]. First, the steady-state response of the SRRTF was characterized. The room temperature λ_{res} and free-spectral-range (FSR) of the SRRTF were obtained as 1535.49 nm and 35.37 nm, respectively [Figure 3.4 (a)]. The drop port insertion loss was ~13.5 dB at the λ_{res} (bus waveguide length: 820 μm), and the pass port insertion loss was ~11.3 dB at 1540 nm (bus waveguide length: 445 μm). The difference in the transmission power at the two resonances (1535.49 nm and 1570.86 nm) was ~0.3 dB. The λ_{res} increased linearly with the heating power and the wavelength tuning efficiency was 1.21 nm/mW [Figure 3.4 (b)]. Due to the linear relationship between the heating power and temperature of micro-heaters [104], the thermal sensitivity of the SRRTF was believed to be constant over the tuning range.

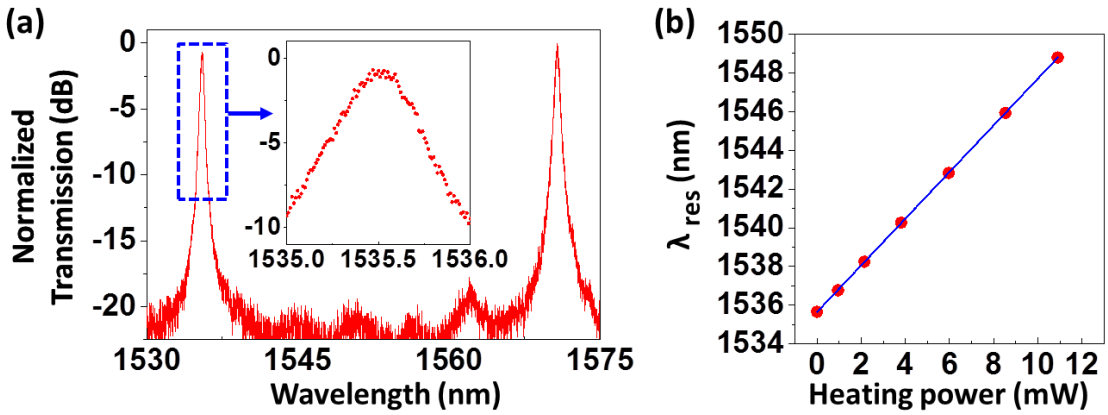

Figure 3.4 (a) Normalized transmission spectrum at the drop port of the fabricated SRRTF. The inset shows the zoom-in resonance peak, indicating a clearly defined single peak. (b) Resonance wavelength as function of heating power.

The transient response of the SRRTF (i.e., the t – λ_{res} relation) was obtained by operating the SRRTF (i.e., the micro-heater) with an operating frequency of 10 kHz (and 50 kHz) and a driving voltage of 3.38 V (~10.9 mW) of square-wave input voltage. The time-domain output of the PD was recorded at different wavelengths of the tunable laser (λ_{TL}) by using a data acquisition system with 16-bit resolution and 62.5 MS/s speed. At the operating frequencies of 10 kHz [Figure 3.5 (a)] and 50 kHz [Figure 3.5 (d)], the PD output was maximized when the λ_{res} coincided with the λ_{TL}. From these results, the time at the peak output of the PD for each λ_{TL} (i.e., λ_{res}) was determined. The measured t – λ_{res} results [Figures 3.5 (b) and 3.5 (e)] were then curve fitted by using a 3-term exponential function. The t – λ_{res} relation at 10 kHz [Figure 3.5 (b)] was used to obtain the maximum tuning range (~13.0 nm at 3.38 V) and the thermal response time τ of the SRRTF (12.8 μsec, 10 % – 90 % rise/fall time).

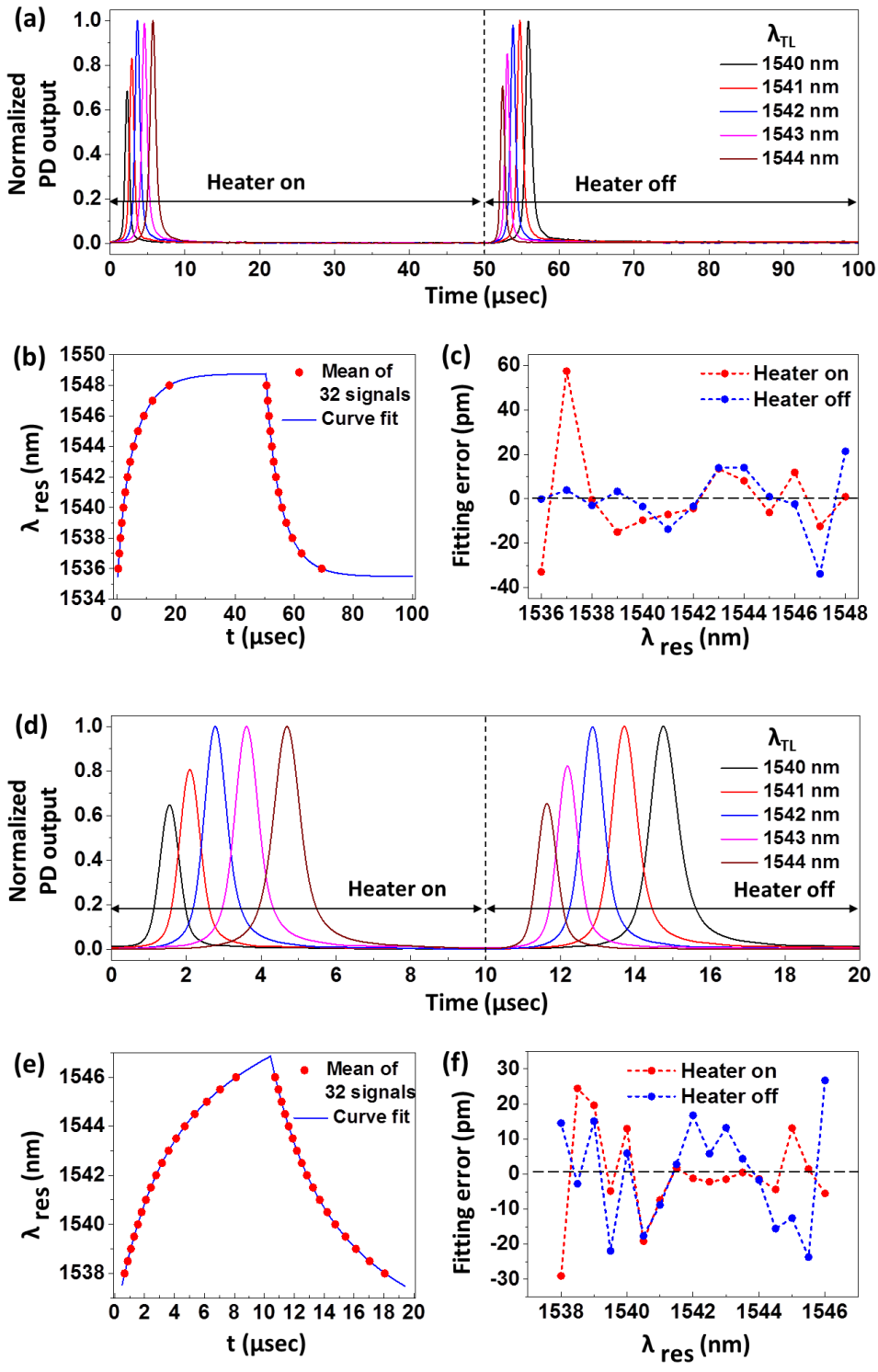

Figure 3.5 Transient response characterization. (a) and (d): normalized PD outputs as a function of time at different λ_{TL} at 10 kHz and 50 kHz operating frequencies, respectively. (b) and (e): measured $t-\lambda_{res}$ pairs and their curve fit, at 10 kHz and 50 kHz operating frequencies, respectively. (c) and (f): curve fitting errors at 3.38 V and operating frequencies of 10 kHz and 50 kHz, respectively.

As the interrogation is performed during both the heater-on and -off scans, the interrogation speed is twice of the operating frequency. Increasing the operating frequency helps enhance the interrogation speed. However, further increasing the operating frequency beyond $1/2\tau$ (i.e., ~40 kHz) reduces the tuning range. For example, the tuning range was reduced to be ~9.0 nm at the 50 kHz of operating frequency [Figure 3.5 (e)]. To enhance the interrogation speed without sacrificing the tuning range, the thermal response time should be reduced, which can be accomplished by decreasing the micro-heater width and the buried oxide layer thickness [105]. The interrogation range (i.e., tuning range) is determined by both the amplitude and operating frequency of the input voltage waveform. Ideally, by increasing the voltage amplitude to ~5.5 V (i.e., ~29.2 mW), the interrogation range increases to 35.37 nm, which is the maximum range limited by the FSR of the SRRTF. However, possible micro-heater failure at a high heating power could reduce this maximum range. The FSR can be further increased by reducing the ring radius, which, however, could increase the radiation loss and thus decrease the Q-factor. The interrogation accuracy is determined by the errors of the curve fitting for the $t - \lambda_{res}$ relations. Figures 3.5 (c) and 3.5 (f) show the fitting errors in the 10 % – 90 % of the tuning range. At 10 kHz, the RMSEs were 20 pm and 13 pm for the heater-on and -off scans, respectively, and the maximum errors were 57 pm and 33 pm for the heater-on and -off scans, respectively. At 50 kHz, the RMSEs were 12 pm (maximum 29 pm) and 14 pm (maximum 26 pm) for the heater-on and -off scans, respectively. Furthermore, the interrogation resolution (the minimum discriminable wavelength difference [106]), is determined by the FWHM of the

SRRTF. The measured FWHM for the fabricated device was 0.46 nm. It can be further improved by enhancing the Q-factor of the SRRTF.

3.4.2 Interrogation of FBG temperature sensors

The high-speed SRRTF interrogation system [Figure 3.1 (a)] was implemented for an FBG temperature sensor. The SRRTF was driven with a 50 kHz and 3.38 V of square-wave voltage signal. This renders an interrogation speed of 100 kHz and a range of ~9.0 nm. The Bragg wavelength (λ_{Bragg}) (~1539.8 nm at room temperature) was kept within the interrogation range. The FBG sensor was mounted on a MEMS hotplate, where the temperature was well controlled and monitored with a thermocouple. The time-domain PD outputs at different static temperatures are shown in Figure 3.6 (a). The outputs for the heat-off scans were converted into spectrum domain [Figure 3.6 (b)] by using the $t - \lambda_{res}$ relation of the SRRTF [Figure 3.5 (e)]. For comparison, the FBG sensor was also interrogated by using a tunable laser [Figure 3.6 (c)]. With both approaches, the temperature sensitivity of the FBG sensor was measured to be ~9.9 pm/˚C [Figure 3.6 (d)]. However, the spectra obtained from the SRRTF-based system rendered wider FWHMs. It mainly resulted from the wider linewidth of the SRRTF than that of the tunable laser. A higher Q-factor of the SRRTF will help achieve better interrogation resolution. Note that the peak position of the PD outputs is not affected by the Q-factor of the SRRTF. Furthermore, an FBG sensor under dynamic temperature change was interrogated with the SRRTF system. The MEMS hotplate was operated with a 200 Hz on/off speed, rendering a periodic temperature change with ~11 ˚C amplitude. The obtained time-domain response of λ_{Bragg} is shown in Figure 3.6 (e), with a 10 μs temporal resolution.

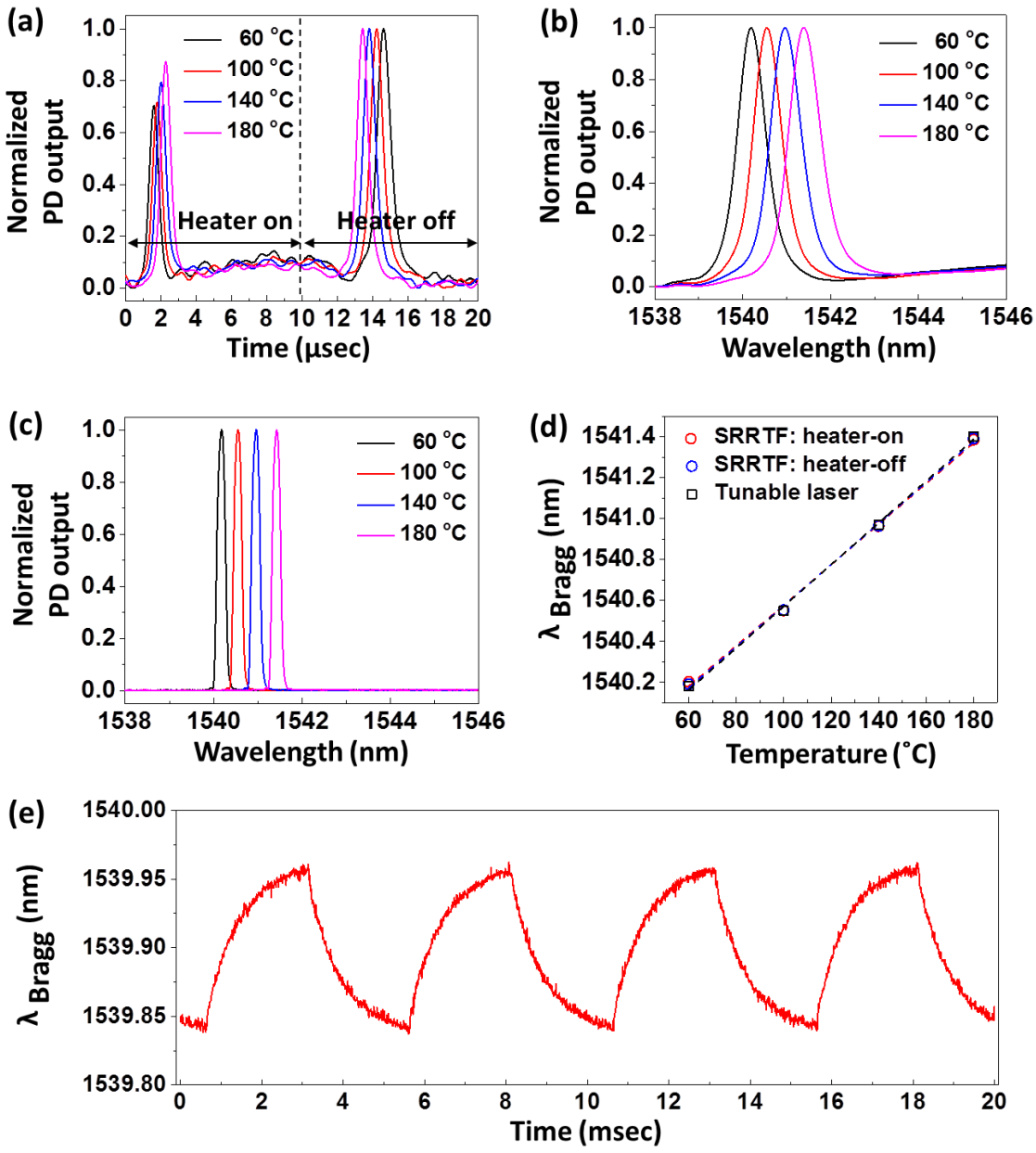

Figure 3.6 High-speed interrogation of a FBG sensor. (a) Time-domain PD outputs at different static temperatures. Reflection spectra of the FBG sensor interrogated by using (b) SRRTF and (c) a tunable laser system. (d) Measured λ_{Bragg} as a function of temperature. (e) Measured time response of λ_{Bragg} under a 200 Hz periodic temperature change (the resulting temperature change was ~11 ℃).

3.5 Summary

In summary, a high-speed sensor interrogation system using an SRRTF was investigated theoretically and experimentally. This system utilized the nonlinear transient response of the SRRTF and scanned the entire spectral range in its thermal response time. With the proof-of-concept SRRTF, an FBG temperature sensor was successfully interrogated at 100 kHz speed. This work will pave the way for realizing portable, compact optical sensing systems for real-time monitoring of dynamic parameters.

Chapter 4: High-speed and wide-range thermally tunable silicon ring resonator filter for simultaneous interrogation of multiplexed FBG sensors

4.1 Introduction

Thermally tunable silicon ring resonators have received much attention in integrated photonic sensing systems. Due to their advantages of high quality-factor (Q-factor), large phase shift, compact footprint, and CMOS compatible fabrication, they have been widely used as a wavelength tunable filter for sensor interrogation. Since the performance of such interrogation systems is primarily determined by the silicon-ring-resonator-based thermally tunable filter (SRRTF), enhancing the thermal and optical characteristics of the SRRTF has been of great interest.

A common approach for thermo-optic tuning of the silicon ring resonator is employing a metallic heater on top of the oxide cladding layer. While the fabrication process of such a structure is simple, it is not suitable for realizing fast tuning speed. For achieving a fast tuning speed, a thin oxide cladding layer is desirable [105]. However, reducing the top-oxide (TOX) and buried-oxide (BOX) layers to less than ~1μm is challenging due to the lossy metal and the mode radiation to the bulk silicon under the BOX layer. Moreover, the low thermal conductivity of the cladding oxide makes the ratio of the waveguide temperature change to the heater temperature change

(R, i.e., $\Delta T_{WG}/\Delta T_{Heater}$) small. Such a small R has hindered wide-range tuning due to a possible high-temperature failure of the heater.

To address these issues, the TOX layer was partially or entirely removed, and the heater was formed either in the interior silicon slab of the resonators (i.e., interior-ridge-ring resonator and disk resonator) for increasing the R [42, 100, 107] or in the ring waveguide by using PN junction and P-i-P junction for direct heating of the waveguide [108, 109]. However, such approaches have a limitation in reducing the resonator radius due to the possible Q-factor decrease. For example, the former requires a sufficient gap (larger than 1 μm) between the heater and the waveguide to avoid the absorption loss due to the lossy metal of the heater. The latter increases the waveguide bending loss due to the exterior silicon slab for the impurity doping. Note that ultracompact ring resonators have advantages of rendering a large free-spectral-range (FSR) as well as high tuning efficiency [42, 55, 107]. Furthermore, enhancing the tuning speed (i.e., reducing the thermal response time) beyond the constraint of the BOX layer remains a challenge. For further enhancement of the tuning speed a pre-emphasized voltage waveform was utilized for the heater operation [42, 110]. With the pre-emphasized voltage waveform sub-100-ns of 10 % – 90 % rise time (t_{rise}) was demonstrated. However, the 10 % – 90 % fall time (t_{fall}) did not decrease since the thermal time constant (τ) of the resonator system remained unchanged.

In this chapter, a novel approach for enhancing the tuning speed and range of SRRTFs is proposed. This approach utilizes metallic through-cladding-vias (TCVs) for thermal management of the SRRTF, as shown in Figure 4.1. The exterior TCV helps with better heat dissipation to the bulk silicon (i.e., the heat sink), so that it helps reduce

the τ and thus enhances the tuning speed. Furthermore, an interior-ridge ring is used for the resonator, and a metallic heater is formed on the TOX layer. Such a design enables the development of an ultra-compact resonator with a wide FSR. In addition, the interior TCV, along with the interior silicon slab of the resonator, helps increase the R owing to the high thermal conductivities of chromium (Cr) and silicon. Note that the thermal conductivities of Cr and silicon are ~100 times higher than that of oxide. Therefore, the tuning of SRRTF over a target spectral range can be realized at a much lower heater temperature compared with the conventional SRRTF, which relies on the TOX layer for the heat transfer from the heater to the waveguide.

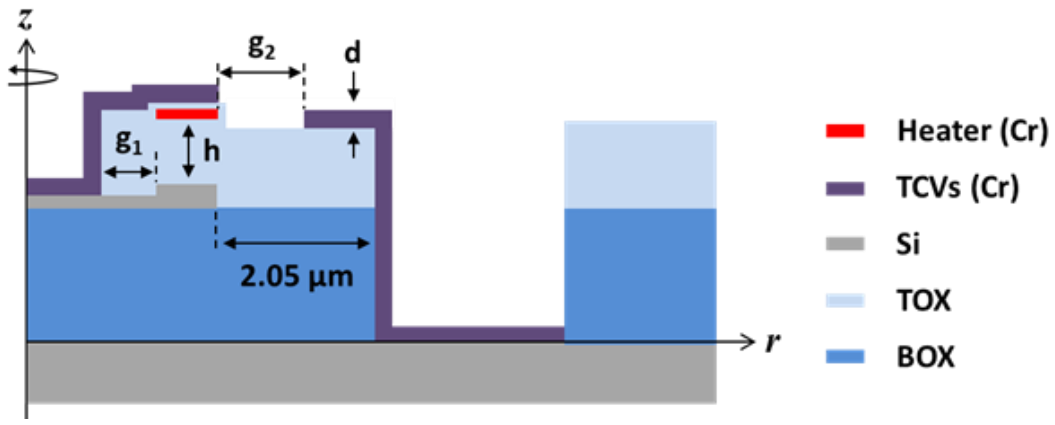

Figure 4.1 Schematic showing the cross section of the SRRTF with an interior-ridge ring and thermal TCVs.

The rest of this chapter is organized as follows. First, the SRRTF with an interior-ridge ring and thermal TCVs is designed. Next, the fabrication of the designed SRRTF is described. Then, the fabricated SRRTF is characterized. Further, simultaneous interrogation of multiplexed fiber-Bragg-grating (FBG) sensors is demonstrated with the fabricated SRRTF. Finally, concluding remarks are provided.

4.2 Design

4.2.1 Design of the interior-ridge-ring resonator

The interior-ridge-ring resonator was designed based on a disk resonator. Disk resonators, compared with ring resonators with the same outer radius, render a higher Q-factor, i.e., a narrower full-width at half-maximum (FWHM) spectrum. Such higher Q-factor of the disk resonator is attributed to less radiation and scattering losses. As the resonator radius decreases, the radiation loss (i.e., the waveguide bending loss) increases for both the disk and ring resonators. However, the ring resonator experiences more mode energy leakage into the radiation modes than the disk resonator since it has the inner sidewall of the waveguide, which forces the mode energy distribution out of the resonator [84]. Furthermore, exposure of the optical field to the inner sidewall increases the scattering loss due to the waveguide sidewall roughness. However, disk resonators have a drawback of supporting higher-order modes, which prevent to achieve a large FSR.

To address this drawback, the interior silicon of the disk resonator was partially removed [Figure 4.2 (a)], such that the inner sidewall of the waveguide could interact with and thus attenuate the higher-order modes only. The remaining 110 nm-thick silicon slab is used for the heat conduction path. The radius (r) and waveguide width (w) of the interior-ridge-ring resonator were determined based on the finite-element-method (FEM) simulation studies, as shown in Figures 4.2 (b) and 4.2 (c). The r was chosen to 2.1 μm, which renders ~2×10^6 of intrinsic Q-factor and ~57 nm of FSR for the 1st radial TE mode. The w was chosen to 600 nm, such that the intrinsic Q-factor of the 2nd radial TE mode decreases to be less than 2×10^2 while the intrinsic Q-factor of

the 1st radial TE mode remains to ~2 × 10^6. Note that the TE mode operation was selected for the resonator design since it renders higher thermal sensitivity and thus higher tuning efficiency than the TM mode operation. Further, the mode shapes of the designed interior-ridge-ring resonator were obtained using FEM simulations, as shown in Figure 4.2 (d). The mode shape of the 2nd radial TE mode was clearly different from that of the disk resonator. Meanwhile, the 1st radial TE mode of the interior-ridge-ring resonator had an almost similar mode shape with the disk resonator, which confirmed that the inner sidewall of the interior-ridge-ring resonator mainly interacts with and attenuates the 2nd radial TE mode.

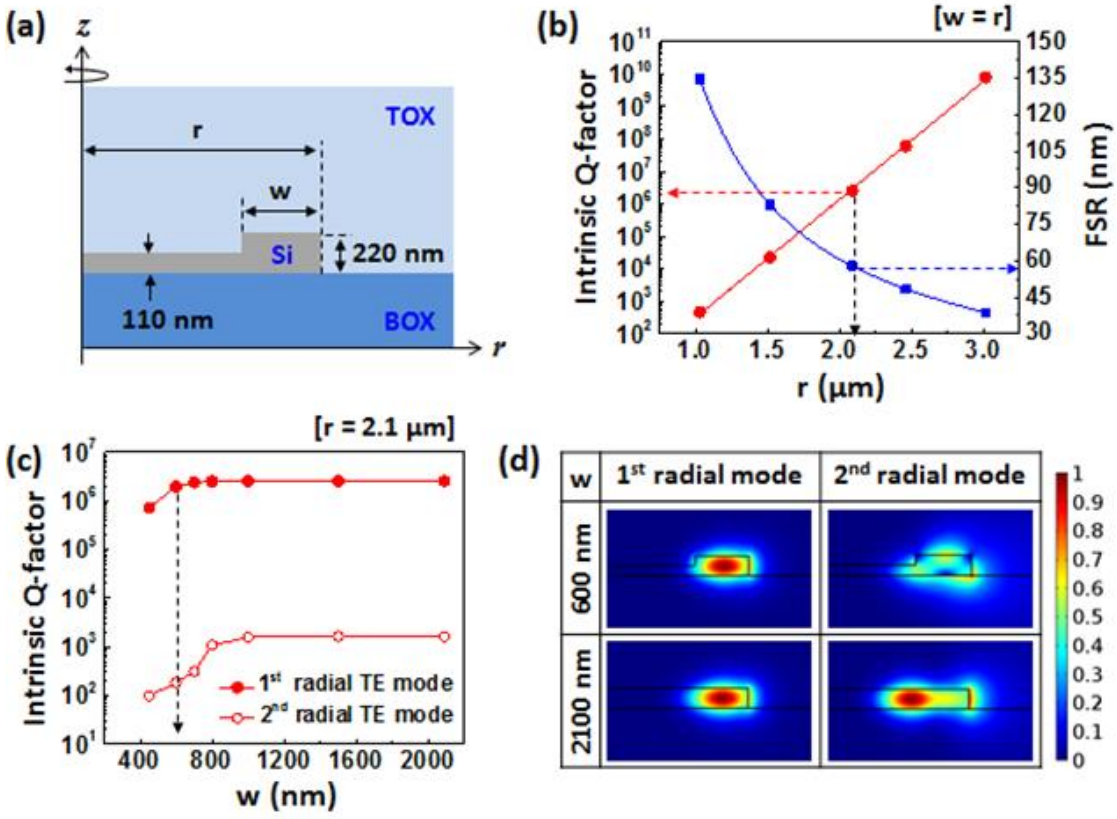

Figure 4.2 (a) Schematic showing the cross section of the interior-ridge-ring resonator. (b) Intrinsic Q-factor and FSR of a disk resonator as a function of the radius. The resonance wavelength of interest was located in 1550 nm ± 1 nm. (c) Intrinsic Q-factor of the interior-ridge-ring resonator as a function of the waveguide width. The outer radius of the resonator is 2.1 μm. (d) Normalized 1st and 2nd radial TE mode shapes of the interior-ridge-ring resonator at two different waveguide widths.

4.2.2 Design of the thermal TCVs

Four design parameters were defined for the thermal TCVs [Figure 4.1]: the gap between the interior TCV and the ring waveguide (g_1), the TOX layer thickness (h), the gap between the interior and the exterior TCVs (g_2), and the TCV thickness (d). The exterior TCV was located at 2.05 μm away from the ring resonator, which includes the 300 nm-wide bus waveguide, 250 nm of coupling gap, and 1,500 nm spacing from the bus waveguide. The BOX layer thickness was chosen to be 3 μm considering the

disposable silicon-on-insulator (SOI) wafer. Note that an SOI wafer with a thinner BOX layer can be used to achieve a faster thermal response time. For example, Atabaki et al. performed FEM simulation studies, which showed that the $t_{rise/fall}$ of the thermally tunable silicon ring resonator decreased from ~12 µs with a 3 µm BOX layer to ~4 µs with a 1 µm BOX layer [105]. However, thermally tunable silicon ring resonators with a thin BOX layer have a drawback of rendering low tuning power efficiency.

The small g_1 and h are desirable to increase the R. However, they should be large enough to avoid the absorption loss (i.e., Q-factor reduction) due to the metallic TCVs. To determine the g_1 and h, parametric studies were performed using FEM simulations, as shown in Figure 4.3. The simulation results show that the g_1 and h should be larger than ~400 nm and ~700 nm, respectively, to achieve the intrinsic Q-factor higher than ~1×10^6. Considering the fabrication error the g_1 and h were chosen to 600 nm and 900 nm, respectively.

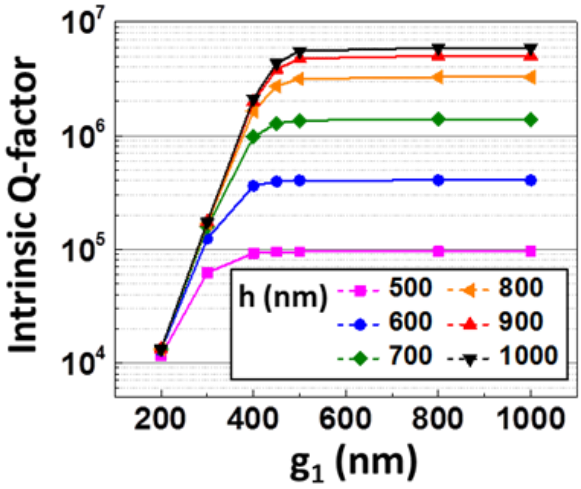

Figure 4.3 Intrinsic Q-factor of the interior-ridge-ring resonator as a function of the g_1 and h. 200 nm-thick Cr TCVs were used for the simulations.

For the chosen g_1 and h, the tuning characteristics of the SRRTF are determined by the g_2 and d. For high-speed, wide-range, power-efficient thermo-optic tuning of the SRRTF short $t_{rise/fall}$ and τ, high R, and high tuning efficiency (η) are desirable. To investigate the effects of the g_2 and d on these tuning characteristics, parametric studies were performed using FEM simulations, as shown in Figure 4.4. The simulation results show that for short $t_{rise/fall}$ and τ the g_2 should decrease and the d should be ~200 nm. For high R both the g_2 and d should increase. For high η the g_2 should increase while the d should decrease. Since there exist trade-offs between these tuning characteristics, a figure-of-merit (FOM) is defined for the thermal TCVs design as

$$FOM = \frac{t_{rise/\,fall}}{R \cdot \eta}, \tag{4.1}$$

where a small FOM is desirable. Based on the FOM analysis the g_2 and d were chosen to 1000 nm and 200 nm, respectively, which renders 4.20 μs·mW/nm of FOM [Figure 4.4 (e)].

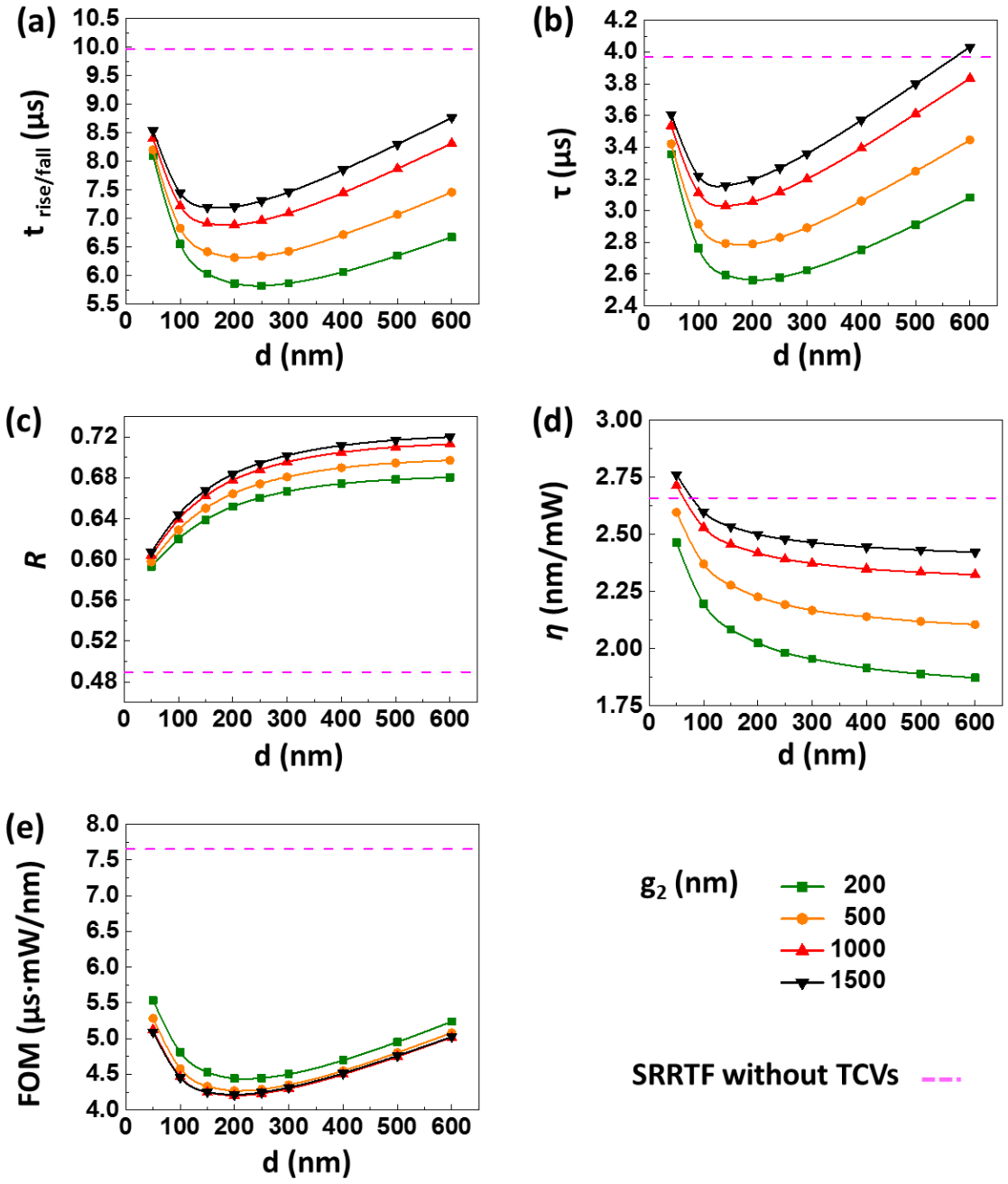

Figure 4.4 (a) $t_{rise/fall}$, (b) τ, (c), R, (d) η, and (e) FOM as a function of the g_2 and d. The g_1 and h are 600 nm and 900 nm, respectively.

Figure 4.5 shows the time-dependent thermal response and the steady-state temperature profile of the designed SRRTF. It renders 6.89 μs of $t_{rise/fall}$, 0.68 of R, and 2.42 nm/mW of η. Compared with the SRRTF without the thermal TCVs, the $t_{rise/fall}$ is

reduced by 30.9 %, the R increases by 38.8 %, the η is reduced by 9.0 %, and the FOM is enhanced by 45.1 %.

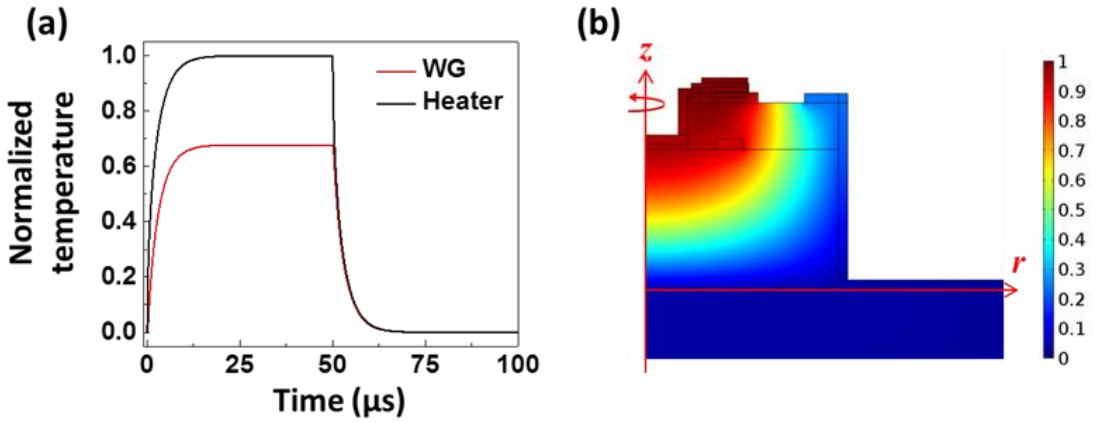

Figure 4.5 (a) Normalized response of the designed SRRTF to a square-wave thermal input and (b) its steady-state temperature profile (g_1: 600 nm, h: 900 nm, g_2: 1000 nm, d: 200 nm).

4.3 Fabrication

The designed SRRTF was fabricated with following fabrication steps.

Step 1: Interior-ridge-ring resonator fabrication. An SOI substrate with a 220 nm silicon layer and a 3μm BOX layer was prepared. The SOI substrate was spin-coated with a 60 nm-thick E-beam resist (ER) (PMMA A2). The waveguide was patterned using E-beam lithography, and a 20 nm-thick Cr film was deposited using E-beam evaporation. The Cr on top of the ER was lifted off [Figure 4.6 (a)]. A 110 nm-thick silicon was etched using inductively coupled reactive ion etching (ICP-RIE) [Figure 4.6 (b)]. A 200 nm-thick ER (PMMA A4) was spin-coated, and the interior slab was patterned using E-beam lithography. A 60 nm-thick Cr film was deposited using E-beam evaporation, and the Cr on top of the ER was lifted off [Figure 4.6 (c)]. The remaining 110 nm-thick silicon was etched using ICP-RIE. Finally, the Cr film was wet-etched [Figure 4.6 (d)].

Step 2: Heater fabrication. A 900 nm-thick TOX layer was deposited using plasma-enhanced chemical vapor deposition (PECVD) [Figure 4.6 (e)]. A 600 nm-thick ER (PMMA A6) was spin-coated, and the heater was patterned using E-beam lithography [Figure 4.6 (f)]. A 110 nm-thick Cr film was deposited using E-beam evaporation, and the Cr on top of the ER was lifted off [Figure 4.6 (g)]. Finally, A 100 nm-thick oxide insulation layer was deposited using PECVD [Figure 4.6 (h)].

Step 3: Thermal TCVs fabrication. A 500 nm-thick ER (MaN 2405) was spin-coated, and the TCV holes were patterned using E-beam lithography. A 20 nm/350 nm-thick Cr/Ni films were deposited using E-beam evaporation, and the Cr/Ni on top of the ER was lifted off [Figure 4.6 (i)]. The TOX and BOX layers were etched using ICP-RIE, and the Cr/Ni films were wet-etched [Figure 4.6 (j)]. Different depths of the interior and exterior TCV holes were fabricated with a single ICP-RIE process since different hole sizes render different etch rates. Note that the etch rate of a large hole is faster than that of a small hole. A 600 nm-thick ER (PMMA A6) was spin-coated, and the TCVs were patterned using E-beam lithography [Figure 4.6 (k)]. A 200 nm-thick Cr films were sputter-deposited. Sputtering was used for the Cr deposition since it gives better step coverage than E-beam evaporation. Finally, the Cr on top of the ER was lifted off [Figure 4.6 (l)].

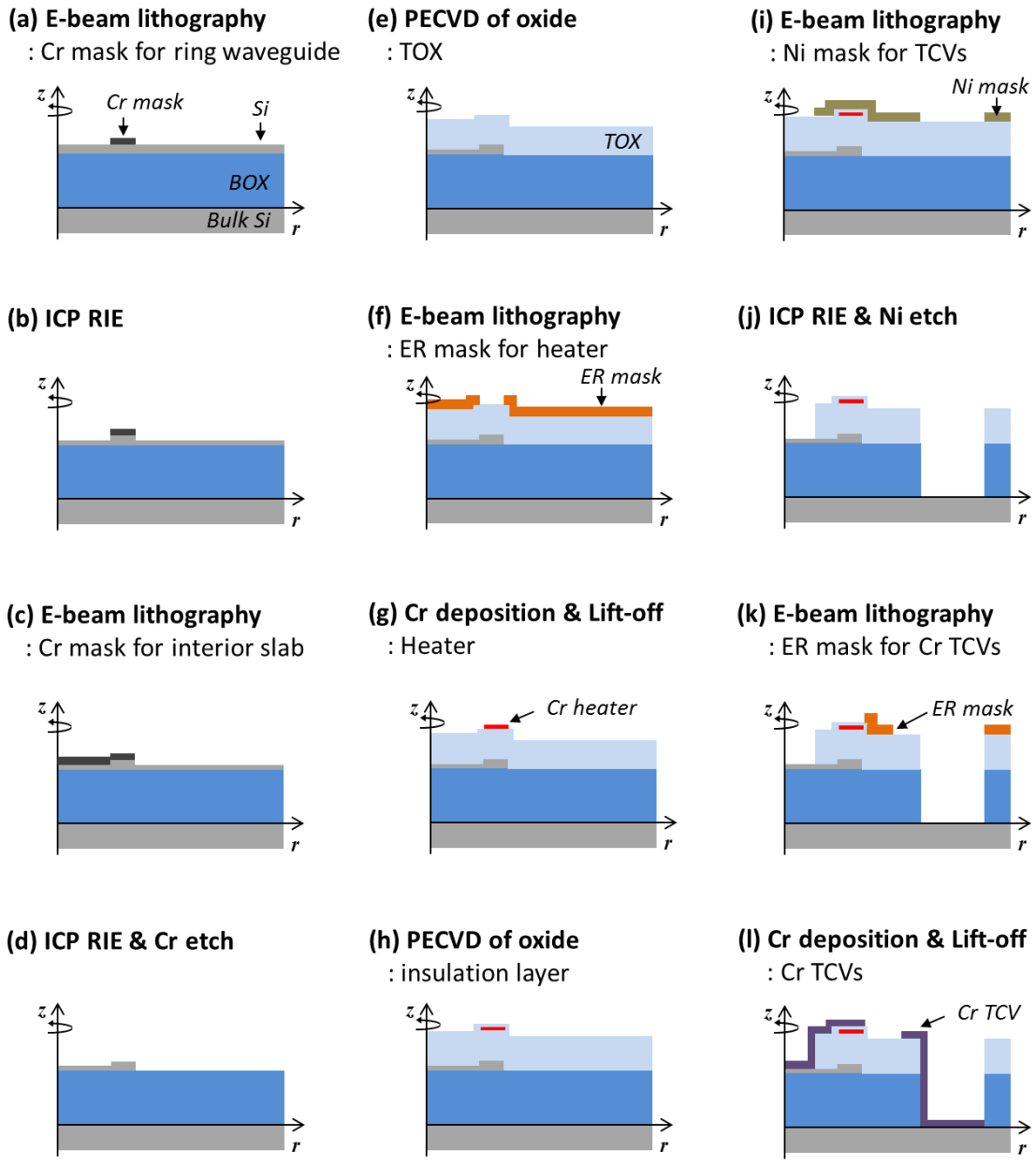

Figure 4.6 Fabrication process flow for the SRRTF. The fabrication process starts from (a) and ends with (l).

Figure 4.7(a) shows the fabricated Cr heater on the TOX layer. The heater width was measured to be 600 nm. Figures 4.7 (b) and 4.7 (c) show the fabricated SRRTF with the thermal TCVs. The black circle and rectangles are the interior and exterior TCV holes, respectively. Unlike the simulation studies, where the exterior TCV hole

surrounds the ring resonator, two exterior TCV holes were formed beside the ring resonator due to the electrical routing for the heater and the bus waveguides for coupling the light into and from the ring resonator. The TCV hole depths were measured using an optical topology measurement system (TMS-1200, Polytec), and the measured depths of the interior and exterior TCV holes were 1.66 μm and 4.01 μm, respectively.

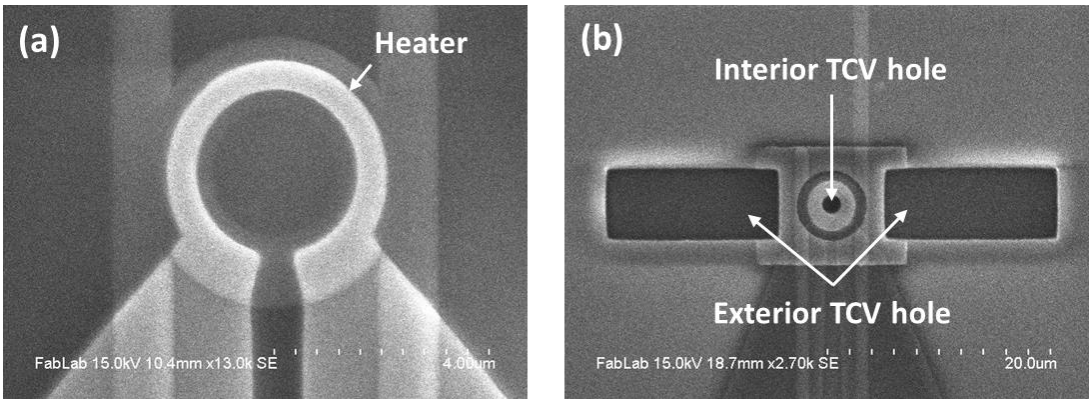

Figure 4.7 SEM images of (a) the Cr heater on the TOX layer of the SRRTF and (b) the SRRTF with the thermal TCVs.

4.4 Experimental setup

The fabricated SRRTF was characterized with a tunable laser (TL) [Figure 4.8 (a)]. The light from the TL was TE-polarized with a polarization controller, and was coupled into the SRRTF using an inverse taper coupler and lensed fiber. For the tuning speed measurement the wavelength of the TL (λ_{TL}) was set to be located at the half-maximum point of the resonance peak, and the SRRTF was operated with square-wave input voltage. The amplitude of the voltage waveform was set, such that the redshifted resonance wavelength (λ_{res}) was located at the λ_{TL} [Figure 4.8 (b)]. The output light from the SRRTF chip was monitored using a 10 MHz photodetector (PD) and an oscilloscope with 16-bit resolution and 1 GS/S speed.

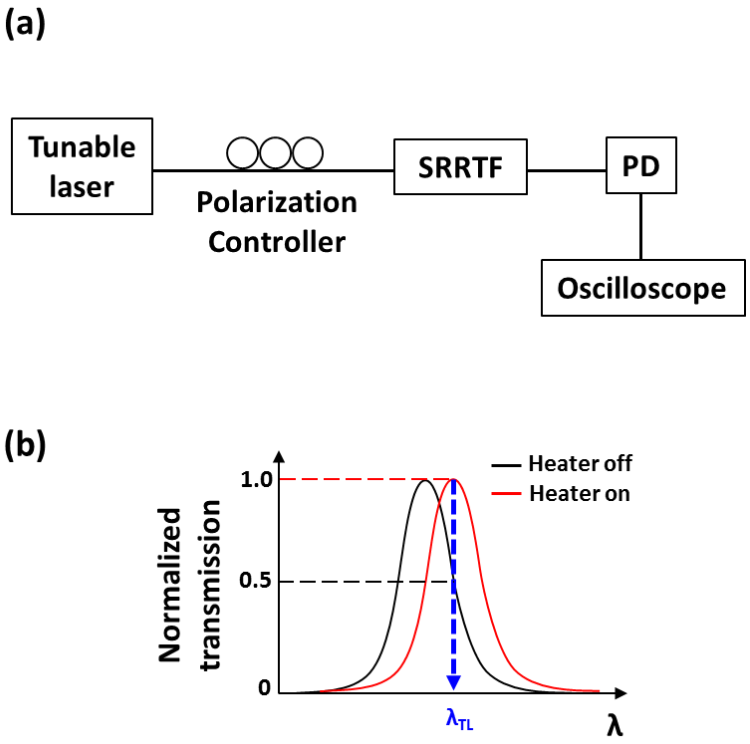

Figure 4.8 Schematics showing (a) the experimental setup for characterizing the SRRTF and (b) the λ_{TL} and the resonance shift during the tuning speed measurement.

With the fabricated SRRTF a SRRTF-based interrogator was developed for simultaneous interrogation of the multiplexed FBG sensors, as shown in Figure 4.9 (a). A broadband light source and a circulator were used to obtain the reflection signal of the three FBG sensors. The reflection signal was amplified using an erbium-doped fiber amplifier (EDFA). It was then TE-polarized and coupled into the fabricated SRRTF chip. The output light was monitored using a 10 MHz PD and an oscilloscope with 14-bit resolution and 62.5 MS/s speed. One of the FBG sensors (i.e., FBG 2) was attached on the aluminum clamped-free-free-free (CFFF) plate (60 mm × 50 mm × 3 mm) subjected to impact loading [Figure 4.9 (c)], and the others were isolated from environmental disturbances.

For the interrogation performance comparison an extrinsic Fabry-Perot (FP) fiber optic sensor was attached on the aluminum plate near the FBG 2, and an FP sensor interrogator was developed, as shown in Figure 4.9 (b). A broadband light source and a bandpass filter were used to provide a narrow-linewidth probe light with the FP sensor. The probe light was located at the quadrature point of the FP sensor spectrum. The reflection signal of the FP sensor was monitored with a 200 kHz PD and an oscilloscope with 14-bit resolution and 62.5 MS/s speed.

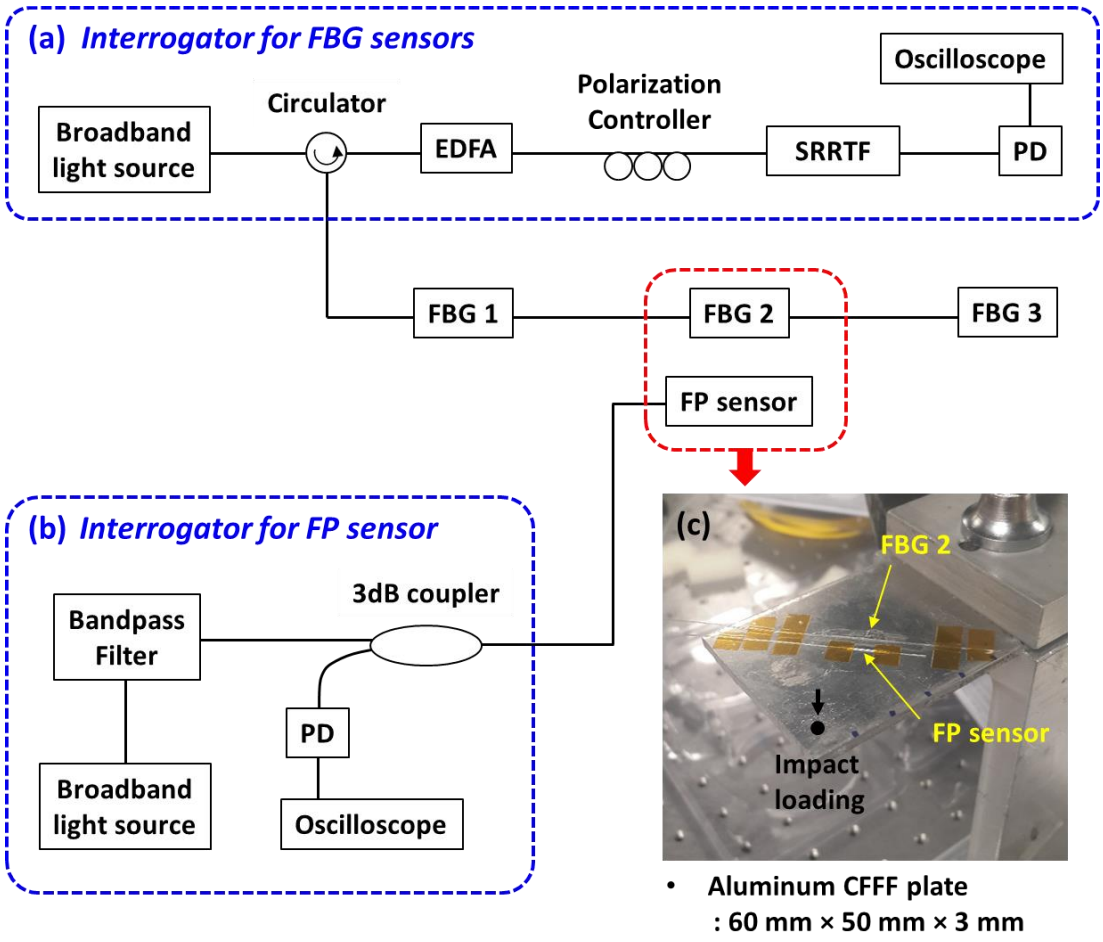

Figure 4.9 Schematics showing (a) the SRRTF-based interrogator for the multiplexed FBG sensors and (b) the interrogator for the FP sensor. (c) Photograph showing the FBG sensor and FP sensor attached on the aluminum CFFF plate.

4.5 Results and discussions

4.5.1 Characterization of the SRRTF

Figure 4.10 (a) shows the transmission spectrum of the fabricated SRRTF obtained at the drop port. At room temperature the λ_{res} of interest was 1540.09 nm and the FSR was 53.3 nm. The resonance at 1540.09 nm had a single peak with 0.276 nm of FWHM, as shown in Figure 4.10 (b). The Q-factor was ~5,600. The η of the SRRTF was measured to be 1.44 nm/mW, and a 39.2 nm of λ_{res} shift was achieved at 27.3 mW of heating power [Figure 4.10 (c)]. Figure 4.10 (d) shows the estimated temperature changes in the heater and the waveguide at given heating power, which were obtained from the measured λ_{res} shift, thermal sensitivity, and R of the SRRTF. From the FEM simulations the thermal sensitivity and R of the SRRTF were 78 pm/˚C and 0.68, respectively. At 27.3 mW of heating power the estimated temperature changes in the heater and the waveguide were 740 ˚C and 500 ˚C, respectively. To avoid a possible high-temperature failure of the heater the SRRTF was not operated at the heating power beyond 27.3 mW. For the tuning speed measurement the SRRTF was operated with 10 kHz of square-wave input voltage. The obtained time-dependent PD output is shown in Figure 4.10 (e). The measured $t_{rise/fall}$ was ~7.74 μs.

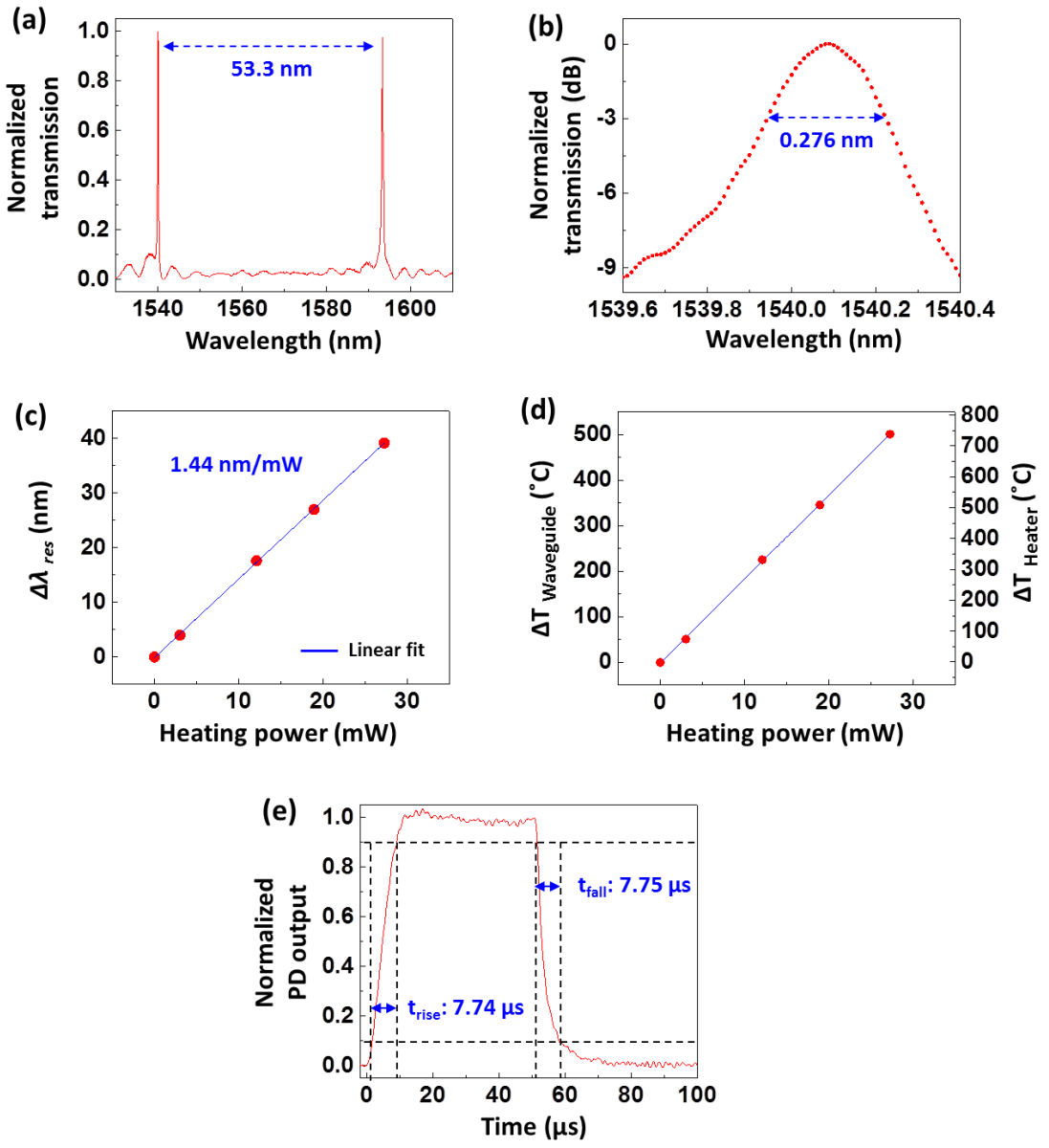

Figure 4.10 (a) Normalized transmission spectrum at the drop port of the SRRTF and (b) the zoom-in resonance peak. (c) Measured λ_{res} shift as a function of the heating power. (d) Estimated temperature changes in the waveguide and the heater as a function of the heating power. (e) Normalized PD output as a function of time. The SRRTF was operated with a 10 kHz of square-wave input voltage.

The measured $t_{rise/fall}$ and η showed errors from the simulation results (i.e., $t_{rise/fall}$: 6.89 µs, η: 2.42 nm/mW). These errors are believed to result from the differences in the geometric parameters and material properties between the experiments and

simulations. There were three main discrepancies in the geometric parameters. First, the exterior TCV hole of the fabricated SRRTF did not surround the resonator. Further, the Cr thickness in the TCV sidewall is believed to be less than 200 nm. In general, the deposition rate in the sidewall is lower than that in the plate surface. Lastly, the depth of the interior TCV hole was ~700 nm deeper than that in the simulations. For accurate depth control the TCV hole etching process should be separated into two ICP-RIE processes: one for the interior TCV hole and the other for the exterior TCV hole. However, it has a drawback of requiring an additional E-beam lithography process.

4.5.2 Simultaneous interrogation of the multiplexed FBG sensors

For simultaneous interrogation of the multiplexed FBG sensors the SRRTF was operated with square-wave input voltage. The operating frequency was chosen to 62.5 kHz considering the ~7.74 μs of $t_{rise/fall}$, which rendered 125 kHz of interrogation speed. Note that the interrogation speed is twice of the operation frequency since the SRRTF scans the spectral range twice in one thermal response cycle. The amplitude of the voltage waveform was set, such that the Bragg wavelengths (λ_{Bragg}s) of the multiplexed FBG sensors were kept within the interrogation range. Figure 4.11 (a) shows the λ_{Bragg}s of the three FBG sensors monitored with the SRRTF-based interrogator in Figure 4.9 (a). The λ_{Bragg} of the FBG 2 started fluctuating when impact loading was applied to the aluminum plate (i.e. at ~1.2 ms). However, the λ_{Bragg}s of the FBG 1 and FBG 3 remained unchanged since they were isolated from environmental disturbances. Figure 4.11 (b) shows the λ_{Bragg} fluctuation of the FBG 2 in the first 5 ms, which had the same trend with the fluctuation of the reflection power of the FP sensor [Figure 4.11 (c)]. However, the signal-to-noise ratio of the FBG 2 was lower than that of the FP sensor,

which is believed to be attributed to the lower strain sensitivity of the FBG sensor compared with the FP sensor.

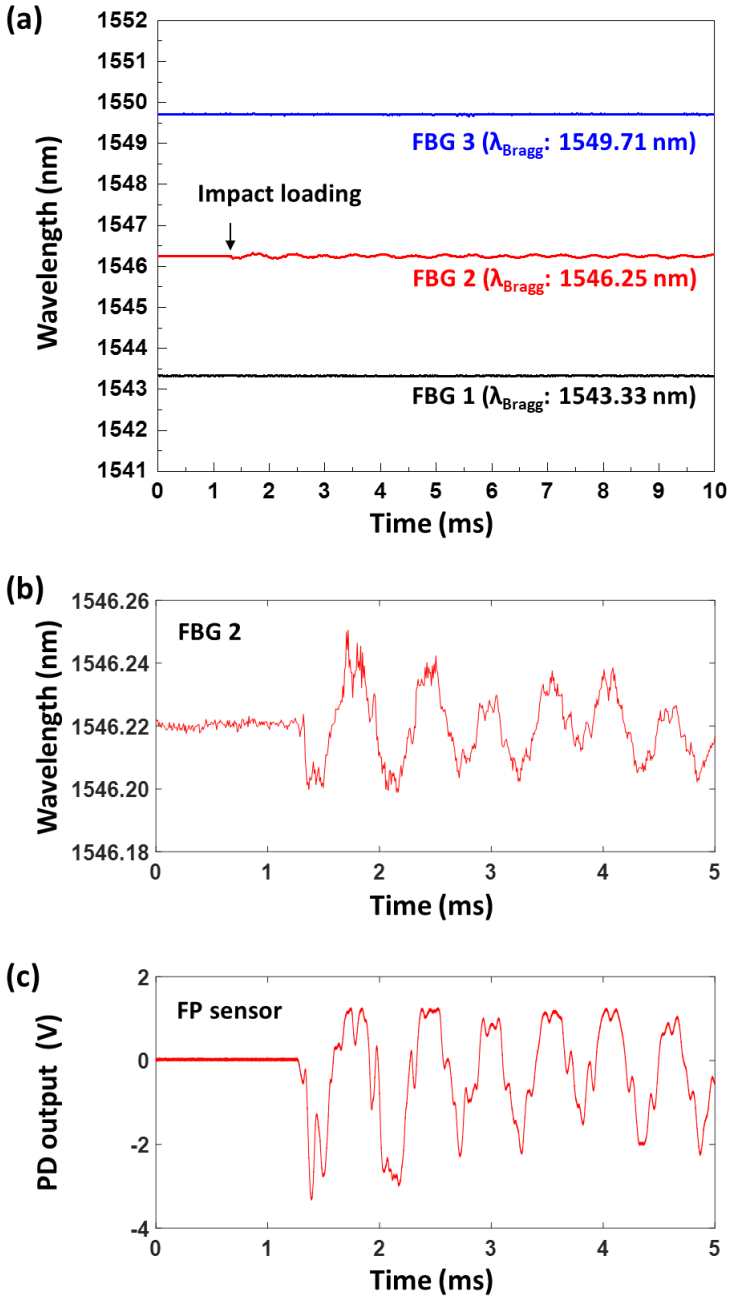

Figure 4.11 (a) λ_{Bragg}s of the three FBG sensors as a function of time. Impact loading was applied to the aluminum plate at ~1.2 ms. (b) λ_{Bragg} fluctuation of the FBG 2 and (c) fluctuation of the reflection power from the FP sensor in the first 5 ms.

The time-domain responses of the FBG 2 and the FP sensor were transformed into frequency domain to find the resonance frequencies of the aluminum plate, as shown in Figure 4.12 (a) and 4.12 (b). 4 resonance frequencies were observed from the spectrum of the FBG 2: 0.65 kHz, 1.84 kHz, 7.44 kHz, and 12.63 kHz. 6 resonance frequencies were observed from the spectrum of the FP sensor: 0.65 kHz, 1.84 kHz, 3.72 kHz, 7.44 kHz, 12.63 kHz, and 18.56 kHz. Note that the 3.72 kHz and 18.56 kHz of resonance frequencies were not observed in the spectrum of the FBG 2, which is believed due to the low signal-to-noise ratio of the FBG sensor response. For comparison, frequency response of the aluminum plate was analyzed using FEM simulations. Figure 4.12 (c) shows the simulated, frequency-dependent strain changes at the center point of the aluminum plate surface, where the FBG 2 and FP sensor is located. The resonance frequencies measured from the experiment results compared well with the simulation result. However, the experimental results did not show all the resonance frequencies in the simulation result. It is believed due to the following reasons. First, the adhesives for attaching the FBG and FP sensors on the aluminum plate (i.e., acrylic glue for the FBG sensor and Kapton tape for the FP sensor) act as a damper, such that it prevents the sensors from responding to the plate deformation at high frequency. Second, these optical fiber sensors are sensitive to strains along the fiber axis but not for strains in other directions. Therefore, they cannot measure all the strain changes at the center point of the aluminum plate surface.

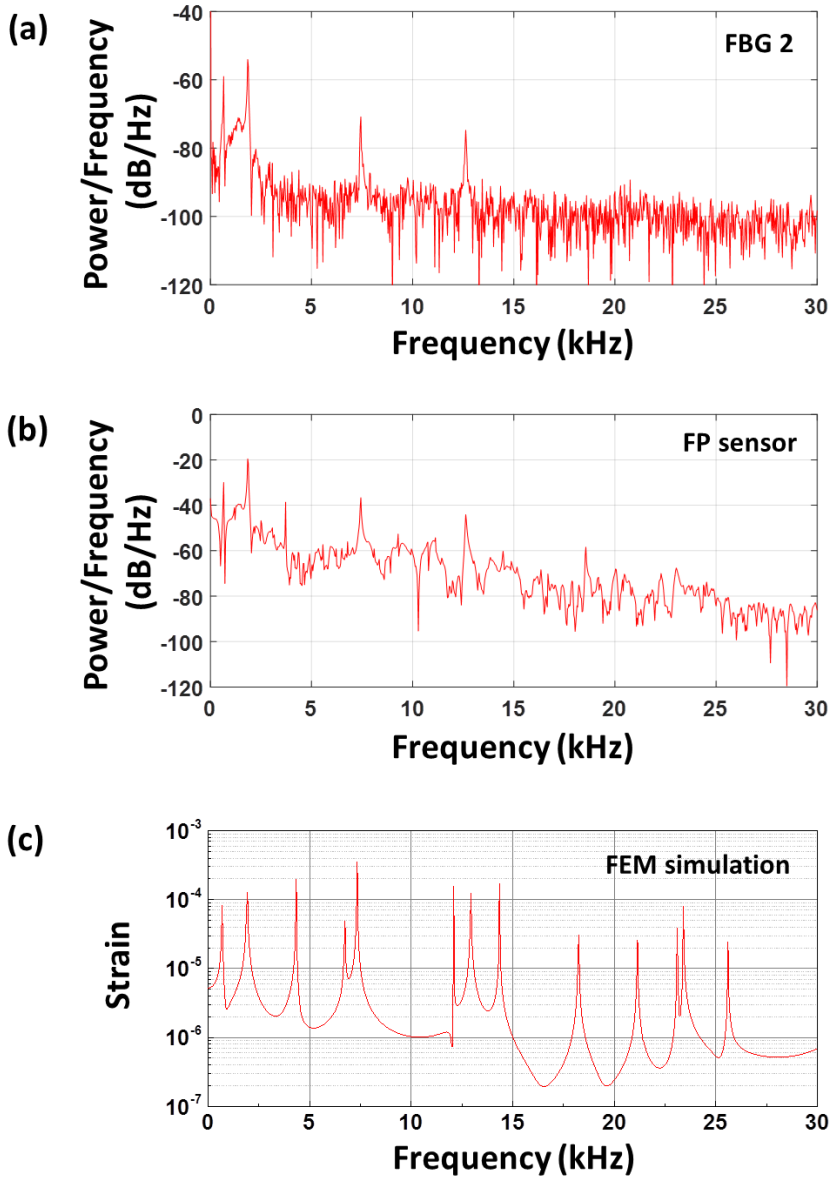

Figure 4.12 Frequency spectra of the time-domain responses of (a) the FBG 2 and (b) the FP sensor. (c) Simulated frequency response of the aluminum plate. The strain was monitored at the center of the aluminum plate surface.

4.6 Summary

In summary, a high-speed and wide-range SRRTF was developed for simultaneous interrogation of multiplex FBG sensors. The developed SRRTF used an interior-ridge-ring resonator and thermal TCVs to enhance the tuning speed and range.

It demonstrated 62.5 kHz of tuning speed (7.74 μs of $t_{rise/fall}$) and 40 nm of tuning range with a 53.3 nm of FSR. With the developed SRRTF three FBG sensors were simultaneously interrogated at 125 kHz of speed. One of the FBG sensors was used to monitor the response of the aluminum plate under impact loading, and it successfully monitored the resonance frequencies of the aluminum plate up to 12.63 kHz. This work will help develop a high-speed on-chip optical interrogator for simultaneous interrogation of large array of FBG sensors.

Chapter 5: Summary and future work

5.1 Summary of the dissertation work

Recent progress in integrated photonics technology has shed light on the performance enhancement, miniaturization, and cost reduction of optical sensing systems. Among many integrated photonic structures, silicon microring resonators have received much attention for both sensing and interrogation. Particularly, the high quality-factor (Q-factor) of the ring resonator and the large thermo-optic coefficient and high thermal conductivity of silicon make them attractive for temperature sensing and thermally-tunable-filter-based interrogation.

This dissertation work is aimed at achieving enhanced understanding of thermo-optic effects in silicon microring resonators and applying such understanding to the development of (1) a cascaded-ring-resonator (CRR)-based temperature sensor, (2) a high-speed interrogator with a silicon-ring-resonator-based thermally tunable filter (SRRTF), and (3) a high-speed and wide-range SRRTF for simultaneous interrogation of multiplexed FBG sensors. The dissertation work is summarized as follows.

Sensitivity of conventional silicon-ring-resonator-based temperature sensors has been less than ~80 pm/°C. Since the sensor resolution is determined by the sensitivity and the interrogator resolution, they have often required a bulky and expensive fine-resolution interrogator for precise temperature monitoring. In the first part of the dissertation work, the CRR-based Vernier effect was investigated to enhance

the sensitivity as well as the sensing range of the silicon-ring-resonator-based temperature sensor. To achieve the dual enhancement the CRR-based temperature sensor employed two silicon ring resonators with different temperature sensitivities and different free-spectral-ranges (FSRs). The differences in the temperature sensitivities and FSRs were obtained by tailoring the in-plane geometric parameters of the CRRs. For proof-of-concept the CRR-based temperature sensor was fabricated using a single-mask complementary metal-oxide-semiconductor (CMOS)-compatible process. With the fabricated CRR sensor, a temperature sensitivity of 293.9 pm/°C was demonstrated, which was 6.3 times higher than that of the individual ring resonator. Furthermore, the sensor was shown to enhance the temperature sensing range by 5.3 times. Owing to the sensitivity enhancement of the CRR-based temperature sensor, one can potentially use an on-chip, low resolution spectrometry for sensor interrogation without significant compromise in resolution. This can help reduce the volume and cost of photonic temperature monitoring systems.

On-chip optical interrogators employing an SRRTF offer a promising solution for realizing portable, compact optical sensing systems. However, the slow interrogation speed of conventional SRRTF-based interrogators (less than a few Hz) has hindered real-time sensing of dynamic parameters. In the second part of the dissertation work, a 100 kHz of high-speed SRRTF-based interrogator was developed for monitoring dynamic parameters. The speed enhancement was achieved by using the nonlinear transient response of the SRRTF to a square-wave input voltage. The entire spectral range of the SRRTF was scanned twice during its thermal response cycle. The time-domain sensor output signal, which was obtained by scanning the SRRTF

over the sensor spectrum, was converted into spectrum domain based on the experimentally characterized, time-dependent resonance wavelength shifts of the SRRTF. With the developed high-speed SRRTF-based interrogator, a fiber Bragg grating (FBG) sensor under dynamic temperature change (200 Hz) was interrogated. This work will pave the way for realizing portable, compact optical sensing systems for real-time monitoring of dynamic parameters.

Performance of SRRTF-based interrogators is primarily determined by thermal and optical characteristics of the SRRTF, including the tuning speed and range. However, conventional SRRTFs (i.e., a silicon ring resonator with a micro-heater on the top oxide cladding) are not suitable for high-speed and wide-range tuning. In the third part of the dissertation work, a high-speed and wide-range SRRTF was developed for simultaneous interrogation of multiplexed FBG sensors. The developed SRRTF employed an interior-ridge ring and thermal through-cladding-vias (TCVs). The thermal TCVs reduced the thermal response time of the SRRTF and thus enhanced the tuning speed. Further, the thermal TCVs, along with the interior-ridge ring, increased the ratio of the waveguide temperature change to the heater temperature change, which helps increase the tuning range avoiding high-temperature failure of the heater. The interior-ridge ring enabled the resonator to achieve a large FSR with high Q-factor. The developed SRRTF demonstrated 62.5 kHz of tuning speed (i.e., ~7.74 μs of $t_{rise/fall}$) and a 40 nm of tuning range with a 53.3 nm of FSR. With the developed SRRTF three FBG sensors were simultaneously interrogated at 125 kHz of speed. One of the FBG sensors was used to monitor the response of the aluminum plate subjected impact loading and observed the resonance frequencies of the aluminum plate up to 12.63 kHz. This work

will help develop a high-speed on-chip optical interrogator for simultaneously interrogating large array of FBG sensors.

The original contributions in this dissertation work are summarized as follows:

Contribution 1: A novel concept of silicon photonic temperature sensing has been developed with the CRR-based Vernier effect for simultaneous enhancement of the sensitivity and sensing range. The figure-of-merit (FOM) of the temperature sensor is defined by the FSRs of the CRRs. The FOM can be used to either solely enhance the sensitivity or sensing range or enhance both by tailoring the in-plane geometric parameters of the CRRs. A proof-of-concept temperature sensor was fabricated, and demonstrated 6.3 times enhancement in the sensitivity and 5.3 times enhancement in the sensing range with a 33.4 of FOM.

Contribution 2: A novel, high-speed optical interrogation scheme using the nonlinear transient response of an SRRTF has been developed for interrogation of optical sensors for dynamic parameter sensing. The nonlinear transient response of the SRRTF has been investigated for scanning the sensor spectrum twice in its thermal response cycle. With the developed high-speed interrogator an FBG sensor was interrogated at 100 kHz of speed.

Contribution 3: An SRRTF employing an interior-ridge-ring resonator and TCVs has been developed to enhance the speed and range of the SRRTF-based interrogator. The developed SRRTF demonstrated 62.5 kHz of tuning speed and 40 nm of tuning range with a 53.3 nm of FSR. The speed and range of the interrogator with the developed SRRTF are 125 kHz and 40 nm, respectively.

5.2 Future work

As an extension of this dissertation work, future work is suggested as follows.

1) SRRTF with a doped poly-silicon heater for high temperature operation. For the developed SRRTF-based interrogator the major failure mechanism was damage of the chromium heater at high heating power. The heater exposed to high heating power (i.e., high operating temperature) experienced the degradation of electrical and mechanical characteristics. For example, the electrical resistance of the heater changed permanently, and in the worst case the heater was burned out and had a short circuit. To address such issues, a doped polysilicon heater will be used for the SRRTF. Doped polysilicon has been widely used as a heater material for high-temperature micro-electro-mechanical-system (MEMS) hotplates and thermal infrared emitters. For such devices the doped polysilicon heater has demonstrated long-term stable operation at high temperature (~1000 K) [104]. Therefore, the SRRTF with a doped polysilicon heater will help develop a high-speed and wide-range SRRTF-based interrogator with enhanced long-term reliability.

2) Integration of the SRRTF-based interrogator into a miniaturized platform. The developed SRRTF had a 2.1 μm-radius, ultracompact ring resonator and the device footprint including the bus waveguides and the electrical contact pads was less than 500 μm × 200 μm. However, the SRRTF-based interrogator had large photonic components such as a broadband light source, optical amplifier, pulse generator, and photodetector, which made the interrogator bulky. Further, coupling the light into and from the SRRTF chip relied on the lensed fibers with a precise fiber alignment system on the anti-vibration table. To reduce the volume and enhance the

portability of the SRRTF-based interrogator, the entire interrogator will be integrated into a miniaturized platform. The platform will consist of a photonic circuit and a supporting electrical circuit. The photonic circuit will be realized by bonding the SRRTF, superluminescent diode, semiconductor optical amplifier chip, and photodiode onto a silicon submount. Optical interconnection between the photonic components will be achieved using 3D-printed polymer waveguides. These photonic components will be then electrically connected to the supporting electrical circuit using wire bonding. Further, the operation temperature of the photonic circuit will be kept at ~20 °C using a thermoelectric cooler and a heat sink. Such a miniaturized SRRTF-based interrogator will extend the application of optical sensing in emerging fields such as wireless sensor network and wearable biomedical devices.

Appendix A: LabView code for data acquisition

A.1 Data acquisition with Picoscope 5444B

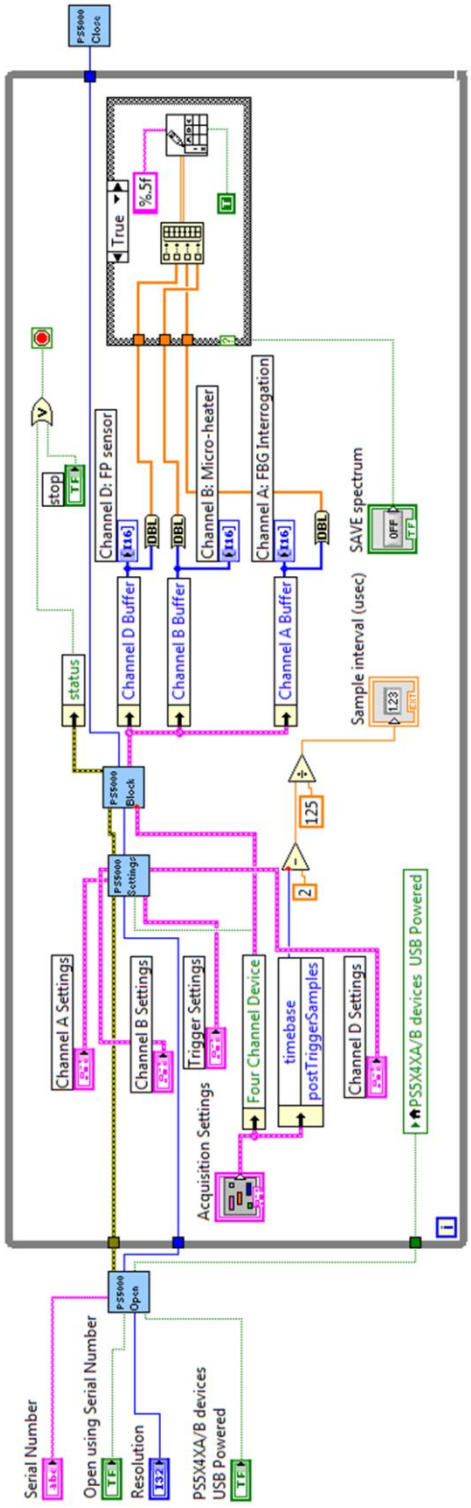

Appendix B: Matlab codes for the sensor interrogation

B.1 Data processing for the FBG sensor interrogation

```
%% Data loading
m = importdata('Aluminum_plate_Impact');
S   = 679;
SP  = 1000;
E   = 4000;
t   = m(S:S+SP*E,1);
FBG = m(S:S+SP*E,3);
FG  = m(S:S+SP*E,4);


%% Sampling parameters
time_lapse = mean(diff(t));
Fs = 1/(time_lapse*10^-6);
time_cycle = 16;
Fs_int = 1/(time_cycle*10^-6);


%% Full-spectrum visualization
Target = FBG;
i = floor(length(Target)/SP);
t_scan   = transpose(0:time_cycle/(SP-1):time_cycle);
t_intero = 0:time_cycle/1000:time_cycle/1000*(i-1);
Spectra_2D = reshape(Target(1:SP*i),[SP,i]);
figure()
[C,h] = contourf(t_intero,t_scan,Spectra_2D);
set(h,'LineColor','none')
xlabel('Interrogation time (msec)')
ylabel('Time spectrum (usec)')


%% Bragg wavelength tracing
mar1 = 100;
mar2 = 330;
mar3 = 200;
mar4 = 230;
t_fit = 0:0.001:time_cycle;
lf    = length(t_fit);

t_scan_on  = t_scan(mar1:ceil(SP/2)-mar2);
t_scan_off = t_scan(ceil(SP/2)+mar3:end-mar4);
t_fit_on   = t_fit(1:ceil(lf/2));
t_fit_off  = t_fit(ceil(lf/2):end);

for j = 1:i
    y = Spectra_2D(:,j);

    y_on = y(mar1:(SP/2)-mar2);
    xx = min(length(t_scan_on),length(y_on));
    f_on = fit(t_scan_on(1:xx),y_on(1:xx),'gauss1');
    [Pks_on,loc_on] = findpeaks(f_on(t_fit_on));
```

```
    [PksM_on, idx_on] = max(Pks_on);
    Peak_on(j) = t_fit_on(loc_on(idx_on

    y_off = y((SP/2)+mar3:end-mar4);
    xy = min(length(t_scan_off),length(y_off));
    f_off = fit(t_scan_off(1:xy),y_off(1:xy),'gauss1');
    [Pks_off,loc_off] = findpeaks(f_off(t_fit_off));
    [PksM_off, idx_off] = max(Pks_off);
    Peak_off(j) = t_fit_off(loc_off(idx_off));
end


%% Offset calibration
p1 =    0.001845;
p2 =        2.05;
F1_Cal = p1 * t_intero + p2 - 2.05;
Scan_on_Pks = transpose(Peak_on-F1_Cal);

p10 =    0.001674;
p20 =        11.8;
F2_Cal = p10 * t_intero + p20 - 11.8;
Scan_off_Pks = transpose(Peak_off-F2_Cal);


%% Wavelength demodulation
w_e = 1554.86;
w_s = 1541.0;

a =      0.1383;
b =     -0.4964;
c =      0.5207;
d =     -0.1674;
e =      0.4592;
f =     -0.3225;
x =  Scan_on_Pks;
Bragg_on = w_e-(w_e-w_s)*(a*exp(b*x)+c*exp(d*x)+e*exp(f*x));

a1 =      0.3399;
b1 =     -0.2761;
c1 =     0.04151;
d1 =    -0.03151;
e1 =      0.6058;
f1 =     -0.2761;
y =  Scan_off_Pks;
Bragg_off = w_s+(w_e-w_s)*(a1*exp(b1*y)+c1*exp(d1*y)+e1*exp(f1*y));


%% Time-domain response
Bragg = zeros(1,length(Bragg_on)*2);
Bragg(1:2:end-1) = Bragg_on;
Bragg(2:2:end)   = Bragg_off;
Bragg = transpose(Bragg);

Fs_comb = 1/(time_cycle*10^-6)*2;
t_comb = 0:time_lapse/2:time_lapse*E;
```

```
figure()
plot(t_comb(1:length(Bragg)) , Bragg, 'r');
tix=get(gca,'ytick')';
set(gca,'yticklabel',num2str(tix,'%.2f'))


%% Power spectrum
M = length(Bragg);
xdft = fft(Bragg);
xdft = xdft(1:M/2+1);
psdx = (1/(Fs_comb*M)) * abs(xdft).^2;
psdx(2:end-1) = 2*psdx(2:end-1);
freq = 0:Fs_comb/length(Bragg):Fs_comb/2;

figure()
plot(freq/1000,10*log10(psdx),'r')
grid on
xlabel('Frequency (kHz)')
ylabel('Power/Frequency (dB/Hz)')
```

B.2 Data processing for the FP sensor interrogation

```
%% Data loading
m = importdata(' Aluminum_plate_Impact');
S  = 679;
SP = 1000;
E  = 4000;
t  = m(S:S+SP*E,1);
FP = m(S:S+SP*E,2);


%% Sampling parameters
time_lapse = mean(diff(t));
Fs = 1/(time_lapse*10^-6);
time_cycle = 16;
Fs_int = 1/(time_cycle*10^-6);


%% Time-domain response
figure()
plot((t-min(t))/1000,FP,'r')
xlabel('Time (msec)')
ylabel('Amplitude')


%% Power spectrum
N = length(FP);
xdft = fft(FP);
xdft = xdft(1:N/2+1);
psdx = (1/(Fs*N)) * abs(xdft).^2;
psdx(2:end-1) = 2*psdx(2:end-1);
freq = 0:Fs/length(FP):Fs/2;
```

```
figure()
plot(freq/1000,10*log10(psdx))
xlim([0 20])
grid on
xlabel('Frequency (kHz)')
ylabel('Power/Frequency (dB/Hz)')
```

Appendix C: Material properties for optical and thermal simulations

	Silicon	**Silicon dioxide**	**Chromium**
Refractive index	3.48	1.45	3.66 + i4.18
Thermo-optic coefficient (/K)	1.86×10^{-4}	1.0×10^{-5}	-
Heat capacity (J/kg/K)	703	733	448
Density (kg/m^3)	2330	2203	7150
Thermal conductivity (W/m/K)	163	1.3	93.7

Appendix D: List of Publications

Journal Publications

[1] **H.-T. Kim** and M. Yu, "High-speed optical sensor interrogator with a silicon-ring-resonator-based thermally tunable filter," Optics Letters, vol. 42, pp. 1305-1308, 2017.

[2] **H.-T. Kim** and M. Yu, "Cascaded ring resonator-based temperature sensor with simultaneously enhanced sensitivity and range," Optics Express, vol. 24, pp. 9501-9510, 2016.

[3] **H.-T. Kim**, H. Bae, Z. Zhang, A. Kusimo, and M. Yu, "Optofluidic microvalve-on-a-chip with a surface plasmon-enhanced fiber optic microheater," Biomicrofluidics, vol. 8, p. 054126, 2014.

[4] **H.-T. Kim** and M. Yu, "High-speed and wide-range thermally tunable silicon ring resonator for simultaneous interrogation of FBG sensors," (To be submitted).

Conference Proceedings

[1] **H.-T. Kim** and M. Yu, "Thermally-tunable ring resonators for high-speed optical sensor interrogation," in CLEO: Science and Innovations, 2016, p. SM3G. 2.

[2] **H.-T. Kim** and M. Yu, "Thermally-tunable-silicon-ring-resonator-based high-speed optical sensor interrogator for impact monitoring," accepted to Frontiers in Optics, 2017.

Bibliography

[1] A. Densmore, D.-X. Xu, P. Waldron, S. Janz, P. Cheben, J. Lapointe, *et al.*, "A silicon-on-insulator photonic wire based evanescent field sensor," *Photonics Technology Letters, IEEE*, vol. 18, pp. 2520-2522, 2006.

[2] X. Fan, I. M. White, H. Zhu, J. D. Suter, and H. Oveys, "Overview of novel integrated optical ring resonator bio/chemical sensors," in *Lasers and Applications in Science and Engineering*, 2007, pp. 64520M-64520M-20.

[3] P. Prabhathan, V. Murukeshan, Z. Jing, and P. V. Ramana, "Compact SOI nanowire refractive index sensor using phase shifted Bragg grating," *Optics express*, vol. 17, pp. 15330-15341, 2009.

[4] E. Chow, A. Grot, L. Mirkarimi, M. Sigalas, and G. Girolami, "Ultracompact biochemical sensor built with two-dimensional photonic crystal microcavity," *Optics letters*, vol. 29, pp. 1093-1095, 2004.

[5] A. L. Washburn, M. S. Luchansky, A. L. Bowman, and R. C. Bailey, "Quantitative, label-free detection of five protein biomarkers using multiplexed arrays of silicon photonic microring resonators," *Analytical chemistry*, vol. 82, pp. 69-72, 2009.

[6] M. S. Luchansky and R. C. Bailey, "Rapid, multiparameter profiling of cellular secretion using silicon photonic microring resonator arrays," *Journal of the American Chemical Society*, vol. 133, pp. 20500-20506, 2011.

[7] G. T. Reed and A. P. Knights, *Silicon photonics: The state of the art*: Wiley Online Library, 2008.

[8] G. Strouse, "Standard platinum resistance thermometer calibrations from the Ar TP to the Ag FP," *NIST Special Publication*, vol. 250, p. 81, 2008.

[9] H. Xu, M. Hafezi, J. Fan, J. Taylor, G. Strouse, and Z. Ahmed, "Ultra-sensitive chip-based photonic temperature sensor using ring resonator structures," *Optics express*, vol. 22, pp. 3098-3104, 2014.

[10] N. N. Klimov, S. Mittal, M. Berger, and Z. Ahmed, "On-chip silicon waveguide Bragg grating photonic temperature sensor," *Optics letters*, vol. 40, pp. 3934-3936, 2015.

[11] F. Taffoni, D. Formica, P. Saccomandi, G. D. Pino, and E. Schena, "Optical fiber-based MR-compatible sensors for medical applications: An overview," *Sensors*, vol. 13, pp. 14105-14120, 2013.

[12] S. J. Mihailov, "Fiber Bragg grating sensors for harsh environments," *Sensors*, vol. 12, pp. 1898-1918, 2012.

[13] A. D. Kersey, M. A. Davis, H. J. Patrick, M. LeBlanc, K. Koo, C. Askins, *et al.*, "Fiber grating sensors," *Journal of lightwave technology*, vol. 15, pp. 1442-1463, 1997.

[14] D. Kinet, P. Mégret, K. W. Goossen, L. Qiu, D. Heider, and C. Caucheteur, "Fiber Bragg grating sensors toward structural health monitoring in composite materials: Challenges and solutions," *Sensors*, vol. 14, pp. 7394-7419, 2014.

[15] N. A. Mohammed, T. A. Ali, M. H. Aly, and O. Member, "Evaluation and performance enhancement for accurate FBG temperature sensor measurement with different apodization profiles in single and quasi-distributed DWDM systems," *Optics and Lasers in Engineering*, vol. 55, pp. 22-34, 2014.

[16] G. Coppola, L. Sirleto, I. Rendina, and M. Iodice, "Advance in thermo-optical switches: principles, materials, design, and device structure," *Optical Engineering*, vol. 50, pp. 071112-071112-14, 2011.

[17] H. Bae, D. Yun, H. Liu, D. A. Olson, and M. Yu, "Hybrid miniature Fabry–Perot sensor with dual optical cavities for simultaneous pressure and temperature measurements," *Journal of Lightwave Technology*, vol. 32, pp. 1585-1593, 2014.

[18] D. J. Sadler, R. Changrani, P. Roberts, C.-F. Chou, and F. Zenhausern, "Thermal management of BioMEMS: temperature control for ceramic-based PCR and DNA detection devices," *Components and Packaging Technologies, IEEE Transactions on*, vol. 26, pp. 309-316, 2003.

[19] G. Cocorullo, F. Della Corte, and I. Rendina, "Temperature dependence of the thermo-optic coefficient in crystalline silicon between room temperature and 550 K at the wavelength of 1523 nm," *Applied physics letters*, vol. 74, pp. 3338-3340, 1999.

[20] Y.-J. Rao, "Recent progress in applications of in-fibre Bragg grating sensors," *Optics and lasers in Engineering*, vol. 31, pp. 297-324, 1999.

[21] J. Goicoechea, C. Zamarreño, I. Matias, and F. Arregui, "Utilization of white light interferometry in pH sensing applications by mean of the fabrication of nanostructured cavities," *Sensors and Actuators B: Chemical*, vol. 138, pp. 613-618, 2009.

[22] X. Sang, C. Yu, T. Mayteevarunyoo, K. Wang, Q. Zhang, and P. L. Chu, "Temperature-insensitive chemical sensor based on a fiber Bragg grating," *Sensors and Actuators B: Chemical*, vol. 120, pp. 754-757, 2007.

[23] M. Jędrzejewska-Szczerska, "Response of a New Low-Coherence Fabry-Perot Sensor to Hematocrit Levels in Human Blood," *Sensors,* vol. 14, pp. 6965-6976, 2014.

[24] A. N. Chryssis, S. S. Saini, S. M. Lee, H. Yi, W. E. Bentley, and M. Dagenais, "Detecting hybridization of DNA by highly sensitive evanescent field etched core fiber Bragg grating sensors," *Selected Topics in Quantum Electronics, IEEE Journal of,* vol. 11, pp. 864-872, 2005.

[25] D. A. Jackson, "Recent progress in monomode fibre-optic sensors," *Measurement Science and Technology,* vol. 5, p. 621, 1994.

[26] C. Pang, M. Yu, X. Zhang, A. Gupta, and K. Bryden, "Multifunctional optical MEMS sensor platform with heterogeneous fiber optic Fabry–Pérot sensors for wireless sensor networks," *Sensors and Actuators A: Physical,* vol. 188, pp. 471-480, 2012.

[27] J. Yick, B. Mukherjee, and D. Ghosal, "Wireless sensor network survey," *Computer networks,* vol. 52, pp. 2292-2330, 2008.

[28] H. Shen, Y. Xu, and C. Remeikas, "Pitch Control of a Micro Air Vehicle with Micropressure Sensors," *Journal of Aircraft,* vol. 50, pp. 239-248, 2012.

[29] J. C. Kinsey, R. M. Eustice, and L. L. Whitcomb, "A survey of underwater vehicle navigation: Recent advances and new challenges," in *IFAC Conference of Manoeuvering and Control of Marine Craft*, 2006.

[30] G. W. Hunter, J. C. Xu, A. Biaggi-Labiosa, D. Laskowski, P. Dutta, S. Mondal, *et al.,* "Smart sensor systems for human health breath monitoring applications," *Journal of breath research,* vol. 5, p. 037111, 2011.

[31] R. A. Receveur, F. W. Lindemans, and N. F. de Rooij, "Microsystem technologies for implantable applications," *Journal of Micromechanics and Microengineering,* vol. 17, p. R50, 2007.

[32] J. Chou, Y. Han, and B. Jalali, "Time-wavelength spectroscopy for chemical sensing," *IEEE Photonics Technology Letters,* vol. 16, pp. 1140-1142, 2004.

[33] K. Goda and B. Jalali, "Dispersive Fourier transformation for fast continuous single-shot measurements," *Nature Photonics,* vol. 7, pp. 102-112, 2013.

[34] H. Fu, H. Liu, X. Dong, H. Tam, P. Wai, and C. Lu, "High-speed fibre Bragg grating sensor interrogation using dispersion-compensation fibre," *Electronics Letters,* vol. 44, p. 1, 2008.

[35] H. Xia, C. Wang, S. Blais, and J. Yao, "Ultrafast and precise interrogation of fiber Bragg grating sensor based on wavelength-to-time mapping

incorporating higher order dispersion," *Journal of lightwave technology,* vol. 28, pp. 254-261, 2010.

[36] C. Wang and J. Yao, "Ultrafast and ultrahigh-resolution interrogation of a fiber Bragg grating sensor based on interferometric temporal spectroscopy," *Lightwave Technology, Journal of,* vol. 29, pp. 2927-2933, 2011.

[37] Y. Wang, M. Han, and A. Wang, "High-speed fiber-optic spectrometer for signal demodulation of inteferometric fiber-optic sensors," *Optics letters,* vol. 31, pp. 2408-2410, 2006.

[38] X. Zhang, Y. Liu, H. Bae, C. Pang, and M. Yu, "Phase modulation with micromachined resonant mirrors for low-coherence fiber-tip pressure sensors," *Optics express,* vol. 17, pp. 23965-23974, 2009.

[39] H. Omran, Y. M. Sabry, M. Sadek, K. Hassan, M. Y. Shalaby, and D. Khalil, "Deeply-etched optical MEMS tunable filter for swept laser source applications," *Photonics Technology Letters, IEEE,* vol. 26, pp. 37-39, 2014.

[40] K. Isamoto, K. Totsuka, T. S. T. Sakai, A. Morosawa, C. Chong, H. Fujita, *et al.*, "A high speed MEMS scanner for 140-kHz SS-OCT," in *16th international conference on optical MEMS and nanophotonics*, 2011.

[41] F. Gan, T. Barwicz, M. Popovic, M. Dahlem, C. Holzwarth, P. Rakich, *et al.*, "Maximizing the thermo-optic tuning range of silicon photonic structures," in *Photonics in Switching*, 2007, pp. 67-68.

[42] A. H. Atabaki, A. A. Eftekhar, S. Yegnanarayanan, and A. Adibi, "Sub-100-nanosecond thermal reconfiguration of silicon photonic devices," *Optics express,* vol. 21, pp. 15706-15718, 2013.

[43] S. Pathak, P. Dumon, D. Van Thourhout, and W. Bogaerts, "Comparison of AWGs and echelle gratings for wavelength division multiplexing on silicon-on-insulator," *Photonics Journal, IEEE,* vol. 6, pp. 1-9, 2014.

[44] P. Cheben, J. Schmid, A. Delâge, A. Densmore, S. Janz, B. Lamontagne, *et al.*, "A high-resolution silicon-on-insulator arrayed waveguide grating microspectrometer with sub-micrometer aperture waveguides," *Optics express,* vol. 15, pp. 2299-2306, 2007.

[45] D. Liang, G. Roelkens, R. Baets, and J. E. Bowers, "Hybrid integrated platforms for silicon photonics," *Materials,* vol. 3, pp. 1782-1802, 2010.

[46] L. Chen, K. Preston, S. Manipatruni, and M. Lipson, "Integrated GHz silicon photonic interconnect with micrometer-scale modulators and detectors," *Optics express,* vol. 17, pp. 15248-15256, 2009.

[47] L. Chen, C. R. Doerr, L. Buhl, Y. Baeyens, and R. A. Aroca, "Monolithically integrated 40-wavelength demultiplexer and photodetector array on silicon," *Photonics Technology Letters, IEEE,* vol. 23, pp. 869-871, 2011.

[48] G.-D. Kim, H.-S. Lee, C.-H. Park, S.-S. Lee, B. T. Lim, H. K. Bae, *et al.*, "Silicon photonic temperature sensor employing a ring resonator manufactured using a standard CMOS process," *Optics express,* vol. 18, pp. 22215-22221, 2010.

[49] C.-M. Chang and O. Solgaard, "Fano resonances in integrated silicon Bragg reflectors for sensing applications," *Optics express,* vol. 21, pp. 27209-27218, 2013.

[50] J. F. Tao, H. Cai, Y. D. Gu, J. Wu, and A. Q. Liu, "Demonstration of a photonic-based linear temperature sensor," *Photonics Technology Letters, IEEE,* vol. 27, pp. 767-769, 2015.

[51] S. L. Tsao and P. C. Peng, "An SOI Michelson interferometer sensor with waveguide Bragg reflective gratings for temperature monitoring," *Microwave and Optical Technology Letters,* vol. 30, pp. 321-322, 2001.

[52] S. W. Lloyd, J. A. Newman, D. R. Wilding, R. H. Selfridge, and S. M. Schultz, "Compact optical fiber sensor smart node," *Review of scientific instruments,* vol. 78, p. 035108, 2007.

[53] J. Heebner, R. Grover, T. Ibrahim, and T. A. Ibrahim, *Optical microresonators: theory, fabrication, and applications*: Springer Science & Business Media, 2008.

[54] D. G. Rabus, *Integrated ring resonators*: Springer, 2007.

[55] Q. Xu, D. Fattal, and R. G. Beausoleil, "Silicon microring resonators with 1.5-μm radius," *Optics express,* vol. 16, pp. 4309-4315, 2008.

[56] W. Bogaerts, P. De Heyn, T. Van Vaerenbergh, K. De Vos, S. Kumar Selvaraja, T. Claes, *et al.*, "Silicon microring resonators," *Laser & Photonics Reviews,* vol. 6, pp. 47-73, 2012.

[57] M. W. Geis, S. J. Spector, R. Williamson, and T. Lyszczarz, "Submicrosecond submilliwatt silicon-on-insulator thermooptic switch," *Photonics Technology Letters, IEEE,* vol. 16, pp. 2514-2516, 2004.

[58] G. T. Reed, G. Mashanovich, F. Gardes, and D. Thomson, "Silicon optical modulators," *Nature photonics,* vol. 4, pp. 518-526, 2010.

[59] R. A. Soref and B. R. Bennett, "Electrooptical effects in silicon," *Quantum Electronics, IEEE Journal of,* vol. 23, pp. 123-129, 1987.

[60] J. Leuthold, C. Koos, W. Freude, L. Alloatti, R. Palmer, D. Korn, *et al.*, "Silicon-organic hybrid electro-optical devices," *Selected Topics in Quantum Electronics, IEEE Journal of,* vol. 19, pp. 114-126, 2013.

[61] A. Shen, C. Qiu, L. Yang, T. Dai, Y. Li, H. Yu, *et al.*, "Tunable microring based on-chip interrogator for wavelength-modulated optical sensors," *Optics Communications,* vol. 340, pp. 116-120, 2015.

[62] X. Wang, G. R. Vargas, and R. R. Panepucci, "FBG interrogation system on a silicon chip," in *Latin America Optics and Photonics Conference*, 2010, p. ThF3.

[63] G. Vargas, "Fiber Bragg grating interrogation using a micro-ring resonator tunable filter with peak wavelength detection enhancement," in *SPIE Sensing Technology+ Applications*, 2015, pp. 94800P-94800P-8.

[64] G. R. Vargas and R. R. Panepucci, "Wavelength to time interval demodulation employing a tunable micro-ring," in *Microwave & Optoelectronics Conference (IMOC), 2011 SBMO/IEEE MTT-S International*, 2011, pp. 837-841.

[65] B. B. Kyotoku, L. Chen, and M. Lipson, "Sub-nm resolution cavity enhanced micro-spectrometer," *Optics express,* vol. 18, pp. 102-107, 2010.

[66] R. März and C. Cremer, "On the theory of planar spectrographs," *Journal of lightwave technology,* vol. 10, pp. 2017-2022, 1992.

[67] J. Brouckaert, W. Bogaerts, S. Selvaraja, P. Dumon, R. Baets, and D. Van Thourhout, "Planar concave grating demultiplexer with high reflective Bragg reflector facets," *Photonics Technology Letters, IEEE,* vol. 20, pp. 309-311, 2008.

[68] Z. Shi and S. He, "A three-focal-point method for the optimal design of a flat-top planar waveguide demultiplexer," *Selected Topics in Quantum Electronics, IEEE Journal of,* vol. 8, pp. 1179-1185, 2002.

[69] Z. Xia, A. A. Eftekhar, M. Soltani, B. Momeni, Q. Li, M. Chamanzar, *et al.*, "High resolution on-chip spectroscopy based on miniaturized microdonut resonators," *Optics express,* vol. 19, pp. 12356-12364, 2011.

[70] W. N. Ye, J. Michel, and L. C. Kimerling, "Athermal high-index-contrast waveguide design," *Photonics Technology Letters, IEEE,* vol. 20, pp. 885-887, 2008.

[71] M. Uenuma and T. Motooka, "Temperature-independent silicon waveguide optical filter," *Optics letters,* vol. 34, pp. 599-601, 2009.

[72] D. Dai, "Highly sensitive digital optical sensor based on cascaded high-Q ring-resonators," *Optics Express,* vol. 17, pp. 23817-23822, 2009.

[73] T. Claes, W. Bogaerts, and P. Bienstman, "Experimental characterization of a silicon photonic biosensor consisting of two cascaded ring resonators based on the Vernier-effect and introduction of a curve fitting method for an improved detection limit," *Optics express,* vol. 18, pp. 22747-22761, 2010.

[74] L. Jin, M. Li, and J.-J. He, "Highly-sensitive silicon-on-insulator sensor based on two cascaded micro-ring resonators with vernier effect," *Optics Communications,* vol. 284, pp. 156-159, 2011.

[75] M. La Notte, B. Troia, T. Muciaccia, C. E. Campanella, F. De Leonardis, and V. Passaro, "Recent advances in gas and chemical detection by Vernier effect-based photonic sensors," *Sensors,* vol. 14, pp. 4831-4855, 2014.

[76] J. Hu and D. Dai, "Cascaded-ring optical sensor with enhanced sensitivity by using suspended Si-nanowires," *Photonics Technology Letters, IEEE,* vol. 23, pp. 842-844, 2011.

[77] C. Ciminelli, F. Dell'Olio, C. Campanella, V. Passaro, and M. Armenise, "Integrated optical ring resonators: modelling and technologies," *NOVA Science Publishers, New York,* 2009.

[78] W. Bogaerts, R. Baets, P. Dumon, V. Wiaux, S. Beckx, D. Taillaert, *et al.*, "Nanophotonic waveguides in silicon-on-insulator fabricated with CMOS technology," *Lightwave Technology, Journal of,* vol. 23, pp. 401-412, 2005.

[79] A. Kersey and T. Berkoff, "Fiber-optic Bragg-grating differential-temperature sensor," *Photonics Technology Letters, IEEE,* vol. 4, pp. 1183-1185, 1992.

[80] Y.-J. Rao, D. J. Webb, D. A. Jackson, L. Zhang, and I. Bennion, "In-fiber Bragg-grating temperature sensor system for medical applications," *Lightwave Technology, Journal of,* vol. 15, pp. 779-785, 1997.

[81] Z. Zhang, Y. Chen, H. Liu, H. Bae, D. A. Olson, A. K. Gupta, *et al.*, "On-fiber plasmonic interferometer for multi-parameter sensing," *Optics express,* vol. 23, pp. 10732-10740, 2015.

[82] Y. Vlasov and S. McNab, "Losses in single-mode silicon-on-insulator strip waveguides and bends," *Optics express,* vol. 12, pp. 1622-1631, 2004.

[83] X. Wang, X. Guan, Q. Huang, J. Zheng, Y. Shi, and D. Dai, "Suspended ultra-small disk resonator on silicon for optical sensing," *Optics letters,* vol. 38, pp. 5405-5408, 2013.

[84] M. Soltani, Q. Li, S. Yegnanarayanan, and A. Adibi, "Toward ultimate miniaturization of high Q silicon traveling-wave microresonators," *Optics express,* vol. 18, pp. 19541-19557, 2010.

[85] M.-S. Kwon and W. H. Steier, "Microring-resonator-based sensor measuring both the concentration and temperature of a solution," *Optics express,* vol. 16, pp. 9372-9377, 2008.

[86] V. Zamora, P. Lützow, M. Weiland, and D. Pergande, "Investigation of cascaded SiN microring resonators at 1.3 µm and 1.5 µm," *Optics express,* vol. 21, pp. 27550-27557, 2013.

[87] E. S. Ferry, *A Handbook of Physics Measurements: By Ervin S. Ferry. In Collaboration with OW Silvey, GW Sherman, Jr., and DC Duncan*: John Wiley & Sons, 1926.

[88] C. Campanella, C. Campanella, F. De Leonardis, and V. Passaro, "A high efficiency label-free photonic biosensor based on vertically stacked ring resonators," *The European Physical Journal Special Topics,* vol. 223, pp. 2009-2021, 2014.

[89] F. De Leonardis, C. E. Campanella, B. Troia, A. G. Perri, and V. Passaro, "Performance of SOI Bragg grating ring resonator for nonlinear sensing applications," *Sensors,* vol. 14, pp. 16017-16034, 2014.

[90] P. Urquhart, "Compound optical-fiber-based resonators," *JOSA A,* vol. 5, pp. 803-812, 1988.

[91] K. Oda, N. Takato, and H. Toba, "A wide-FSR waveguide double-ring resonator for optical FDM transmission systems," *Lightwave Technology, Journal Of,* vol. 9, pp. 728-736, 1991.

[92] L. Y. Tobing, D. C. Lim, P. Dumon, R. Baets, and M.-K. Chin, "Finesse enhancement in silicon-on-insulator two-ring resonator system," *Applied Physics Letters,* vol. 92, p. 101122, 2008.

[93] L. Jin, M. Li, and J.-J. He, "Optical waveguide double-ring sensor using intensity interrogation with a low-cost broadband source," *Optics letters,* vol. 36, pp. 1128-1130, 2011.

[94] B. Guha, J. Cardenas, and M. Lipson, "Athermal silicon microring resonators with titanium oxide cladding," *Optics express,* vol. 21, pp. 26557-26563, 2013.

[95] E. Dulkeith, F. Xia, L. Schares, W. M. Green, and Y. A. Vlasov, "Group index and group velocity dispersion in silicon-on-insulator photonic wires," *Optics express,* vol. 14, pp. 3853-3863, 2006.

[96] Z. Zhang, H. Bae, T. Nagaya, Y. Nakamura, P. Choyke, H. Kobayashi, *et al.*, "In Vivo Pressure and Temperature Monitoring during Near Infrared Photo-Immunotherapy Using a Fiber Optic Sensor," in *Frontiers in Optics*, 2015, p. FTh2E. 2.

[97] J. Song, X. Luo, X. Tu, M. K. Park, J. S. Kee, H. Zhang, *et al.*, "Electrical tracing-assisted dual-microring label‐free optical bio/chemical sensors," *Optics express*, vol. 20, pp. 4189-4197, 2012.

[98] C. Qiu, J. Shu, Z. Li, X. Zhang, and Q. Xu, "Wavelength tracking with thermally controlled silicon resonators," *Optics Express*, vol. 19, pp. 5143-5148, 2011.

[99] B. Yang, A. Shen, C. Qiu, T. Hu, L. Yang, H. Yu, *et al.*, "Microring-based ratio-metric wavelength monitor on silicon," *Optics letters*, vol. 39, pp. 3298-3300, 2014.

[100] N. Li, E. Timurdogan, C. V. Poulton, M. Byrd, E. S. Magden, Z. Su, *et al.*, "C-band swept wavelength erbium-doped fiber laser with a high-Q tunable interior-ridge silicon microring cavity," *Optics express*, vol. 24, pp. 22741-22748, 2016.

[101] W. M. Rohsenow, J. P. Hartnett, and Y. I. Cho, *Handbook of heat transfer* vol. 3: McGraw-Hill New York, 1998.

[102] A. Arbabi and L. L. Goddard, "Dynamics of self-heating in microring resonators," *IEEE Photonics Journal*, vol. 4, pp. 1702-1711, 2012.

[103] V. R. Almeida, R. R. Panepucci, and M. Lipson, "Nanotaper for compact mode conversion," *Optics letters*, vol. 28, pp. 1302-1304, 2003.

[104] J. Spannhake, O. Schulz, A. Helwig, A. Krenkow, G. Müller, and T. Doll, "High-temperature MEMS heater platforms: long-term performance of metal and semiconductor heater materials," *Sensors*, vol. 6, pp. 405-419, 2006.

[105] A. Atabaki, E. S. Hosseini, A. Eftekhar, S. Yegnanarayanan, and A. Adibi, "Optimization of metallic microheaters for high-speed reconfigurable silicon photonics," *Optics express*, vol. 18, pp. 18312-18323, 2010.

[106] Y. Wang, M. Han, and A. Wang, "Analysis of a high-speed fiber-optic spectrometer for fiber-optic sensor signal processing," *Applied optics*, vol. 46, pp. 8149-8158, 2007.

[107] L. Yu, Y. Yin, Y. Shi, D. Dai, and S. He, "Thermally tunable silicon photonic microdisk resonator with transparent graphene nanoheaters," *Optica*, vol. 3, pp. 159-166, 2016.

[108] L. Zhou, X. Zhang, L. Lu, and J. Chen, "Tunable Vernier Microring Optical Filters With p-i-p-Type Microheaters," *IEEE Photonics Journal*, vol. 5, pp. 6601211-6601211, 2013.

[109] X. Li, H. Xu, X. Xiao, Z. Li, Y. Yu, and J. Yu, "Fast and efficient silicon thermo-optic switching based on reverse breakdown of pn junction," *Optics letters*, vol. 39, pp. 751-753, 2014.

[110] X. Wang, A. Lentine, C. DeRose, A. L. Starbuck, D. Trotter, A. Pomerene, *et al.*, "Wide-range and fast thermally-tunable silicon photonic microring resonators using the junction field effect," *Optics express*, vol. 24, pp. 23081-23093, 2016.